Exploring *N*-Heterocyclic Carbene Effects on Hyperpolarisation with *para*-Hydrogen

Rhianna Nelson-Forde

MSc by Research

University of York

Chemistry

June 2017

Abstract

This research focuses on the Nuclear Magnetic Resonance (NMR) applications of Signal Amplification by Reversible Exchange (SABRE); a hyperpolarisation technique discovered within the Duckett Group. The hyperpolarisation technique, SABRE, is used to enhance the magnetic resonance signals produced in NMR and improve the resolution seen in an NMR spectrum. *Para*hydrogen is used as the source of hyperpolarisation. This research aims to focus on developing SABRE techniques by determining the most efficient SABRE-active catalyst which can be further applied to biomedical applications.

SABRE catalysts are made up of an N-heterocyclic carbene ligand and a substrate in a solvent of choice. In 2009, A SABRE-active catalyst with the general formula $[Ir(H)_2(NHC)(sub)_3]Cl$, where NHC = N-heterocyclic carbenes, and substrates, were synthesised and used to enhance NMR signals through the hyperpolarisation technique, SABRE. This research aims to investigate different N-heterocyclic ligands and determine the efficiencies of their corresponding SABRE catalysts by determining the largest total signal enhancements produced by these catalysts. The catalysts were characterised by Nuclear Magnetic Resonance (NMR) spectroscopy and Mass Spectrometry (MS). These catalysts were further examined to determine their optimum environment as signal enhancement is dependent on various properties such as; substrate concentration, temperature and solvent. The rates of substrate exchange at the catalyst were also determined to establish the optimum conditions.

As SABRE can be applied to biomedical applications, two biological molecules were used as the substrates throughout this research and these were pyridine and a pyridine derivative, 3-5-Lutidine. The ^{1}H NMR signals of pyridine and 3,5-lutidine were shown to be enhanced using SABRE, a non-hydrogenative *para*hydrogen induced polarisation (PHIP) application.

Work has previously looked at different NHC and substrate combinations that produce the largest total signal enhancements and by optimisation of the conditions and NHC, a 5500-fold total pyridine signal enhancements was discovered when the NHC was IMes, 1,3-bis(2,4,6-trimethylphenyl)-imidazol-2-ylidene.[1]

Table of Contents

Table of Figures

Table of Tables

Table of Equations

Acknowledgements

I would like to take the opportunity to firstly thank my supervisor, Professor Simon Duckett for his support and guidance throughout my Masters. He has been incredibly helpful and encouraged me to attend many symposiums that have been very beneficial to my research.

I would secondly like to take the opportunity to thank everyone in the Duckett research group for their support and invaluable helpfulness throughout this project. I would like to give a special thanks to Pete Rayner for all his synthesis of the various complexes he kindly made for me, Marianna Fekete for all her help and guidance throughout with synthesis as well and to Wissam Iali to all his amazing knowledge and guidance through my synthesis. I also thank my office mates, Chris, Will, Phil and Robin. With a special thanks to Kate, Amy, Emma, Pete Rich, Olga, Liz, Jenny and Barby for keeping me thoroughly entertained and for all their help and advice.

I would also like to thank all the technical and academic staff in the department for providing mass spectra and replacing all the broken NMR tubes.

Lastly, this would not be possible without the support and encouragement from my Mum and Dad; they kept me sane and helped me persevere throughout this project. I would also like to thank all my family and friends, especially my best friends Mario, Norhan and Yeni, who have been my rocks and kept me focused throughout my Masters.

Lastly and most importantly I would like to thank God who without him, this would all not be possible.

Declaration

I hereby declare, to the best of my knowledge, that the work presented within this thesis is original, except where stated otherwise and referenced appropriately, and has not been submitted or published previously in other's work for this or any other university. All sources are acknowledged as References.

1   Introduction

In medical and chemical applications, it is very important to be able to analyse and characterise the multitude of compounds that are associated with a new drug. A spectroscopic technique called Nuclear Magnetic Resonance (NMR) is used for the elucidation of structures of newly synthesized compounds, natural products and semi-synthesized compounds.[2] Additionally, by using NMR active species, Magnetic Resonance Imaging (MRI) is able to map the distribution of these species by gaining images from within the human body.[3] The particular strength in NMR lies in its ability to distinguish between different chemical species and provide us with simultaneous information on the structures, concentration distribution and flow processes occurring in a particular process unit.[4] However, the field of magnetic resonance is currently limited by a sensitivity issue, which will be explained later on in this thesis. To overcome this we use a hyperpolarisation technique called Signal Amplification By Reversible Exchange (SABRE).[5]

1.1   Nuclear Magnetic Resonance

Nuclear Magnetic Resonance (NMR) is a widespread analytical tool, which was first observed by Rabi *et al*[6] in the late 1930s, when a beam of hydrogen molecules were sent through a homogenous magnetic field.[7] It is now used to identify and analyse compounds by distinguishing the chemical environment of the different nuclei present in them. The quality of an NMR spectra is determined firstly by its sensitivity and secondly, by its resolution.

The most commonly used spin $\frac{1}{2}$ nuclei used in NMR is the proton, which is nearly 100% abundant and has the most sensitivity out of all commonly studied NMR nuclei. This means that it produces the largest NMR signal and hence rapid probing is possible. By changing key acquisition parameters, such as the delay between measurements, you can improve the accuracy of the measurement. Other common spin $\frac{1}{2}$ nuclei used to characterise materials are ^{13}C, ^{15}N, ^{19}F and ^{31}P which have a lower sensitivity than that of ^{1}H NMR. For example in ^{13}C NMR, the abundance is a lot lower at 1.1%.

The main limitation of NMR is its low sensitivity, meaning that it is extremely hard to identify and characterise materials in low concentrations. In recent years, significant advances in the field of sensitivity enhancement have been achieved through different avenues such as increasing the magnetic field.[8] The minimum sample amount that can be detected for analysis by traditional NMR is within the range of 10^{-9} and 10^{-11} mol of

sample[9] but hyperpolarisation techniques have been developed and this project seeks to address how we overcome this sensitivity issue.

1.2 NMR Sensitivity Issue

NMR probes the energy levels that correspond to the nuclear spin states when they are exposed to a magnetic field. Some atomic nuclei possess spin, where I, is conventionally given to nuclear spin quantum number. Depending on the spin quantum number (I), there are different numbers of orientations that can be taken by a nucleus with respect to the applied field.[10] A nuclear spin state with spin $2I + 1$ gives rise to an equal number of nuclear energy levels (I being the spin quantum number).[11] As ^{1}H has a spin quantum number of $\frac{1}{2}$, as seen in Figure 1, 2 possible spin alignments result with the nuclear spin being either parallel, α, or anti parallel to the field, β. This also applies to both ^{13}C and ^{15}N which also have a nuclear spin quantum number of $\frac{1}{2}$.
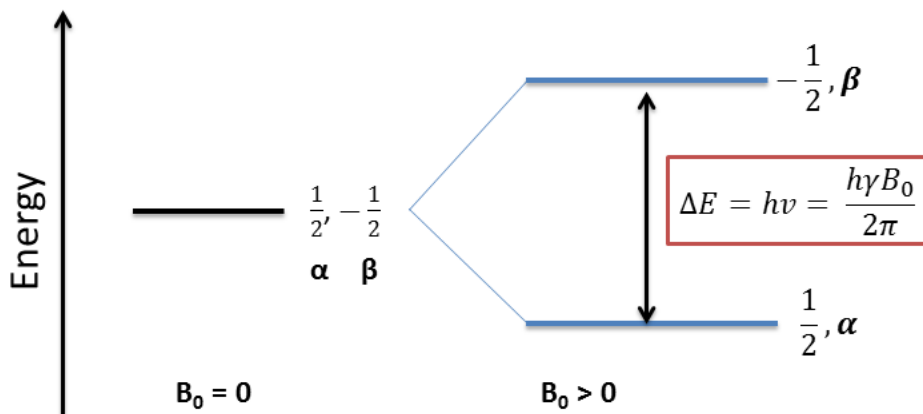
Figure 1: The splitting between two nuclear spin levels (nuclear Zeeman splitting) of a ^{1}H nucleus as a function of the applied magnetic field. ^{1}H nuclei are spin $-\frac{1}{2}$ so the nuclear ground states split into spin states α and β in an applied magnetic field. h is Planck's constant (6.626×10^{-34} m^{2}Kgs^{-1}), γ is the gyromagnetic ratio, B_0 is the applied magnetic field, v is the radio wave frequency and ΔE is the population energy difference.

The sensitivity problems arise due to the small energy difference between the two nuclear spin states of a hydrogen nucleus which is shown in Figure 1. The difference between the two energy levels is related to the energy difference by the Boltzmann distribution:

$$\frac{N_\alpha}{N_\beta} = e^{\frac{-\Delta E}{kT}}$$

Equation 1: Boltzmann distribution where n is the population of an energy level, ΔE is the difference between the energy levels, k is the Boltzmann constant (1.381×10^{-23} m^2 kg s^{-2} K^{-1}) and T is the temperature in Kelvin.[12]

Boltzmann Distribution
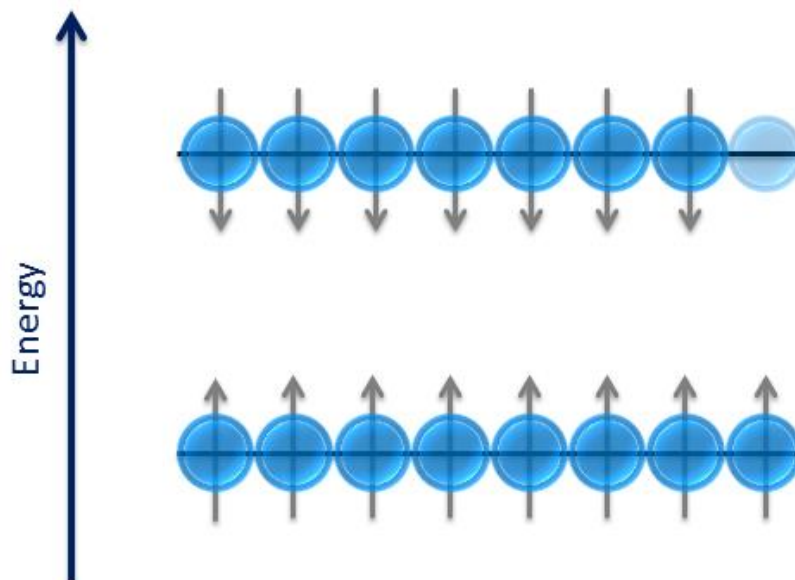
Figure 2: Schematic diagram of Boltzmann distribution of spins in a magnetic field. The energy difference between α (aligned with the magnetic field) and β (aligned against the field) is very small in the Boltzmann distribution, adapted by Frydman *et al.*[13]

NMR spectroscopy probes the population difference between these energy levels and by using the Boltzmann equation, for a magnetic field of 9.4 T in a 400 MHz spectrometer with T equal to 298 K we see:

$$\frac{N_\alpha}{N_\beta} = 0.99993$$

This means that the population difference is just 1 in 32,000[14]. Also as mentioned previously, the abundance of magnetic nuclei in ^{1}H is less than 100% (99.7%) whereas in ^{13}C it is 1.1%. This small population difference leads to longer scan times.

There are a number of ways to improve the inherent insensitivity of NMR:

o   Using stronger magnets to increase the energy difference between the states, however this is extremely expensive. The world's largest magnet has a proton frequency of 1.2 GHz. This means that, for example, ^{1}H nuclei at 298 K, would give a population difference of 1 in 15,000. This magnet is currently in operation in Japan.[15]

o   Run more scans and average the signal.

- o You could also decrease the temperature, which in turn increases the population difference; however this is limited by the solvents available.
- o Use a high concentration which can be more costly as more sample is required.

Alternatively, hyperpolarisation techniques can be used to increase the sensitivity of NMR. Such approaches increase the population difference, by polarisation, of the spin states.

1.3 Hyperpolarisation

An increasingly popular method of addressing sensitivity is through hyperpolarisation. Hyperpolarisation is a technique that allows NMR signals to be enhanced by generating non-Boltzmann spin state populations between the energy levels.[16]

Non- Boltzmann Distribution
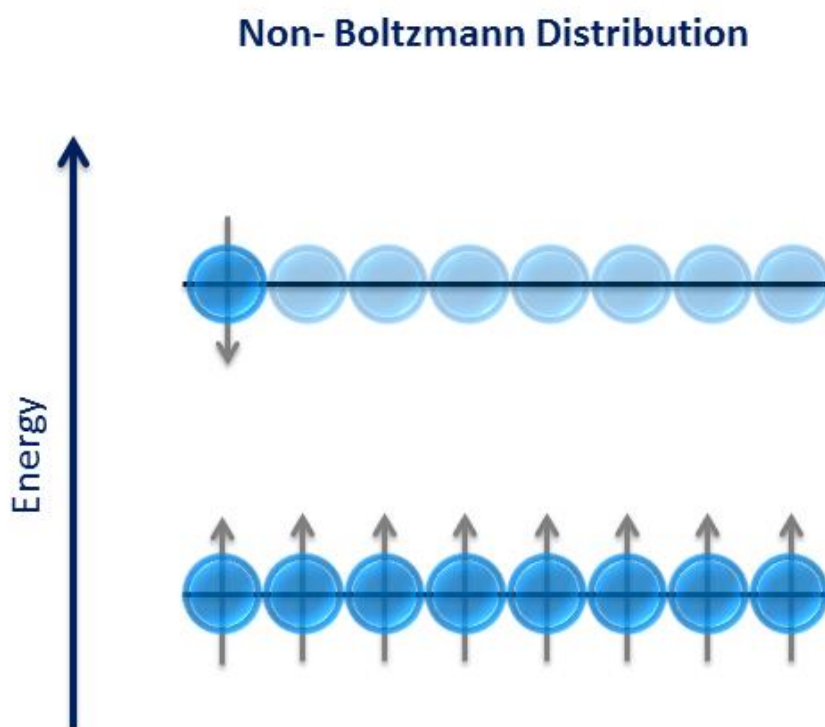
Figure 3: Schematic diagram of the spins in a magnetic field for a non-Boltzmann distribution where fewer spins align against the field, increasing the signal intensity for the observable transitions. As seen previously in Figure 2, the Boltzmann distribution diagram shows what is achieved on a thermal NMR spectrum without hyperpolarisation so the population difference between the energy levels is very small, whereas hyperpolarisation increases this difference, adapted by Frydman et al.[13]

This effect was first demonstrated by Carver and Slichter in 1953, when the nuclear spin polarisation was increased for ^{7}Li nuclei through polarisation transfer from free electrons. This meant that the nuclear spin polarisation, that is relatively low, can be increased well above the thermal equilibrium level.[17] The significant increase in nuclear spin polarisation was later called hyperpolarisation. Hyperpolarisation techniques such as optical pumping

and dynamic nuclear polarisation (DNP) have been developed over the last 60 years and applied to chemical compounds with potential biomedical relevance.[18] A relatively new *Para*hydrogen induced polarisation (PHIP)-based hyperpolarisation technique discovered by Duckett *et al*[5, 16] called SABRE (explained further in section 1.5) is the technique used in conjunction with NMR throughout this thesis.

1.4 *Para*Hydrogen Induced Polarisation (PHIP)

*Para*hydrogen induced polarisation, known as PHIP, is a hyperpolarisation technique based on a hydrogenation reaction that uses the nuclear singlet state of *para*hydrogen as a source of hyperpolarisation.[19]

This effect has been known since 1987 when Weitekamp predicted that the *para*hydrogen state can be converted, by a chemical reaction, into the polarised nuclear spins of the products of molecular hydrogen additions.[20, 21] This was then successfully proven experimentally a year later by Weitekamp and Bowers when they characterised antiphase signal enhancements by hydrogenating acrylonitrile with *para*hydrogen.[21]
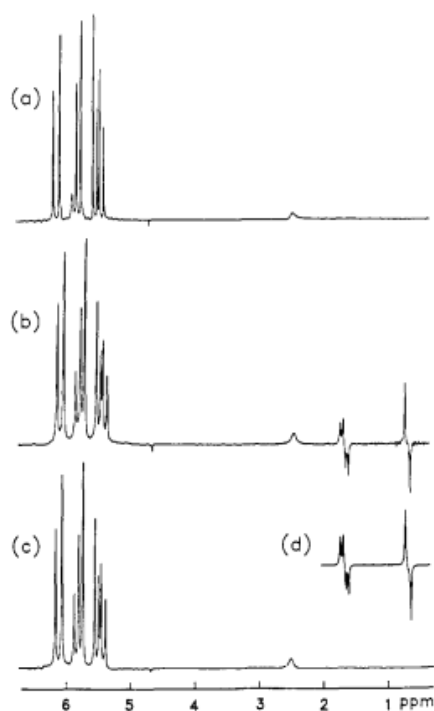
Figure 4: NMR spectrum, taken from Weitekamp *et al*[21], where the hydrogenation of acrylonitrile, to propionitrile, catalysed by tris(phenylphospine)rhodium(I) chloride was observed. Part (a) shows the ^{1}H NMR spectrum before the reaction took place. Part (b) shows the hydrogenation to propionitrile with enhanced signals transitioning between the δ 3-1. Part (c) is the spectrum of the sample at equilibrium and part (d) demonstrates the traditional PHIP-type signals observed from hydrogenation reactions.

PHIP allows for both non-hydrogenative PHIP (where the hyperpolarized substrate and *para*hydrogen exchange on the metal centre via SABRE) and hydrogenative PHIP (which

occurs via *Para*hydrogen and Synthesis Allow Dramatically Enhanced Nuclear Alignment - PASADENA and Adiabatic Longitudinal Transport After Dissociation Engenders Net Alignment - ALTADENA). This concept is explained further in 1.4.3.

1.4.1 *Para*hydrogen (*p*-H$_2$) and hydrogen spin isomers

When metal complexes react with molecular hydrogen, they form metal-hydride ligands which can be monitored and characterised via NMR. Due to the inherently insensitive nature of the NMR technique, if the concentration of the metal-hydride species is low then using NMR would be less efficient and effective for characterisation, so to be able to detect these species a method which requires the use of *para*hydrogen is used.[22] Figure 5 demonstrates the use of *para*hydrogen in NMR experiments compared to the NMR experiments without the use of *para*hydrogen. The antiphase signals seen in Figure 5 in the red box are characteristic of PASADENA (*Para*hydrogen And Synthesis Allow Dramatically Enhanced Nuclear Alignment) where both the αβ and βα spin states are populated and due to population difference being much greater than the Boltzmann distribution, as seen in Figure 5, the NMR produces larger enhancements. This will be explained in more detail later on.
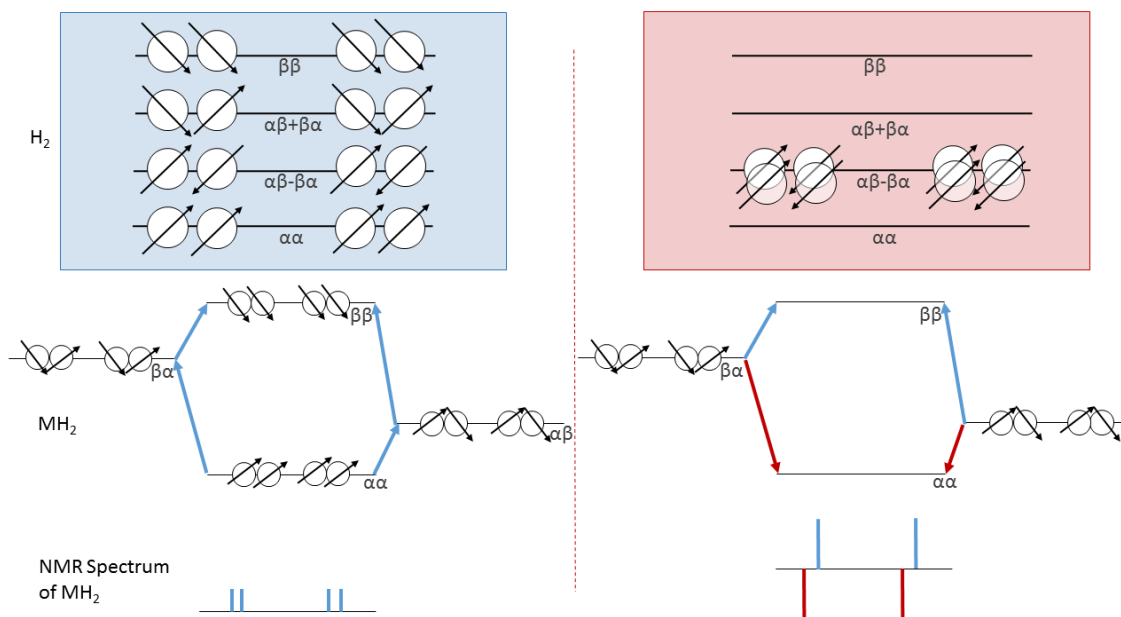
Figure 5: The section coloured in blue is an NMR experiment without *para*hydrogen addition and the section coloured red shows the NMR experiment with *para*hydrogen addition. The NMR signal seen without hyperpolarisation shows two doublets. The lowest energy state, αβ-βα, which is the only *para*hydrogen spin state transition, is populated in the H$_2$ selectively. Hyperpolarisation is seen on the NMR spectrum with resulting antiphase signals adapted by Duckett et al.[23]

Molecular hydrogen (H$_2$) comes in two isomeric forms, one where the two protons align parallel to each other (*ortho*hydrogen) or where they lie next to each other but anti-

parallel, termed *para*hydrogen.[24] As stated previously, a single hydrogen nucleus is either quantified as +½ and -½ nuclear spin with the spin aligning with or against the magnetic field. Henceforth, the spins of dihydrogen may be classified as either; α which aligns parallel to the field or β which aligns anti-parallel to the field[25]. It is the different interaction of these spins that gives four different energy transitions: αα, ββ, αβ+βα and αβ-βα for the dihydrogen molecule. The first three possible forms (seen in Figure 6) are symmetric and reflect a triplet state which refers to *ortho*-H_2. The other form (also seen in Figure 6) is antisymmetric , a singlet, and is referred to as *para*-H_2.[22]
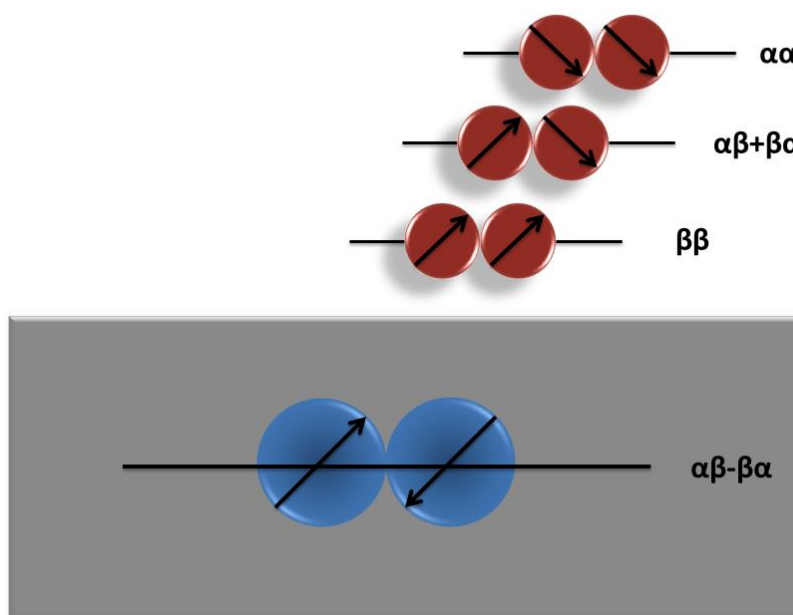
Figure 6: A diagram to show the four different dihydrogen spin transitions, with three transitions being *ortho*hydrogen and the singlet transition being *para*hydrogen.

The triplet states of *ortho*hydrogen (also known as T_{+1}, T_{-1} and T_0) can be affected by the application of a magnetic field due to the Zeeman splitting. However, *para*hydrogen is unaffected as the two opposing spins mean that it is NMR silent[26]. The energy difference of the two spin isomers is based on the total wavefunction of the molecule which constitutes of translation, vibration, electronic, rotation and the nuclear spin components.[27]

$$\varphi_{overall} = \varphi_{trans} \times \varphi_{vib} \times \varphi_{elect} \times \varphi_{rot} \times \varphi_{spin}$$

Equation 2: The total wavefunction (ψ) of a fermion that consists of five components.

The overall molecular wavefunction of H_2 must be anti-symmetric.[28] However, the vibration, electronic and translation are all symmetric. The symmetric *ortho* spin isomers are therefore restricted to antisymmetric rotational states (J= 1, 3, 5 etc.) and the anti-symmetric *para* state is restricted to symmetric rotational states (J= 0, 2, 4 etc.). This results in *para*-H_2 being at a lower energy than *ortho*-H_2.[29] This energy difference can be harnessed through the Boltzmann distribution hence *para*hydrogen is favoured at a low temperature.[22] The interconversion of *para*hydrogen and *ortho*hydrogen isomers is spin forbidden but is possible in the presence of a paramagnetic species.[22] By using a paramagnetic species as a catalyst, the symmetry is broken and the conversion between both species takes place due to the increase in this process and driving the equilibration to change the isomers.[30]

1.4.2 *Para*hydrogen generation

Normally, hydrogen consists of an equilibrium mixture of *ortho* and *para*hydrogen and because of this *para*hydrogen enhancements cannot be achieved using hydrogen from a cylinder because of the low percentage of *para*hydrogen at room temperature and the Boltzmann distribution where there is barely any population different between *ortho* and *para* states.[25] Hydrogen must be cooled to acquire *para*hydrogen and the temperature can cause the equilibrium in hydrogen to shift varying the proportion of *ortho* and *para*hydrogen present (this is seen in Figure 7).

	0 K	20 K	75 K	150 K	273 K	>273 K
parahydrogen	100	99.82	51.86	28.54	25.13	25
orthohydrogen	0	0.18	48.14	71.46	74.87	75
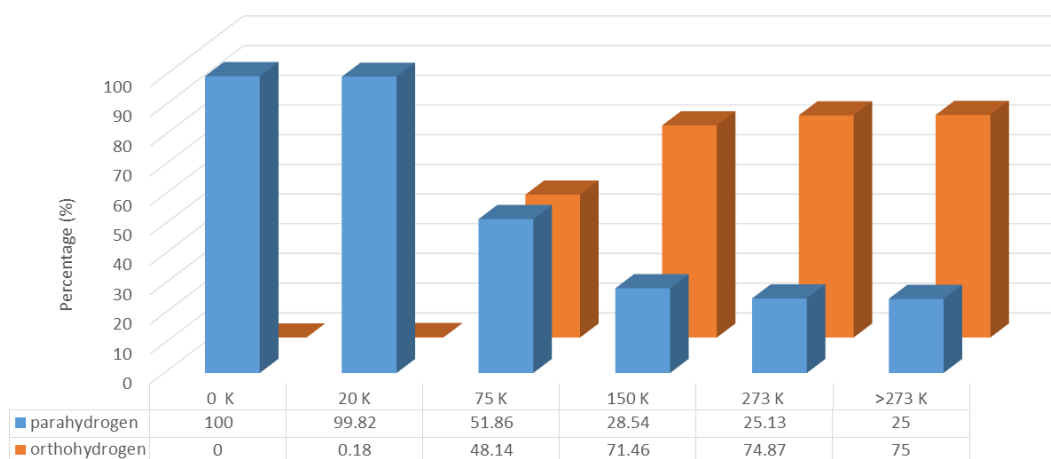
Figure 7: Graph to show the effect temperature has on the percentage abundance of *para*hydrogen and *ortho*hydrogen. The percentage of *para*hydrogen decreases when the temperature increases, this then causes the percentage of orthohydrogen to increase with the rising temperature. Adapted by Duckett et al[29].

Molecular hydrogen contains ¾ *ortho*hydrogen and ¼ *para*hydrogen at room temperature. When the temperature is at absolute zero, the more stable state of hydrogen, *para*hydrogen, is favoured therefore *para*hydrogen is at approximately 100% abundance. At easily reached temperatures of about 30 K, *ortho*hydrogen is able to convert to *para*hydrogen at a ratio of 96.9: 3.1 and it is stable in this form.[31]

Once the hydrogen gas is removed from the catalyst, interconversion can no longer take place meaning that *para*hydrogen can be made and stored.[32]

The spin functions of α and β, the nuclear wavefunction of parahydrogen, can be described as:

$$\Psi = \frac{1}{\sqrt{2}}(\alpha\beta - \beta\alpha)$$

As this wavefunction has a total nuclear spin of 0, parahydrogen has a total nuclear spin of 0. This means it is NMR silent, showing no signal.[33] Hydrogen; however shows a proton signal at δ 4.5 which arises from *ortho*hydrogen.

For hydrogenative PHIP (PASADENA or ALTADENA), the magnetic symmetry must be broken and the *para*hydrogen is transported into a new environment. SABRE requires a catalyst to transfer polarisation to the substrate after binding the hydrogen without hydrogen actually altering the substrate's structure. This hyperpolarisation process is non-hydrogenative and the substrate dissociates.

1.4.3 PASADENA and ALTADENA

As *p*arahydrogen (*p*-H_2) cannot be detected, a reaction needs to occur to break its symmetry. These reactions can take place at a high or low magnetic field and two different effects are observed. These are PASADENA (*Para*hydrogen And Synthesis Allow Dramatically Enhanced Nuclear Alignment) which occurs when a reaction takes place in a high magnetic field or ALTADENA (Adiabatic Longitudinal Transport After Dissociation Engenders Net Alignment) for reactions occurring at low magnetic field.[34]

For an NMR signal with PASADENA, two pairs of antiphase doublets occur, where one absorption line points in a positive direction and one emission line points in a negative direction. This is because the αβ and βα states become overpopulated (as seen in Figure

8). In ALTADENA, there are only two spectral lines (one absorptive and one emissive) as only one αβ or βα state is populated[33].
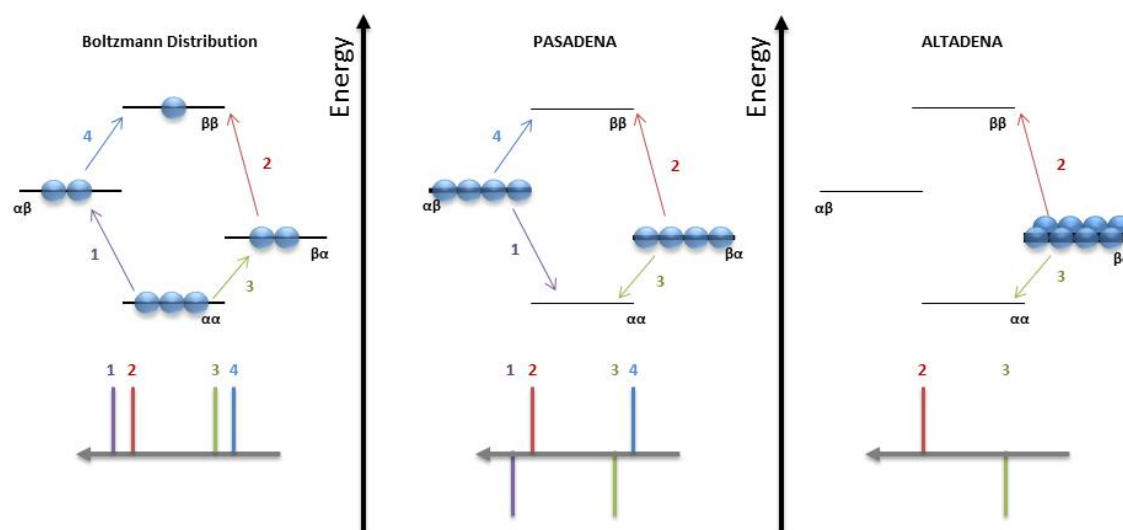
Figure 8: Population model based on an AX type of spin system with the four levels αα, αβ, βα and ββ. In the Boltzmann distribution, the four possible spin alignment transitions of hydrogen spin isomers (far left) are seen to give two doublets within a high magnetic field. The four spin NMR transitions that are allowed yields the ¹H NMR spectra (seen above far left). As PASADENA and ALTADENA are under parahydrogen conditions, they assume non-Boltzmann distribution type conditions. For PASADENA (middle) the population difference in the AX spin system align on the order of unity. However, the selective population of the energy states leads to two antiphase doublets seen in the ¹H NMR spectra (above middle). The ALTADENA ¹H NMR spectra (below far right) shows that only one of two levels, αβ or βα, are populated so only two transitions are possible. Adapted by Natterer et al[33].

In 1988, Pravica *et al* reported experiments where *para*hydrogen is added to a solution outside of the NMR spectrometer producing magnetic states at a low field called ALTADENA.[35] With ALTADENA which uses pH_2 (*para*hydrogen) at low magnetic fields and populates singlet character spin state products, the adiabatic increase of the magnetic field transports this population to the preferred energy level, βα; this allows one spin (positive signal) to emit and the negative signal to absorb.[9]

When a PASADENA experiment is taking place, a hydrogenation with *para*hydrogen occurs inside the magnet of the NMR spectrometer.[33] When the parahydrogen nuclei are placed into an AX type of spin system, then both αβ and βα become populated and four transitions are possible. Due to the population difference and the selective population of the energy levels, all four possible transitions produce enhanced NMR signals compared to standard NMR signals with two antiphase doublets also produced.[33, 36] In practice, PASADENA has proven more popular due to the quicker hyperpolarisation to scan time.

PHIP has also been shown to enhance a number of other nuclei, including ^{13}C nuclei[37]. This shows that PHIP is a powerful tool for understanding reactions and characterising many different molecules especially in biological applications.[38, 39] However, a problem with normal PHIP is that a precursor needs to exist which can be hydrogenated, such as 1,5 –cyclooctadiene (COD).This problem is overcome when a technique known as Signal Amplification by Reversible Exchange (SABRE) is used.

1.5   SABRE

As mentioned previously in section 1.3, a new approach to the generation of PHIP was discovered in 2009 by Duckett *et al* that is non-hydrogenative. This relies on *para*hydrogen and a substrate capable of reversibly binding to a suitable metal host.[16] There are therefore, three key components to SABRE; the metal complex, the substrate and *para*hydrogen.

1.5.1 Introduction to SABRE

In the SABRE process, *Para*hydrogen undergoes an oxidative addition reaction with the metal centre, seen in Figure 9. The metal catalyst operates by facilitating the transfer of spin magnetisation without any chemical change, creating a template where *para*hydrogen and the substrate temporarily bind.[40] The non-equilibrium spin order of the former *para*hydrogen molecule is initially located only in the complex's hydride ligands, therefore when the metal complex forms in a weak magnetic field, the magnetisation is transferred from the *para*hydrogen derived hydride ligands to the nuclei of the substrate molecule through the scalar coupling network.[25]
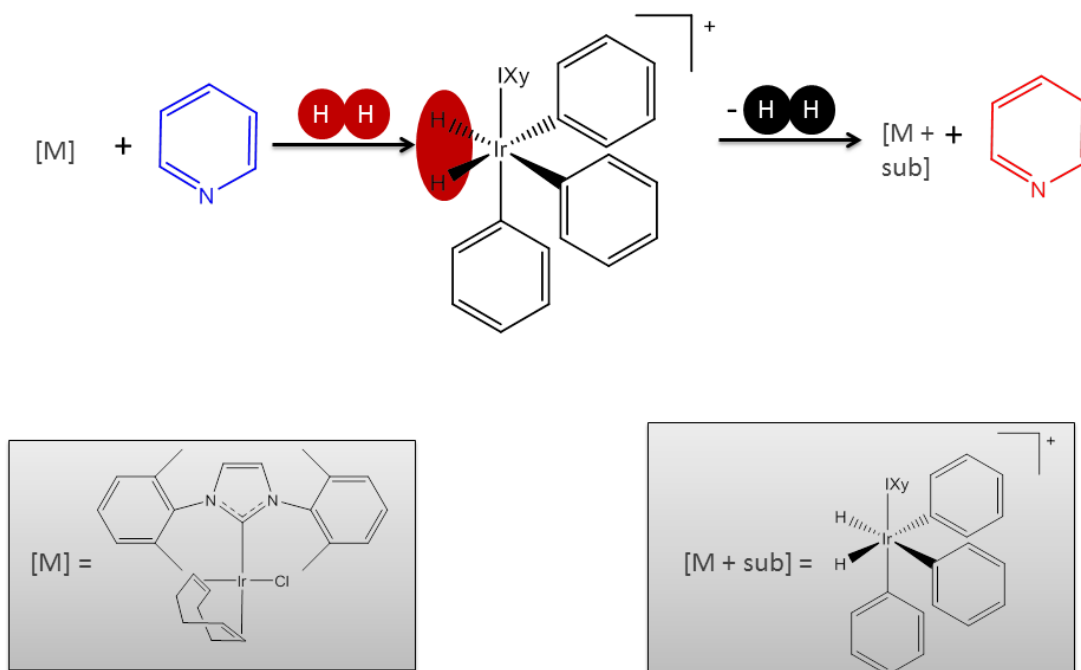
Figure 9: A schematic representation of SABRE, where the polarisation is transferred from the *para*hydrogen derived hydrides to the substrate molecules, which in this example is pyridine. The red colour is used to identify the difference between the polarised parahydrogen derived hydrides and the non-polarised hydrogens. The iridium metal catalyst used in this schematic diagram is the 1,3 -bis(2,6-dimethylbenzene)imidazol-2-ylidene (IXy) complex which will be examined later on. Adapted from Adams et al[5].

In 2009, Adams et al discussed a simplified theory behind polarisation transfer where in the first SABRE experiments, polarisation was transferred from *para*hydrogen to the nuclei species of substrates such as pyridine, where in this model these substrates contained a single pair of protons. However, pyridine is known to contain five hydrogen nuclei, which respectively make up a large scalar coupling network.[41] This would have been too consuming for the model. As seen in Figure 9, the metal complexes that form the NHC, substrate and *para*hydrogen derived hydrides contain two substrate molecules in the equatorial planes, both of which are polarised from the scalar coupling network from the *para*hydrogen. This real life situation is different to the theory model, which Adams et al modelled on only one equatorial site.[41] The scalar coupling is also referred to as *J*-coupling or spin-spin couplings within the model Adams et al theorised. As seen in figure 8, where the population model was based on an AX spin system with four levels, this model complex, is therefore a four-spin system, where two spins originate from the *para*hydrogen and two spins originate from the substrate bound to the complex.

This model and theory resulted in the conclusion that the polarisation transfer is dependent on the magnetic field, the balance between the scalar coupling and the chemical shift being often optimal at around 65 G.[5, 41] One can view this process as

following a periodic function, in which polarisation flows in a cyclic fashion between the hydrides and ligand. When the lifetime of the complex matches the time period which places maximum polarisation on the ligand, dissociation leads to the creation of optimal free substrate hyperpolarisation, as described by Adams. Interestingly, the destruction of the singlet character of the dihydride through SABRE results in a visibly hyperpolarised hydride signal which is of opposite phase to those of the ligands. The relative phases of these signals are actually controlled by the sign of J_{HH} which is negative and hydride hyperpolarisation is not always visible because these signals relax rapidly. Furthermore, while typical hydride ligand couplings lie in the region of 1 Hz, they lie within the linewidth of the hydride resonance and lead to no visible effect, although their presence can be confirmed by COSY methods. Hence SABRE reflects a spin polarisation process that proceeds under coupling rather than an nOe type pathway as exhibited by DNP.

The metal complex plays a key part in SABRE. It was predicted that the efficiency of the hyperpolarisation of SABRE depends on the lifetime of the metal complex; this further led to the prediction of greater efficiencies being expected with a strongly electron-donating N-Heterocyclic carbene ligand than phosphine ligands.[42, 43] This will be explained in more detail later on. Once both the substrate and *para*hydrogen are bound to the catalyst, the transfer of the polarisation can take place. The role of the substrate is to receive polarisation from the polarised *para*hydrogen derived hydrides (as seen in Figure 9). Once polarisation has been transferred, the magnetically labelled substrate dissociates from the catalyst enabling the build-up of polarisation in the unmodified chemical material. This is then examined by NMR methods which produces signals several orders of magnitude larger than would normally be obtained.[16] The build-up of polarisation is important when choosing the substrate, as the substrate is required to weakly bind to the metal centre so it can dissociate easily allowing the polarisation to build up in the surrounding solution. For the SABRE process to take place, *para*hydrogen is required as a polarisation source. Theoretically, at 295 K with a 400 MHz ^1H NMR frequency, we could achieve signals up to 31,208 times more intense than the corresponding thermal signals.[44]

In the literature, SABRE can be used for a multitude of applications including trace analysis of a substrate.[45] Within the Duckett group, research has focused on areas such as; determining different biologically-active substrates that can be enhanced using SABRE,[46] synthesising NHCs with an Ir-O bond to determine the SABRE efficiency of catalysts in different solvents to improve on the polarisation transfer catalysis (PTC)

precursors[47] and also insight into how different NHC ligands can help provide further insight into the catalytic process that highlights SABRE.[1]

For SABRE to be more efficient it is important to consider factors that will affect the polarisation transfer such as; temperature, the concentration of the substrate, the pressure of pH$_2$ and the steric and structure of the metal complex. The two types of PTCs used and examined within the Duckett group for SABRE are iridium complexes stabilised by phosphine ligands such as PPh$_3$ and PCy$_3$ and carbene ligands such as N-heterocyclic carbenes; Bis-1,3-(2,4,6-trimethylphenyl) imidazolium chloride (IMes) and Bis-1,3-methyl imidazolium chloride (IMe) where they would form a [IrCl(COD)(L)] type complex where L is either the phosphine or the carbene ligand. In 2013, van Weerdenburg et al, reported on using a myriad of N-heterocyclic carbene ligands and how their steric and electronic properties increased the signal enhancement levels.[48] This thesis seeks to examine this.

1.5.2 *N*-Heterocyclic Carbenes

The stability, structure and reactivity of carbenes is very important for the SABRE process, as it is dependent on their steric and electronics effect to increase enhancement levels and stabilises the SABRE-active catalyst.[49] There are two main divisions that classify carbenes and whether they have two paired or unpaired electrons which can determine whether it is a singlet carbene or a triplet carbene (Figure 10).
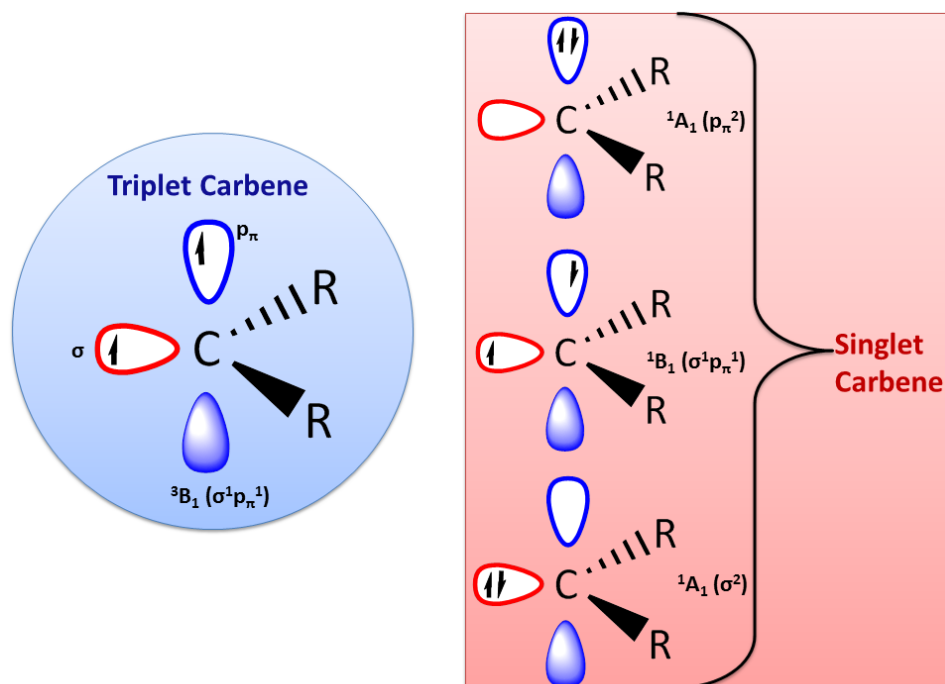
Figure 10: Schematic representation of the electronic configurations of NHC carbenes with the four different forms shown, three being in the singlet state and one being in the triplet state. For the singlet carbenes, the second carbene (middle) shows red sp² orbital with a lone pair. It also shows one electron in the blue p orbital. However, they are spin paired but this singlet carbene would be unstable. The third singlet carbene (below) also has a sp² orbital with two spin paired electrons. It also has a vacant p orbital. In the triplet carbene, there is one unpaired electron in the sp² orbital and one unpaired electron in the p orbital.

There can either be two non-bonding electrons with parallel spins but in two different orbitals known as the triplet state ($\sigma^1 p\pi^1$ configuration) or there are two nonbonding electrons that are paired in either the same or different orbitals ($p\pi^2$, $\sigma^1 p\pi^2$ and σ^2 configurations)[50]. NHCs are known to have a singlet $^1A_1$ ground state (σ^2) abandoning the high energy singlet $^1A_1$ state (p_π^2 configuration) and the only competing electronic states are the triplet $^3B_1$ and the singlet $^1B_1$ electronic states that present single occupied σ and p orbitals.[51]

In the 1960s, Fischer discovered metal alkylidene and alkylidyne complexes, which are referred to as Fischer carbenes, and successfully isolated the first transition metal carbene complex (seen in Figure 11).[52] This was the first successful example of a carbene binding to a central metal. Fischer carbenes are found with metals that have a low oxidation state and are found on the periodic table in the middle to late section of the transition metals which includes metals such as Fe, Cr and W.[53] They bind chemically with the metal centre via the lone pair of electrons within the sp₂ orbitals (σ donation) which donate electrons to the empty d orbital.[54] The π-back bonding occurs from the metal

centre p orbital to the empty p orbital of the carbene carbon (seen in Figure 11). These chemical bonds contribute to the stability of the Fischer carbene complexes.[55]
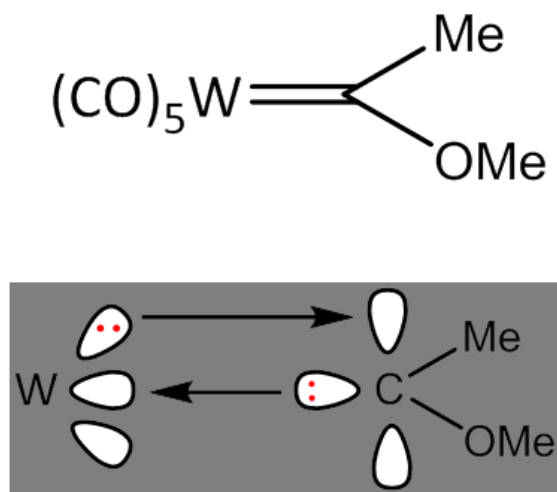
Figure 11: The first Fischer transition-metal carbene complex that was successfully isolated. The section in grey is a representation of Fischer carbenes and highlights the binding that occurs from the sp_2 orbital electrons on the carbon to the empty sp_2 orbital on central metal (W) and the back bonding from the p orbital of metal centre (W) to the empty p orbital of on the carbene carbon.

Another stabilised carbene was discovered by Schrock in the 1970s, where he successfully isolated the first metal methylene complex in the alkylidene family.[56] In contrast to Fischer carbenes, Schrock carbenes are nucleophilic in nature and behave similarly to strong bases, whereas Fischer carbenes are electrophilic due to their vacant π orbital.[57] Unlike Fischer carbenes, Schrock carbenes, seen in Figure 12, are found with high oxidation states and are seen with metals seen in the periodic table in the early transition metal sections like Ti and Ta. Schrock carbenes are formed when the metal centre forms two covalent bonds with carbon by coordinating with strong donor ligands which are non π-acceptors therefore there is no π backbonding.
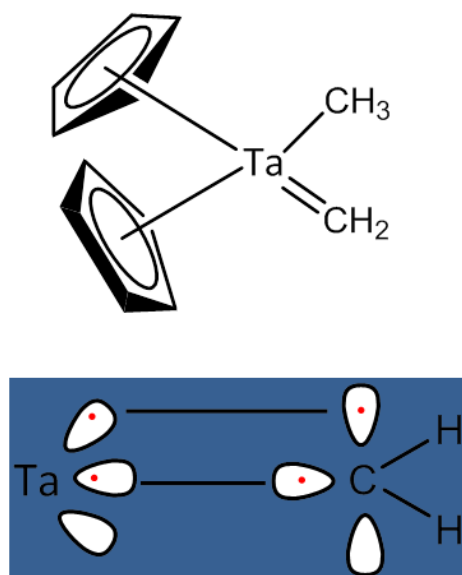
Another type of stabilised carbene which forms the basis of this thesis is persistent carbenes, formally known as *N*-Heterocyclic Carbenes (an example seen in Figure 13). NHCs are neutral compounds with most based on a five-membered ring. The central metal stabilised by these NHCs can vary along with the ring size and shape.
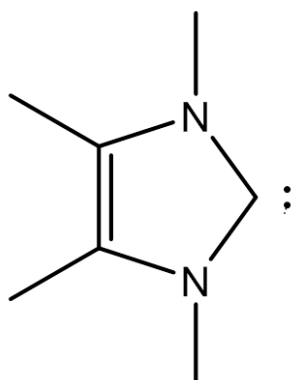
Figure 13: Example of an generic NHC - Imiazol-2-ylidenes

N-Heterocyclic Carbenes (**NHC**) became the forefront of metal carbene research when they were first discovered back in the 1960's. They are defined by their divalent carbon atom with a six-electron valence shell, and attempts were made to synthesise them as early as 1835.[58, 59] However it was not until the late 1980s that the isolation and characterisation of a free, uncoordinated carbene became known.[57] In a seminal paper published in 1988, Bertrand reported the preparation of the first isolable carbene

stabilized by interactions with phosphorus and silicon substituents.[57, 60] This was then followed a few years later by Arduengo *et al*, who were the first to report on a stable isolable crystalline carbene with a nitrogen heterocycle incorporated.[59] Both Ofele and Wanzlick stated that heterocyclic carbenes can be synthesised from imidazolium salts forming stable, electron-rich complexes with specific transition metals in the early 1960s. It was this hypothesis which caused a monumental explosion in experimental work on NHCs which led to the remarkably stable and relatively simple synthesis of the first free stable NHC 1,3-di(adamantly)imidazole-2-ylidene (IAd), seen in Figure 14, by Arduengo *et al*.[59]
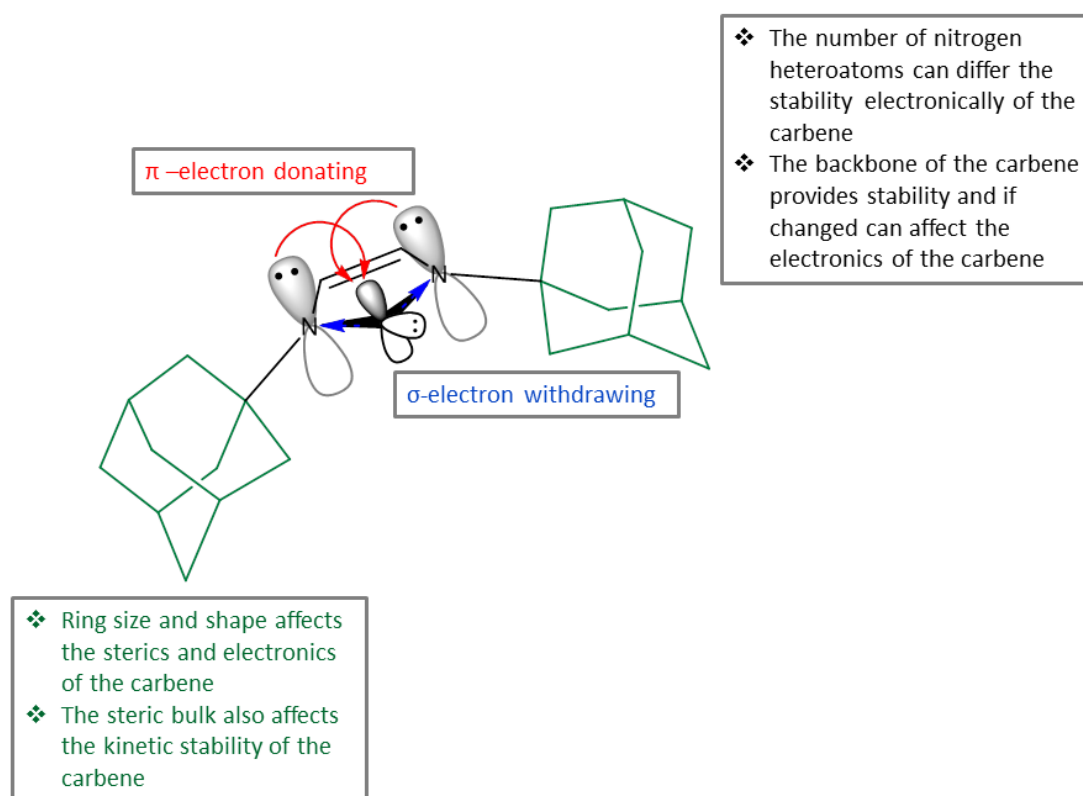
Figure 14: General structural features of the first NHC (IAd) which details some of the key features of an NHCs such as the ring size, shape, nitrogen substituents which affects stability; picture adapted by Hopkinson et al.[57]

There are now many different types of carbene compounds, which differ structurally according to their ring size and the aromatic substituents they bear which can be either symmetric or asymmetric in nature.[61] These differences can affect the electronics and sterics of the NHC but the general representation includes a carbene carbon and two nitrogen atoms in the imidazolium ring (as seen in Figure 14). NHCs are bent carbenes, with frontier orbitals that are sp^2 hybridised and a p-orbital orthogonal to the sp^2 plane called σ and p$_\pi$; with the 5-membered ring of the basic skeleton of an NHC adapting a

planar shape. They generally have a bulky side chain adjacent to the imidazolium ring that helps to improve the kinetic stability of the complex.

Other carbenes, such as those of Bertrand, who in 2005, reported the synthesis of stable cyclic (alkyl)-(amino) carbenes (CAACs) which instead of the two nitrogen atoms seen in the NHCs, contains a more electronegative amino substituent.[62] The CAAC ligands are more electron-rich than phosphine and the other NHC ligands.[62] However, NHCs provide more robust and stable active catalysts when used as ligands with transition metals rendering them more suitable to the work that will be discussed in this thesis.[62, 63]

The nitrogen atoms also provide kinetic stability due to their π-electron donating and σ-electron withdrawing nature. This provides stability by lowering the energy of the σ-orbital and donating the electron density to the empty p-orbital.[57] NHC ligands form stronger bonds with metal centres than other ligands (such as phosphine) and this is due to their strong σ-electron donating properties.[64] This also prevents decomposition of NHC catalysts. All these features are beneficial and contribute to NHCs renowned recognition in organometallic chemistry, especially as NHCs can be used to support ligands in late transition metal catalysis with d block elements such as iridium.[65]

Some of the most commonly used classes of NHCs include imidazolylidene, imidazolinylidene, and benzimidazolylidene.

To characterise these NHCs for medical and chemical applications, NMR (Nuclear Magnetic Resonance) is applied.

1.5.3 Steric and Electronic effects of NHCs

N-Heterocyclic carbenes have been used as powerful two-electron donor ligands forming stable complexes with many metals.[66] By looking at the electronic and steric effects, we are able to determine the catalytic efficiency of the metal complexes.

Electronic effects

As previously stated, singlet carbenes have a filled and a vacant orbital so they possess amphiphilic characteristics, whereas triplet carbenes can be regarded as di-radicals as they have two unpaired electrons.[67] The influence of substituents on the carbene will have a large effect on the electronic and sterics of the molecule. There are two types of electronic effects known as inductive and mesomeric. With the inductive effect, the σ-electron donating groups reduce the energy gap between the s and p_π orbital facilitating the triplet state, while the σ-withdrawing group stabilise the σ orbital, leaving the pπ orbital unchanged, causing the energy gap to increase between the two orbitals favouring the singlet state carbene.[50, 68] The other type of electronic effect is mesomeric effects,

seen in Figure 15, where substituents interact with the carbene centre and are classified as either π-electron-donating or X (-Cl, -PR$_2$, -F) or as π-electron-withdrawing or Z (-BR$_2$, -CN, -PR$_3^+$).
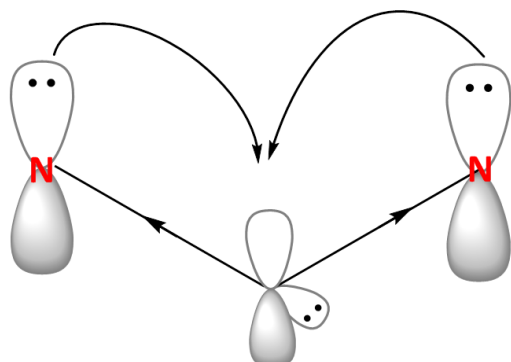
Figure 15: Schematic diagram showing mesomeric effect that occurs in imidazole-2-ylidenes, π-electron-donating substituent, which is the imidazolium ring seen in many carbenes, especially IMes, IXy and ITol and provides stability for the complexes.

Steric Effects

Steric effects can dictate the ground state spin multiplicity if the electronic effects are insignificant. Having bulky substituents on a carbene provides kinetic stabilisation and by increasing the steric bulk of the carbene substituents, this broadens the carbene bond angle favouring the triplet state.[69] The best way to stabilize carbenes kinetically is to protect the reactive carbene centre by increasing the bulky substituents; for the imidazole-2-ylidene type carbenes that are used throughout this thesis we see a two π-donor σ-withdrawer substituents where the carbene electron deficiency is reduced by the donation of the two nitrogen lone pairs while the carbene lone pair is stabilized by the inductive effect of the two electronegative nitrogen atoms.[50] NHCs provide the ability to be able to diversify the electronic and steric properties by varying the *N*-bonded substituents allowing access to tune these properties as you wish.[51]

1.5.4 SABRE catalysts

As previously stated, the SABRE process is very reliant on the design of the SABRE catalyst as it catalyses the transfer of polarisation from the parahydrogen hydrides to the substrate.[40] Therefore the carbene ligand needs to have stable optimal electron-donating characteristics to improve the SABRE efficiencies. The ligand surrounding the metal centre must be able to allow the metal centre to easily bind to *para*hydrogen hydride ligands and other components without interfering. Initially, Duckett *et al* used a cationic iridium complex with the general formula [Ir(COD)(PR$_3$)$_2$]BF$_4$ with R representing Ph, p-tolyl and p-C$_6$H$_4$-OMe, seen in Figure 16. The complex with R=Ph reacted with p-H$_2$ and a 2-fold

excess of pyridine forming $[Ir(PPh_3)_2(py)_2(H)_2]^+$ which was then characterised by NMR showing the dominant hydride signal at δ -21.64 in a ^1H NMR spectrum, with the two hydrides *trans* to pyridine.[5]
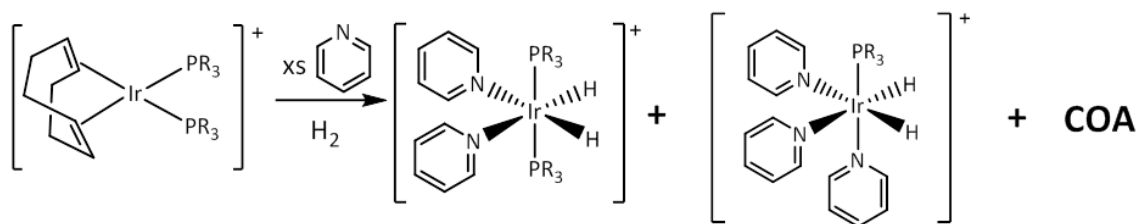
Figure 16: The reaction of [Ir(COD)(PR$_3$)$_2$]$^+$ with excess pyridine and H$_2$ forming the SABRE-active complex [Ir(H)$_2$(PR$_3$)$_2$(py)$_2$]$^+$ and [Ir(H)$_2$(PR$_3$)$_3$]$^+$ with COD hydrogenating to form COA which is no longer bound to the iridium complex.

There was also evidence of a small amount of a second complex $[Ir(PR_3)(py)_3(H)_2]^+$ *cis* by a second hydride signal was seen at δ −21.81. When p-H_2 replaced H_2 the hydride signals of both complexes became PHIP enhanced. Further work was examined to identify that $[Ir(H)_2(PPh_{3\,3})(py)_3]^+$ had significantly more rapid H_2 exchange when compared with $[Ir(H)_2(Ph)_2(py)_2]^+$.[70] The complex that gave the greatest enhancement was however formed with PCy$_2$Ph, which was better than PCy$_3$, this is due the more electron rich phosphine having better H_2 exchange but poorer ligand exchange because of the sterics pushing the ligands off.[16] This in turn draws a link between the exchange rate, electronic and steric properties of the ligand and the SABRE hyperpolarisation level of the complex. Furthermore, the effect of the phosphine on the rate of exchange of the equatorial bound pyridine was determined. At 335 K, $[Ir(H)_2(PR_3)_2(py)_2]^+$ with R = p-C_6H_4-OMe exhibited the faster rate constant at 0.82s^{-1} compared to the other R = Ph complexes showing that this complex, with the greatest electron-rich phosphine has a faster rate of exchange.[70] This exchange occurred between the pyridine (py) ligand *trans* to the hydride and the free pyridine in solution. Also this study showed that the exchange in $[Ir(H)_2(PR_3)(py)_3]^+$ was faster than in $[Ir(H)_2(PR_3)_2(py)_2]^+$ specifically with R = p-tolyl, however the exchange was not seen in 335 K as the complex started to decompose over temperatures higher than 308 K.[70]

Once the link between electron donation of the ligand and the SABRE enhancement of the substrate were found, the first NHC containing complex used for SABRE , IrCl(COD)(IMes) [IMes= (1,3-bis(2,4,6-trimethyl-phenyl)imidazole-2-ylidine)], was explored. This catalyst, derived from Crabtree's catalyst, is used for an array of hydrogenation reactions.
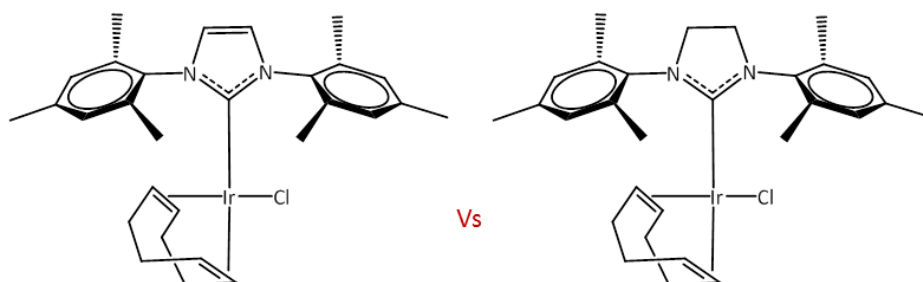
Figure 17: Representative examples of IMes (left) and SIMes (right) catalysts used for SABRE.

It was reported that IrCl(COD)(IMes) is a much better SABRE catalyst precursor than the catalyst [Ir(H)$_2$(PCy$_3$)(py)$_3$[BF$_4$] due to the fact that the NHC is a more powerful electron donor. When IrCl(COD)(IMes) is reacted with excess py and H$_2$, [Ir(H)$_2$(IMes)(py)$_3$]Cl is formed which was proven through NMR spectroscopy. However once 3 atm of pH$_2$ and 0.06 mmol of py were added to IrCl(COD)(IMes) in the earth's magnetic field, a signal enhancement of 266-fold relative to a thermal polarized sample at 295 K and 9.4 T was seen which can be compared to the 18-fold increase of [Ir(H)$_2$(PCy$_3$)(py)$_3$](BF$_4$) . By optimising the reaction conditions, for example, the concentration of the substrate (py), enhancements of 503-fold were reached.[1] Another example of a NHC ligand widely used in SABRE is SIMes (1,3-bis(2,4,6-trimethylphenyl)-4,5-dihydroimidazol-2-ylidene). When SIMes is compared to IMes, the change in the backbone to a double bond backbone causes the carbene ligand to take up less space when surrounding the metal centre in addition; the electron donating power of this ligand is increased. The IMes SABRE active complex [Ir(H)$_2$(IMes)(py)$_3$]Cl therefore has a greater signal enhancement than SIMes with 4 equivalents of pyridine at 5498-fold to SIMes SABRE active complex [Ir(H)$_2$(SIMes)(py)$_3$]Cl at 1317-fold.[1] The steric effect is proven by calculating the buried volume of the ligands which for IMes is 33.0% and 34.5% for SIMes.[5]

1.5.5 SABRE solvents

As previously stated, one of the most effective magnetisation transfer catalysts is IrCl(COD)(IMes)[43] which forms the complex [Ir(H)$_2$(IMes)(sub)$_3$][Cl] once it has undergone activation with a substrate and H$_2$. This complex has chemically equivalent hydrides that transfer polarisation efficiently in polar protic solvents such as methanol, however because of the charged nature of the species, it has been proven that the magnetisation

transfer can be less efficient, while the complexes formed tend to be soluble their ligand exchange rates are slower in a range of low polarity solvent used in NMR analysis.[71] Therefore, choosing the right SABRE solvent is very important to the development of SABRE efficient catalysts, therefore one of the solvents used throughout this thesis was the more polar, non-protio solvent, CD_3OD, and the other was the less polar, non-protio solvent, CD_2Cl_2.

1.6 Aims
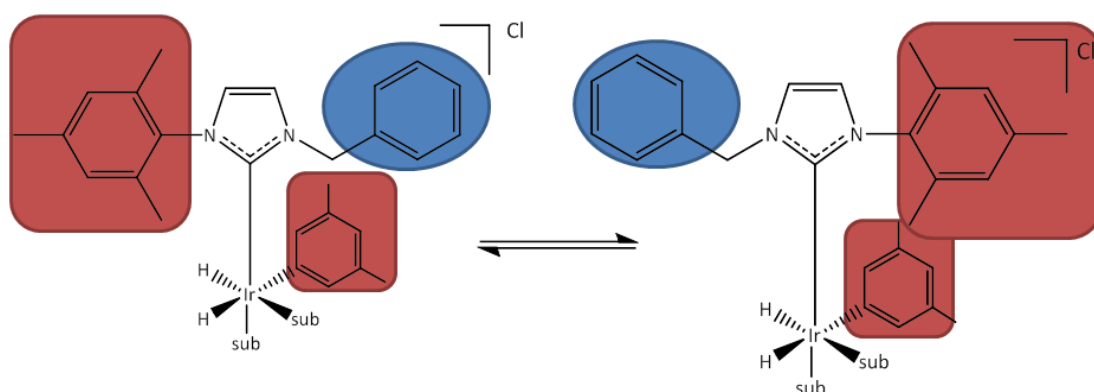
Figure 18: Representative example of asymmetric SABRE active complex [Ir(H)₂(MesCarBenzyl)(3,5-lut)₃]Cl. The red square represents a large ligand while the blue square represents a smaller ligand. Due to the rotation of the complex, this can either allow for a larger or smaller substrate to bind which is determined by the position of the larger or smaller nitrogen substituents.

The aims of this project were to research different homogenous catalysts that could alter the extent of the polarisation transfer for the application of SABRE, with a focus on whether symmetrical or asymmetrical NHCs could improve the polarisation transfer which in turn would produce larger signal enhancements and debate which catalyst was the most efficient for SABRE. This was achieved by:

- ✓ (Chapter 2) - Synthesising symmetric and asymmetric NHC ligands and forming SABRE-active catalysts, with pyridine and 3,5-lutidine as substrates of choice. These substrates are widely used in biomedical applications and therefore were investigated with different symmetric and asymmetric complexes to determine how these different NHCs alter the polarisation transfer. A particular focus into their rates of dissociation were also investigated.
- ✓ (Chapter 3) - Determining and characterising the intermediates that form when the symmetric NHC ligands undergo SABRE and identifying the final SABRE-active

catalyst that form. There was also a focus on how solvents can affect the intermediates and products that form.

- ✓ (Chapter 4) – Investigating and characterising the intermediates and final SABRE-active catalysts that form when varying the asymmetric NHC ligands. Instead of pyridine, 3,5-lutidine was the substrate used in this investigation.

Other variables such as concentration of substrate and temperature of polarisation transfer were investigated throughout this thesis in order to optimise the SABRE process.

This research set out to probe whether an asymmetric or symmetric SABRE active catalyst was the most efficient for SABRE by comparing the signal enhancements and ligand loss rates of the given SABRE active complex with pyridine or 3,5-lutidine as the substrate ligand. Each symmetric and asymmetric complex differ in their electron donating power and their steric bulk and previous research has stated that the ligand design can optimize the catalytic concept of SABRE.[1] From this theory, It can be hypothesised that the symmetric SABRE-active catalyst, $[Ir(H)_2(IXy)(py)_3]Cl$ where IXy = 1,3 -bis(2,6-Dimethylbenzene)imidazol-2-ylidene, due to its size and electron donating power will produce the greater SABRE enhancement and the SABRE catalyst $[Ir(H)_2(PhCarCH_3)(3,5-lutidine)_3]Cl$ which likely has be weakest σ donor will produce the lowest signal enhancements.

In the literature, also seen in Figure 18, it is also stated that the steric effects and size of the NHC and the substrate can also impact the polarisation transfer, which in turn can reduce the total signal enhancements and slow the rate of ligand loss.[1] Therefore, it can also be hypothesised that the larger asymmetric SABRE-active complex, $[Ir(H)_2(MesCarHomoBenzyl)(3,5-lutidine)_3]Cl$, which we would expect to potentially have the largest total signal enhancement, may however produce a much lower total signal enhancement and a slower rate of ligand loss due to the size of the NHC and the substrate, 3,5-lutidine, being a steric hindrance.

2 SABRE Catalyst Design with Pyridine and 3,5-Lutidine as substrates

As stated in section 1.5, SABRE is a hyperpolarisation method where polarisation is transferred from the *para*hydrogen derived hydrides to the substrate molecules that bind to the central iridium atom improving the NMR signals. This could be applied to MRI to improve imaging through the use of pyridine-based polarised biological substances as contrast agents which are less toxic to the body than the contrasting agent, gadolinium. The signal enhancement depends on the magnetic field and the binding kinetics of the substrate through the scalar coupling network, meaning the selection of said substrate is critical to the polarisation transfer and efficiency of SABRE.[72]

2.1 Introduction

Greater SABRE efficiencies were found when the catalyst contains NHC ligands compared to phosphine ligands. As the efficiency depends on the lifetime of the metal complex and the strength of the magnetic field where the polarisation occurs, earlier studies determined that phosphine ligands showed the highest level of polarisation transfer.[57] As previously stated, phosphine ligands were based on the reaction of Crabtree's catalysts, $[Ir(COD)(PCy_3)(py)][BF_4]$ by using pyridine as the substrate and PCy_3, seen in Figure 19, as the phosphine forming $[Ir(H)_2(PCy_3)(py)_3][BF_4]$.[5, 43] Later studies then showed that NHCs ligands had more strongly electron-donating properties.[73]
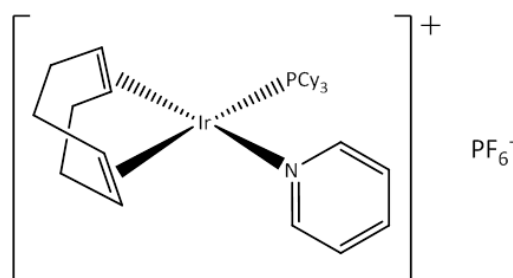
Figure 19: Crabtree's Catalyst, PCy_3= tricyclohexylphosphine.

The most efficient NHC catalyst, 1,3-bis(2,4,6-trimethylphenyl)imidazol-2-ylidene (IMes), seen in Figure 20, currently yields the greatest enhancements making it the most effective used SABRE catalyst within the Duckett group. When an excess of py is added to [IrCl(COD)(IMes)] in the presence of methanol the complex [Ir(COD)(IMes)(py)]Cl is produced. Once hydrogen is added 1,5-cyclooctadiene (COD) hydrogenates at the iridium

centre to cyclooctane (COA). With the addition of p-H$_2$, which replaces hydrogen, polarisation is transferred from the p-H$_2$ derived hydrides to the substrate; which in this case is pyridine forming [Ir(H)$_2$(IMes)(py)$_3$]Cl.
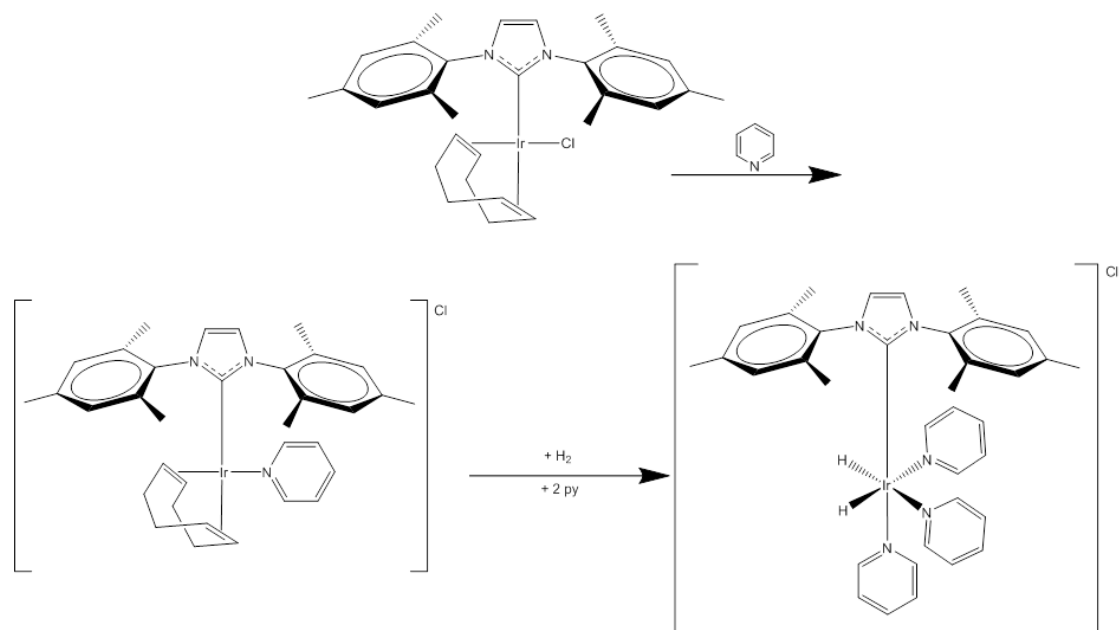
Figure 20: Schematic steps of the formation and activation of [Ir(H)$_2$(IMes)(py)$_3$]Cl. [IrCl(COD)(IMes)] is treated with an excess of py in MeOD forming [Ir(COD)(IMes)(py)]Cl. This then undergoes activation with hydrogen forming the SABRE active catalyst [Ir(H)$_2$(IMes)(py)$_3$]Cl.

The purpose of this study was to analyse new SABRE symmetric and asymmetric active catalysts which differ by their NHC ligands, for example, NHC ligand, 1,3 -bis(2,6-dimethylphenyl)imidazol-2-ylidene (IXy) and 1,3-bis(4-methylphenyl)imidazole-2-ylidiene (ITol). These catalysts were compared to the IMes catalyst. Also in this study, asymmetric complexes were investigated along with pyridine derivatives and compared to symmetric SABRE active catalysts to identify their efficiencies as SABRE active catalysts.

2.2 History of preparing NHCs

As stated previously in section 1.5.2, Arduengo *et al*[74] isolated the first free stable NHC, IAd, and since then many different pathways have been discovered to synthesis the imidazolium salts which become precursors for the NHC ligands used in SABRE. The synthetic pathway used by Arduengo et al in 1999, is the basis for the synthesis of the two

symmetric NHC salts which are precursors to the SABRE active complexes. The synthetic route used by Arduengo is illustrated in Figure 21.
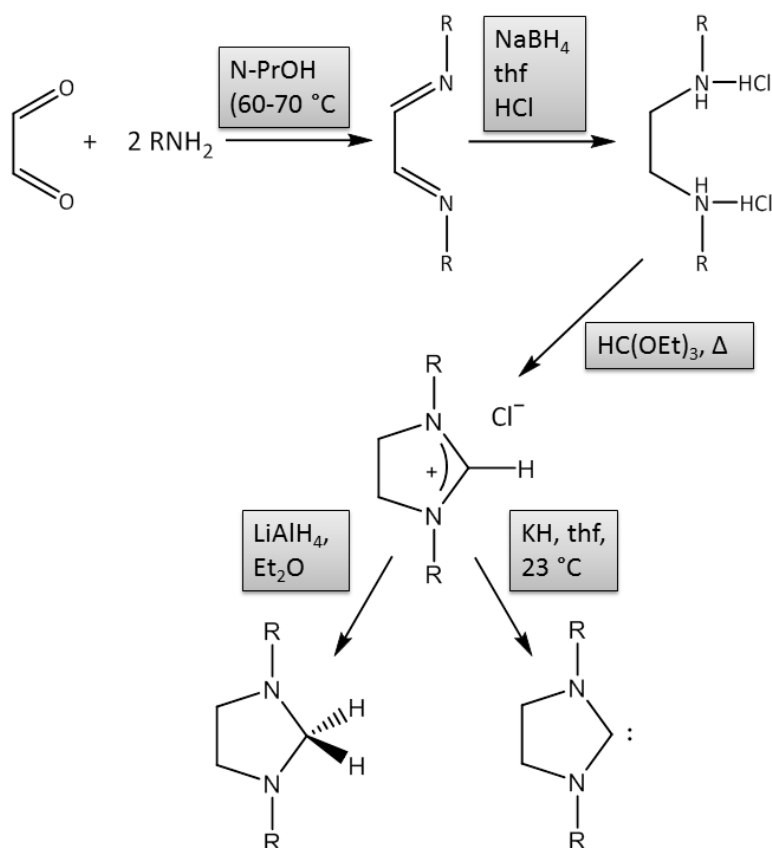
Figure 21: General synthetic pathway use by Arduengo et al[74] to synthesis the unsaturated imidazol-2-ylidenes which further lead to the synthesis of saturated imidazol-2-ylidenes which is further used and adapted to synthesis the new symmetric NHCs, IXy and ITol.

2.3   Synthesis of IrCl(COD)(IXy) (1) and IrCl(COD)(ITol) (3)

	IXy	ITol
R	CH$_3$	H
R$'$	H	CH$_3$
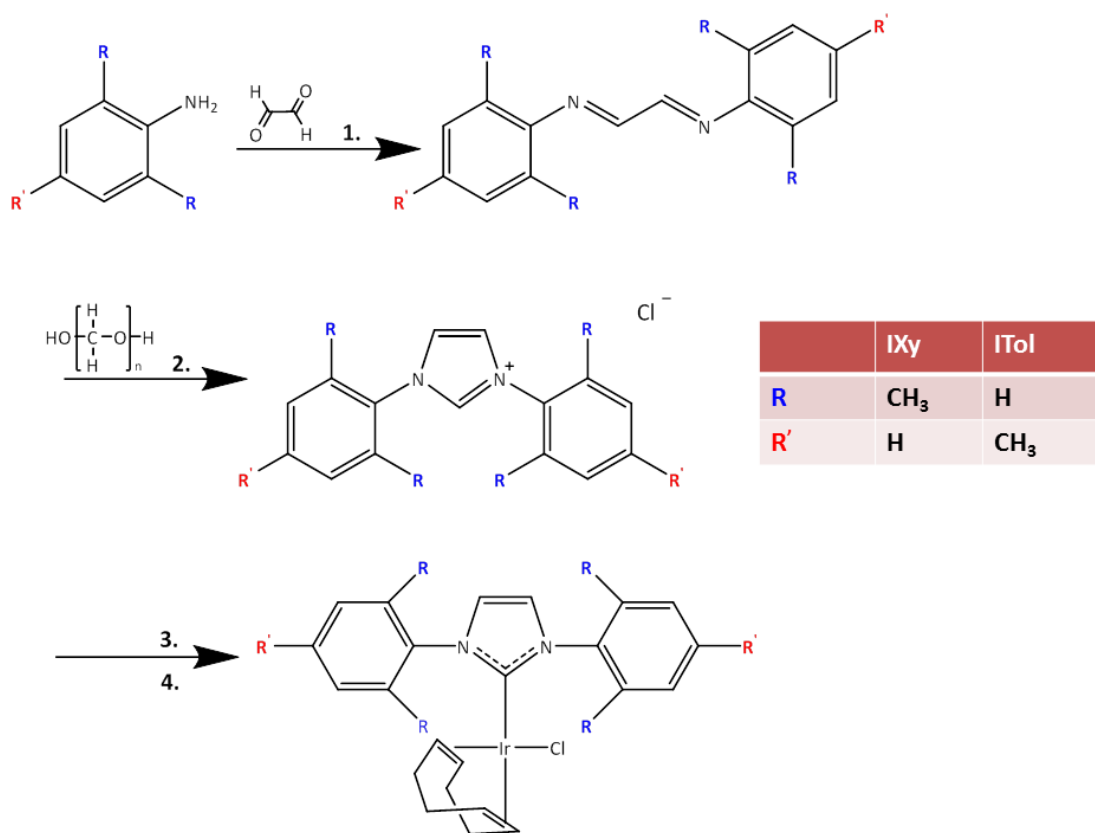
Figure 22: Schematic pathway to show the synthesis of IrCl(COD)(IXy) and IrCl(COD)(ITol). Pathway 1: Addition of formic acid in EtOH at rt for 16h. 2. Addition of HCl in paraformaldehyde at rt for 16h. 3. Imidazolium salt and KO^{t}Bu stirred in THF at rt under N$_2$ for 30 mins. 4. Iridium Dimer [Ir(COD)Cl]$_2$ added to carbene solution under stirring at rt for 2h.

The novel NHC complex, IrCl(COD)(IXy) (**1**) and IrCl(COD)(ITol) (**3**) was synthesised in the laboratories within the Duckett group by following the pathway seen in Figure 22.

2 drops of formic acid and 1.0 equivalent of glyoxal were added and stirred in a solution of aniline (2.0eq.) in MeOH or EtOH. The solution was stirred for 16h at rt forming a yellow precipitate. This precipitate was then filtered and washed with MeOH or EtOH and dried forming the ethylenediimine.

A paraformaldehyde solution (1.1eq.) in 4M HCl (1.5eq.) was added dropwise to the solution of ethylenediimine (1.0eq.) in ethyl acetate at rt under nitrogen with stirring. The solution was then stirred for 16h. The precipitate was filtered and washed with ethyl acetate and dried under a vacuum forming the imidazolium chloride.

The imidazolium salt in Figure 22, after pathway 2 was then added to KO^{t}Bu (2.4eq.) in THF under nitrogen gas at rt. The solution was then stirred for 30 minutes at rt. The

iridium dimer, [Ir(COD)Cl]₂ (1.0eq.) was added to the solute and stirred at rt for 2h. The solvent was removed and the crude product was purified.

This was then fully characterised by ^{1}H, ^{13}C, ^{15}N NMR spectra and ESI-Mass Spectrometry.

2.3.1 Characterisation of IXy and ITol

SABRE requires a carbene ligand which fundamentally has electron donating properties and is chemically and electronically stable enabling the optimal reactivity and efficiency for the hyperpolarisation process. As stated previously, this thesis is based on two new symmetric SABRE catalysts, IrCl(COD)(IXy)]where IXy = 1,3-bis(2,6-dimethylphenyl)imidazol-2-ylidene and IrCl(COD)(ITol) where ITol = 1,3-bis(4-methylphenyl) imidazol-2-ylidene. The full spectroscopic data of both IrCl(COD)(IXy) and IrCl(COD)(ITol) can be found in section 6.4, however the spectroscopic features of an NHC ligand can be exemplified by the key components of this complex which are shown in Table 1, where you can see the key features of the IXy aromatic. Table 2 also provides characterisation data for the ITol aromatic, where the key features of the carbene can be seen. In Table 1, there are two chemical shifts identified for component 1, this is due to the CH_3 groups being in different environments, however NMR does not provide enough information to be able to distinguish between the two CH_3 groups.

	^{1}H NMR δ	^{13}C NMR Δ	^{15}N NMR δ	
1	2.26 ,2.40	19.42, 18.05		
2		137.68, 135.02		
3	7.24	128.06		
4	7.36	128.85		
5		138.64		
6			192.2	
7	7.07	127.70		
8		180.15		

Table 1: ^{1}H, ^{13}C and ^{15}N NMR chemical shifts for the key components of IrCl(COD)(IXy) in CD₂Cl₂

	^{1}H NMR δ	^{13}C NMR δ	^{15}N NMR δ	
1	2.48	20.90		
2		129.02		
3	7.99	125.34		
4	7.36	128.60		
5		137.95		
6	7.34	121.40		
7			195.8	
8		180.8		
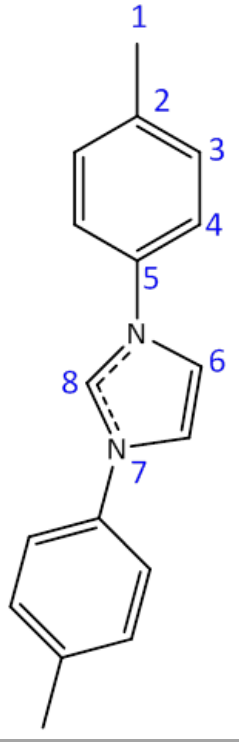
Table 2: ^{1}H, ^{13}C and ^{15}N NMR chemical shifts for the key components of IrCl(COD)(ITol))in CD_2Cl_2

2.4 Synthesis of IrCl(COD)(MesCarBenzyl)]Cl (12) and IrCl(COD)(MesCarHomoBenzyl) (14)
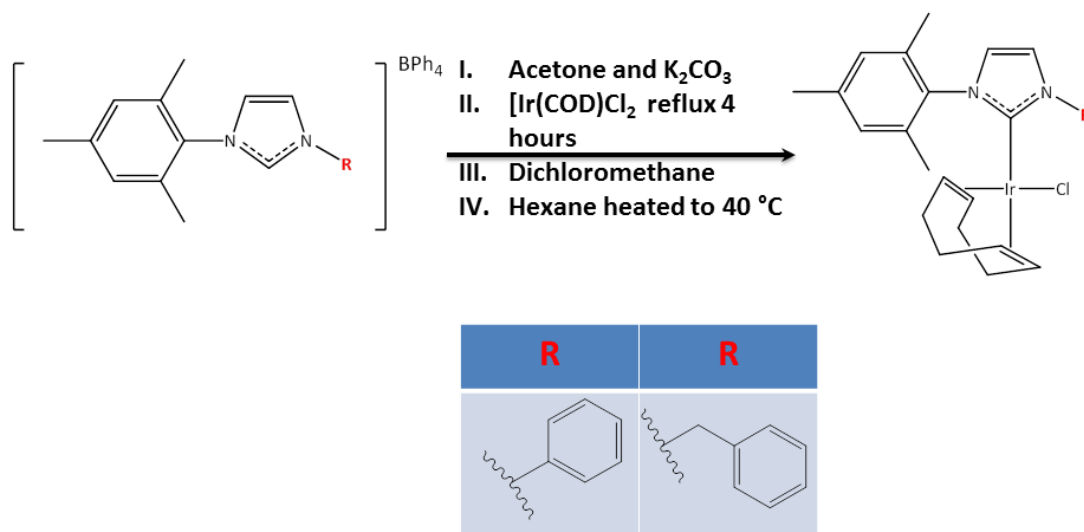
Figure 23: Schematic pathway to show the synthesis of IrCl(COD)(MesCarBenzyl) and IrCl(COD)(HomoBenzyl). Pathway I: dissolved in acetone and K_2CO_3 and stirred. II. Addition of [Ir(COD)Cl$_2$] dimer and refluxed for 4 hours. III. Filtered and dissolved in dichloromethane. 4. Filtered and dissolved in hexane and heated to 40 °C for 15 minutes. The complex was then further purified by repeating steps 4 and filtering and evaporating the solvent until 10 mL of solution is left.

The new NHC complexes, IrCl(COD)(MesCarBenzyl) and IrCl(COD)(MesCarHomoBenzyl) were synthesised in the laboratories within the Duckett group by following the pathway seen in Figure 23.

[MesCarBenzyl](BPh$_4$) (101 mg, 0.170 mmol) or [MesCarHomoBenzyl](BPh$_4$) (107 mg, 0.176 mmol) were dissolved partially in acetone (20 mL). For [MesCarBenzyl](BPh$_4$), K_2CO_3 (127 mg, 0.920 mmol) and for [MesCarHomoBenzyl](BPh$_4$), K_2CO_3 (127 mg, 0.0917 mmol)   was added and stirred for 15 minutes at room temperature prior to the addition of [Ir(COD)Cl]$_2$ (57.2 mg, 0.0852 mmol) for [MesCarBenzyl](BPh$_4$) and[Ir(COD)Cl]$_2$ (59.0 mg, 0.0878 mmol). The mixture was heated at reflux for 4 hours, forming an orange-yellow colour. After cooling to room temperature, the mixture was filtered and evaporated to give an orange-yellow residue. The residue was re-dissolved in

dichloromethane (20 mL), whereby white solid precipitates out. The mixture was filtered through celite and the solvent was evaporated to give an orange-yellow solid. The solid was then re-dissolved in hexane (30 mL) and heated while stirring in a water bath at 40 °C for about 15 minutes. The yellow solution was filtered and the resulting suspension collected. These two steps were then repeated twice more until only a small amount of brown solid remains. The collected yellow solution was then combined and reduced in volume to *ca.* 10 mL. The solution was cooled in the freezer overnight to give yellow needle-like crystals. This was then fully characterised by ^{1}H, ^{13}C, ^{15}N NMR spectra and ESI-MS and the details for this are found in section 6.4.

2.5 Substrate

The first substrate used to observe SABRE was pyridine,[16] which binds to the iridium metal centre via the lone pair on the nitrogen atom. Earlier studies exemplified that greater hyperpolarisation levels were achieved with bulky *N*-Heterocyclic carbenes. At present, the NHC ligand with the greatest transfer of hyperpolarisation thus providing the greatest SABRE enhancement is IrCl(COD)(IMes) which is reported to give a total polarisation enhancement of 8100-fold on the NMR resonances of the free pyridine. [Ir(H)$_2$(IMes)(py)$_3$]Cl is the SABRE-active catalyst, once activation with *para*-H$_2$ has occured.[43]
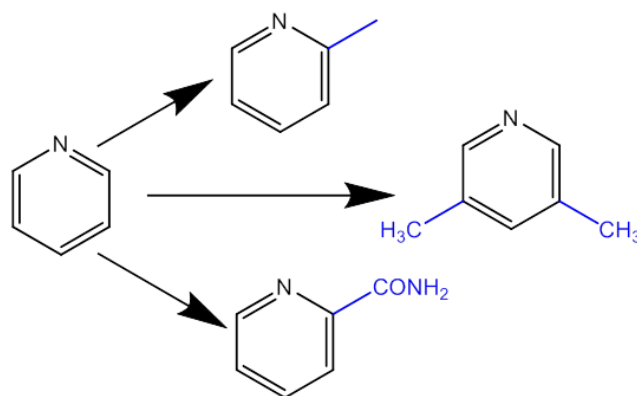
Figure 24: Pyridine and pyridine derivative compounds, picoline, 3,5 – lutidine and niacin (adapted from Altaf et al.[75])

Pyridine and its derivatives (seen in Figure 24) are reported in many different biological activities and compounds that play a vital role clinically and in medicinal applications.[75]

As pyridine was first used to observe SABRE, it will become a substrate of interest. We will also observe SABRE for 3,5-lutidine due to its uses in the manufacture of new generation anti-ulcer drugs such as Omeprazole and Esomeprazole.[76] As pyridine binds readily to the iridium catalyst and has a big impact on SABRE due to its efficiency and exchangeable

protons, I will seek to use pyridine and another pyridine derivative as the substrate and expand on the effect changing the NHC ligand has on polarisation transfer.

2.6 Forming symmetric SABRE-active catalysts

The new symmetric SABRE complexes, which I will be examining in more detail in section 3 and 4, both form SABRE active complexes determined as $[Ir(H)_2(IXy)(py)_3]Cl$ and $[Ir(H)_2(ITol)(py)_3]Cl$.

2.6.1 IrCl(COD)(IXy) and IrCl(COD)(ITol)

When IrCl(COD)(NHC) is dissolved in CD_3OD a yellow solution is produced. When pyridine is added, the chloride ligand is displaced by pyridine to form $[Ir(COD)(IXy)(py)]Cl$ or Ir(COD)(ITol)(py)]Cl, Figure 25. Both of these products are colourless and hence it is possible to monitor the activation reaction by visually inspecting the sample and observing a colour change from yellow to colourless.
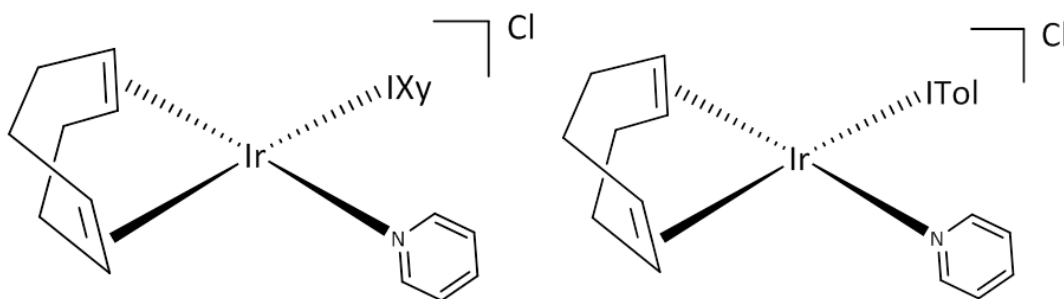
Figure 25: The IXy and ITol complexes formed once added with excess pyridine in deuterated methanol. This is the precursor complex to the SABRE active complexes that are formed once activation with *para*hydrogen has occurred.

2.7 Exchange Rates of Symmetric and Asymmetric SABRE-active complexes

As previously stated, once the SABRE-active complex $[Ir(H)_2(NHC)(sub)_3]Cl$ forms it undergoes SABRE. Hyperpolarisation is transferred from the *para*hydrogen derived hydrides to the substrate which, for the symmetric complexes, is pyridine and for the asymmetric complexes is 3,5-lutidine.This indicates that both complexes undergo dissociative ligand exchange whereby the bound and free substrates continuously exchange. Cowley *et al* showed that by changing the temperature the polarisation levels for the free substrate changed suggesting, there was an optimal ligand exchange rate for polarisation.[43]

The rates of pyridine and 3,5-lutidine dissociation were investigated by monitoring the exchange of the corresponding proton ligand signals in the bound substrate *trans* to hydride. We are unable to observe the exchange of the bound pyridine and 3,5-lutidine ligands positioned trans to the NHC. This would suggest that there is stronger metal bonding interaction to the nitrogen centre when *trans* to the carbene rather than the hydride. This effect has been rationalised previously.[77]

A ^{1}H EXSY (exchange spectroscopy) method was used to observe the exchange process. These measurements started at 263 K where slow exchange was evident. The temperature was then increased up to 313 K. Practically, this involved recording multiple selective 1-D NOESY spectra at different temperatures as a function of the reaction time, as specified by d_8 (mixing time) in the pulse programme. Integrals of the bound and free pyridine substrate signals were determined for each d_8 value. Rate constants for ligand exchange were then determined by plotting the mixing time (d_8) against the peak integrals which were expressed as percentage amount. These data were simulated using a differential kinetic mode and the solver analysis in Microsoft Excel.[78]

Table 3 shows the temperature where ligand exchange rates of 2 was monitored and the rate constants determined for each temperature.

[Ir(H)$_2$(IXy)(py)$_3$]Cl (2)	
Temperature (K)	**K_d (s^{-1})**
263	0.085
273	0.464
283	2.11
293	8.29
298	12.10

Table 3: Kinetic and thermodynamic data showing the ligand loss of pyridine for [Ir(H)$_2$(IXy)(py)$_3$]Cl (4).

When a similar study was completed for the SABRE active ITol complex, [Ir(H)$_2$(ITol)(py)$_3$]Cl, no ligand loss was observed. This must indicate that the process is slow and not visible out to 1 second, which is the maximum d_8 value used. This is expected with [Ir(H)$_2$(ITol)(py)$_3$]Cl as the absence of methyl at the NHC rings 2 and 6 position destabilizes the complex. Where as, [Ir(H)$_2$(IXy)(py)$_3$]Cl addition of methyl at the NHCs rings 2 and 6 positions, now provide stability to the complex against ligand loss. Hence these changes have merit.

For the asymmetric complexes with the ligands now being 3,5-Lutidine, the exchange rate constants were determine and shown in Table 4.

K_d (s^{-1})			
[Ir(H)$_2$(NHC)(sub)$_3$]Cl	298 K	303 K	313 K
[Ir(H)$_2$(PhCarCH$_3$)(3,5-lut)$_3$]Cl	0.337	0.530	
[Ir(H)$_2$(MesCarCH$_3$)(3,5-lut)$_3$]Cl	1.01	1.89	
[Ir(H)$_2$(HomoBenzyl)(3,5-lut)$_3$]Cl	1.19	3.70	10.80
[Ir(H)$_2$(IMes)(3,5-lut)$_3$]Cl	19.6	26.5	

Table 4: Kinetic and thermodynamic data showing the ligand loss of 3,5-Lutidine for [Ir(H)$_2$(PhCarCH$_3$)(3,5-Lut)$_3$]Cl, [Ir(H)$_2$(MesCarCH$_3$)(3,5-Lut)$_3$]Cl, [Ir(H)$_2$(MesCarHomoBenzyl)(3,5-Lut)$_3$]Cl and [Ir(H)$_2$(IMes)(3,5-Lut)$_3$]Cl

From these exchange rates shown in Table 4, we can determine that at 298 K, the rate constant for IrCl(COD)(PhCarCH$_3$) is the slowest at 0.337 s^{-1}, whereas the catalyst, IrCl(COD)(IMes), has the fastest exchange rate at 2.100 s^{-1}. At 303 K, this also follows the same trend with [Ir(H)$_2$(PhCarCH$_3$)(3,5-lut)$_3$]Cl still having the slowest exchange at 0.530 s^{-1} and [Ir(H)$_2$(IMes)(3,5-lut)$_3$]Cl with the highest exchange rate at 26.51 s^{-1}. However we are unable to observe [Ir(H)$_2$(IMes)(3,5-lut)$_3$]Cl at 313K as the exchange is occurring too quickly and the only catalysts where exchange is observed at 313 K and [Ir(H)$_2$(HomoBenzyl)(3,5-lut)$_3$]Cl with a rate constant at 10.800 s^{-1}.

If we were to compare the symmetric and asymmetric complexes, which although use different substrate ligands but are in the same 5 equivalent of substrate, at 298 K, [Ir(H)$_2$(IMes)(3,5-lut)$_3$]Cl has the fastest ligand exchange at 26.5100 s^{-1}. From the literature with 4 equivalents of py, we can even determine that [Ir(H)$_2$(IMes)(py)$_3$]Cl has the fastest ligand exchange rate at 23 s^{-1} .It is assumed that this is due to the NHC having more electron donating properties therefore observing this faster exchange.

2.7.1 Thermodynamic data for pyridine and 3,5 lutidine

Once the rate constants are determined for each catalyst, we are able to calculate the Gibbs free energy, $\Delta G^{\ddagger}$, by using the Eyring-Polanyi Equation, which in turn calculates the enthalpy, $\Delta H^{\ddagger}$, and the entropy, $\Delta S^{\ddagger}$, which is explained in more detail in section 7.2. Given the number of points however, only $\Delta G^{\ddagger}_{298}$ will have any meaning.

[Ir(H)$_2$(NHC)(sub)$_3$]Cl	$\Delta G^{\neq}_{298}$ (kJ/Mol)
[Ir(H)$_2$(PhCarCH$_3$)(3,5-lut)$_3$]Cl	76
[Ir(H)$_2$(MesCarCH$_3$)(3,5-lut)$_3$]Cl	73
[Ir(H)$_2$(HomoBenzyl)(3,5-lut)$_3$]Cl	73
[Ir(H)$_2$(IMes)(3,5-lut)$_3$]Cl	65

Table 5: Thermodynamic data showing the ligand loss of 3,5-lutidine for [Ir(H)$_2$(PhCarCH$_3$)(3,5-lut)$_3$]Cl, [Ir(H)$_2$(MesCarCH$_3$)(3,5-lut)$_3$]Cl, [Ir(H)$_2$(MesCarHomoBenzyl)(3,5-lut)$_3$]Cl and [Ir(H)$_2$(IMes)(3,5-lut)$_3$]Cl and with pyridine for [Ir(H)$_2$(IXy)(py)$_3$].

The loss of 3,5-lutidine, from [IrCl(COD)(PhCarCH$_3$)] therefore has the highest barrier with that for IMes being the smallest. The difference in $\Delta G^{\neq}_{298}$ across the series is 11 kJ/Mol which is substantial and demonstrates that the potential to gain control of SABRE in this way is important.

2.8 **Summary**

This chapter describes new symmetric and asymmetric complexes and how they have been synthesised as a SABRE pre-catalyst. We have examined the rates of ligand loss from [Ir(COD)(NHC)(sub)]Cl by using 1D selective NMR methods and seen how steric interactions with the NHCs promote ligand exchange. Based on these exchange rates, it is hypothesised that [IrCl(COD)(HomoBen)] based systems will give the greatest SABRE enhancements and hence be the most efficient for the SABRE with sterically encumbered 3,5-lutidene.

3 SABRE with symmetric *N*-Heterocyclic carbene complexes

3.1 IrCl(COD)(IXy) (1)

The following section describes the reaction steps that took place during the formation of [Ir(H)$_2$(IXy)(py)$_3$]Cl to examine whether the SABRE efficiencies improve when varying the NHC ligand. Two new NHC ligands, known as IXy and ITol, are reacted with pyridine and hydrogen in two different solvents and monitored to determine the effects the solvents and the NHC ligands have on magnetisation transfer efficiency.

3.1.1 Reaction and Reactivity of 1 with py in CD$_2$Cl$_2$

Complex **1** was dissolved in CD$_2$Cl$_2$ at 294 K with a 5-fold excess of pyridine relative to **1** which produced a yellow coloured solution. There is no evidence, in the associated ^{1}H NMR spectra of this solution, that pyridine (py) binds to the metal centre because the signals for **1** remain at the original positions. Hence, Cl is not displaced by py to form the ionic complex [Ir(COD)(IXy)(py)]Cl. This is illustrated in Figure 26, where peaks for the *meta* and *para* -CH proton signals of the IXy aromatic component appear at δ 7.24 as well as those of the *ortho* methyl groups at δ 2.26 and δ 2.40. The ^{1}H NMR spectrum also shows COD with the corresponding CH proton peaks at δ 3.01 and δ 4.07. Resolved -CH$_2$ proton peaks appear at δ 1.34 and δ 1.71. The other labelled peaks on Figure 26, correspond to the solvent at δ 5.35, δ 2.05 for acetone, δ 7.10 for the CDCl$_3$ contaminant in the solvent and free pyridine peaks at δ 8.71, 7.82 and 7.42 on the spectra.

It was hypothesised that an increase in concentration would change the equilibrium of the reaction and therefore pyridine may bind more easily under these conditions. When various concentrations of pyridine were tested with IrCl(COD)(IXy), 0.66µL (1 equivalent) and 1.97µL (3 equivalents, 0-fold excess), no binding of pyridine was observed in CD$_2$Cl$_2$.

NMR spectra for complex **1** were also acquired at 233 K to see if the coordinated pyridine peaks were visible at lower temperatures due to better peak resolution. Therefore **1** was dissolved in CD$_2$Cl$_2$ with 5 equivalents of pyridine. However, the NMR spectrum showed that even at lower temperature, the coordinated pyridine that should be seen near the region of the free pyridine peaks at around δ 7.50 are not visible. The lack of reaction of **1** in CD$_2$Cl$_2$, is uncommon as we expect pyridine to bind to the metal centre, however we suggest this occurs due to the low polarity of the solvent, which has been proven to reduce efficiency of SABRE complexes.[71]
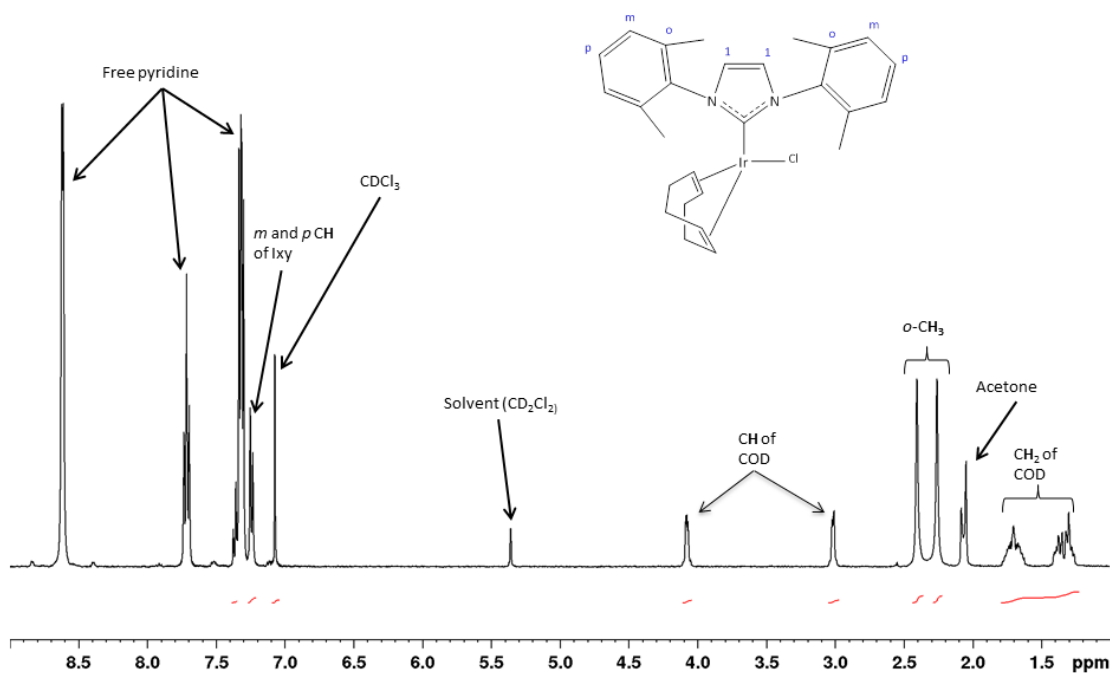
Figure 26: A 32 scan ^{1}H spectra of IrCl(COD)(IXY) (5mg, 8.17μmol) with 5 equivalents of py (3.29μL, 40.8μmol) in 600μL of CD$_2$Cl$_2$ at 400 MHz at a temperature of 294 K. The geometry of this Ir(I) 16 electron complex, IrCl(COD)(IXy) is the square planar conformation seen in chapter 6.4.1.

3.1.2 Reaction of 1 with py in CD$_3$OD

As CD$_2$Cl$_2$ proved to be unsuccessful we changed to the more polar and solvating CD$_3$OD with 5 equivalents of pyridine at 243 K; in the aromatic region of the corresponding ^{1}H NMR spectrum, the following changes were observed:

The ^{1}H NMR signals of the coordinated pyridine are now observed at δ 7.30 for the *meta* proton and δ 7.88 and 7.82 for the *ortho* and *para* protons as shown in Figure 27. It also showed that the *ortho* methyl groups on the IXy aromatic ring are further apart in the proton spectra containing CD$_3$OD. The C-H proton peaks of COD are also different in CD$_3$OD as they appear much closer together in the ^{1}H spectrum. The *meta* and *para* protons on the IXy aromatic appear to stay approximately in the same position on the proton spectrum, in both CD$_2$Cl$_2$ and CD$_3$OD.

The other unaccounted for peaks refer to the residual solvent at δ 5.49 and 3.34 and also the free pyridine peak seen in the aromatic region. The evidence suggests that the labile Cl is replaced by pyridine and [Ir(COD)(IXy)(py)]Cl (**1a**) forms.

We expected to see this reaction due to pyridine having a lone pair of electrons on the nitrogen atom that it can donate to the complex, [IrCl(COD)(IXy)], therefore binding one pyridine molecule to the metal centre.[1] This ultimately leads to Cl loss.
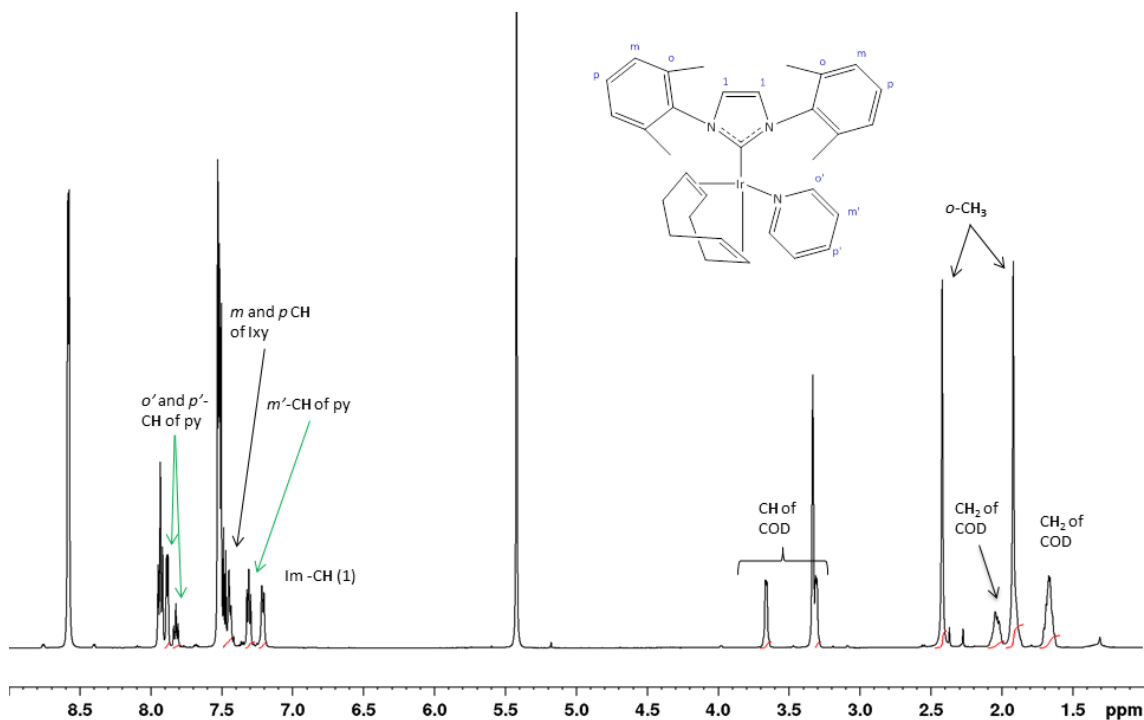
Figure 27: A 32 scan ^{1}H spectrum of IrCl(COD)(IXy) (5mg, 8.17μmol) with 5 equivalents of py (3.29μL, 40.8μmol) in 600μL in CD$_3$OD at 400 MHz and at a temperature of 243 K forming [Ir(COD)(IXy)(py)]Cl; showing activated peaks for the IXy catalyst and the bound pyridine protons.

3.1.3 Reaction of 1 with py and H$_2$ in CD$_2$Cl$_2$ at 233 K

3.1.3.1 Initial H$_2$ addition to IrCl(COD)(IXy)

When hydrogen was added to **1** with an excess of py (5 equivalents) in cold CD$_2$Cl$_2$ (approximately 233 K), the colour changed from yellow to colourless over a 24 hour period, indicating that a reaction was occurring. The hydride region of the resulting ^{1}H NMR spectrum is shown in Figure 28. It contains two pairs of hydride resonances which are all chemically inequivalent to each other indicating the formation of two products. These resonances appear at δ −12.05 and −17.55 for one pair of hydride resonances and the other pair of hydride resonances appear at δ −13.42 and −18.08 with the lower field signals having a chemical shift that is indicative of being *trans* to a soft ligand while the higher field shifts are commensurate of ligands that lie *trans* to pyridine. Appleby *et al* stated the chemical shifts for a similar complex where the intermediates of IrCl(COD)(IMes) and pyridazine and phthalazine as substrates were monitored and the diagnostic hydride resonances were assigned at around δ −14 and −18.[46]

There are 4 diagnostic alkene resonances at δ 3.99 and 2.99. The other two resonance alkene peaks are at δ 3.58 and 3.21 in the complex IrCl(H)$_2$(COD)(IXy)(py). When pyridine has resonances at δ 7.88, 7.82 and 7.30 and two hydride resonances are considered, 5 groups within the octahedron have been accounted for. The sixth group, the NHC, yields a diagnostic imidazole resonance at δ 7.07. This complex is further characterised in chapter 6.4.

These products were identified as **1b** and **1c** respectively by multinuclear NMR methods. The first product formed was [Ir(H)$_2$(COD)(IXy)(py)]Cl (**1c**) with the corresponding hydride signals are at -12.05 and -17.55, however, there is also another set of hydride singlet peaks at δ -13.42 and -18.08, these correspond with the complex [IrCl(H)$_2$(COD)(IXy)] (**1c**). From the relative peaks intensities in Figure 28, we can see that [Ir(H)$_2$(COD)(IXy)]Cl has a higher concentration in this solution, however this could not be seen in 1 scan ^{1}H NMR and so a 32 scan spectrum was recorded.
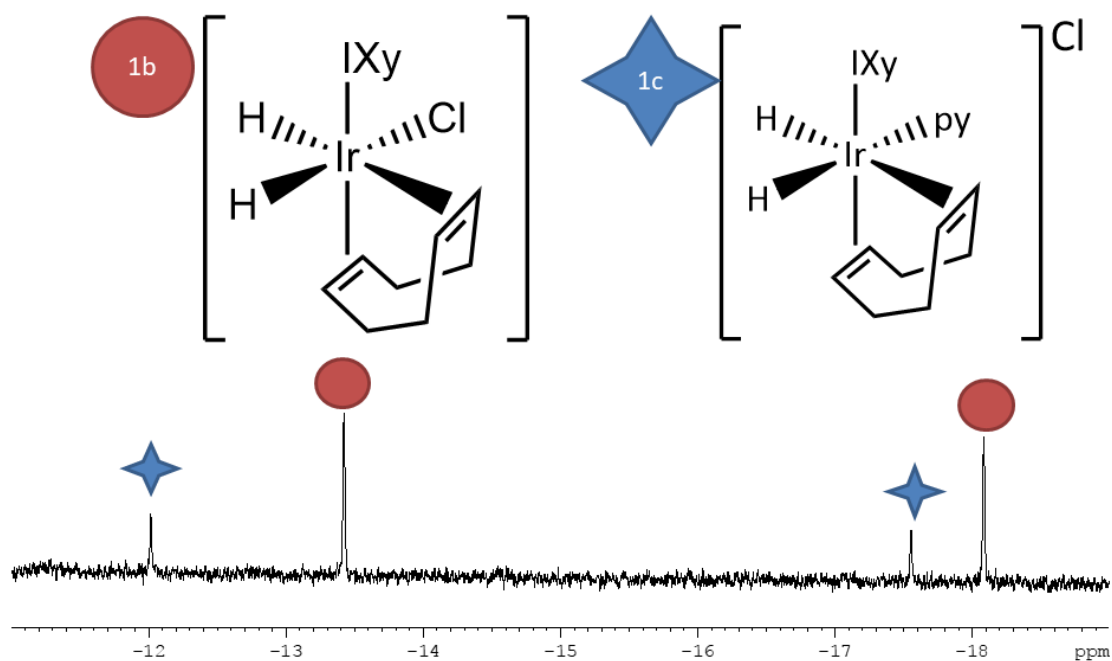
Figure 28: ^{1}H NMR spectrum of hydride resonance peaks corresponding to the formation of [Ir(H)$_2$(IXy)(COD)(py)] and IrCl(H)$_2$(IXy)(COD) that form once hydrogen gas at 3 bar pressure is added to the sample before NMR analysis.

[Ir(H)$_2$(IXy)(py)$_3$]Cl does not form at 233 K, we do however observe free pyridine peaks at δ 8.71, 7.82 and 7.42 that show polarisation with a 386-fold signal enhancement. This indicates that [Ir(H)$_2$(IXy)(COD)(py)] is SABRE active.

3.1.4 **Reaction of 1 with py and H₂ in CD₂Cl₂ at 298 K**

3.1.4.1 Initial H₂ addition and hydride migration in [Ir(H)₂(COD)(IXy)(py)](Cl)

Upon warming to 298 K, the formation of the desired SABRE active catalyst is observed. Furthermore, a colour change from yellow to clear as the reaction proceeds was observed. COD hydrogenates to COA as the SABRE active complex [Ir(H)₂(IXy)(py)₃]Cl forms .

When hydrogen was initially added to a solution of **1** with 5 equivalents of pyridine in CD₂Cl₂. Complexes **1b** and **1c** observed at 233 K were also observed in the solution at 298 K with corresponding hydride signals for **1b** appearing at δ −13.50 and −18.10 and for **1c** seen at δ −12.06 and −17.60.

3.1.4.2 *Formation of [Ir(H)₂(IXy)(py)₃]Cl*
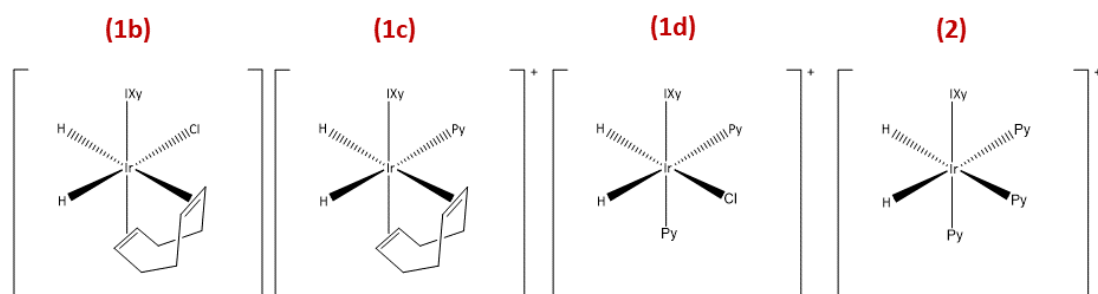
Figure 29: IXy complexes formed by the addition of *p*-H₂ and substrate (pyridine) to (1) in CD₂Cl₂ at 298K. IrCl(COD)(IXy) (5mg, 8.17μmol) was dissolved in CD₂Cl₂ with 5 equivalents of pyridine (3.29μL, 40.8μmol).

Para-H₂ (3 bar) was added to a solution containing [Ir(COD)(IXy)(py)]Cl in CD₂Cl₂ with a 2-fold excess of pyridine. A 1 scan thermal ¹H NMR spectrum was recorded after shaking for 10 seconds at about approximately a 65 G magnetic field. From this, initially multiple products were identified (seen in Figure 29).

The complexes can be identified by ¹H NMR spectroscopy and yield two coupled hydride resonances. In the case of **1b**, these lie at δ −13.63 (H lies *trans* to COD) and −17.93 (where H lies *trans* to Cl). Complex **1c** gives hydride signals at δ −12.27 (H lies *trans* to COD) and −17.59 (where H lies *trans* to py). In this reaction, we also observe the resonance for COA, which occurs when COD hydrogenates to COA and dissociates from the complex and this occurs in both complexes **1d** and **2**. Complex **2** has equivalent hydrides and the corresponding ¹H NMR signal is a singlet at δ −22.76. Complex **1d** has inequivalent hydrides giving resulting signals at δ −23.73 and −24.37 (H *trans* to Cl).

Initially, when *para*-H_2 is added all four complexes, seen in Figure 29, were observed in a 1 scan ^1H spectrum, however after about 20 minutes, only complexes **1d** and **2** can be seen. The SABRE active catalyst **2** comprises 97% of the mixture, with 3 % chloride complex, **1d**. After 10 seconds of shaking the NMR tube at an approximate 65 G magnetic field and dropping into the NMR spectrometer, the major SABRE active catalyst showed 425-fold total proton enhancement in free pyridine molecules. The enhanced ^1H NMR spectrum is seen in Figure 30, with the corresponding free and bound pyridine signals showing typical SABRE type enhancements previously described. This reaction is typical for SABRE–active complexes such as IMes.[46]
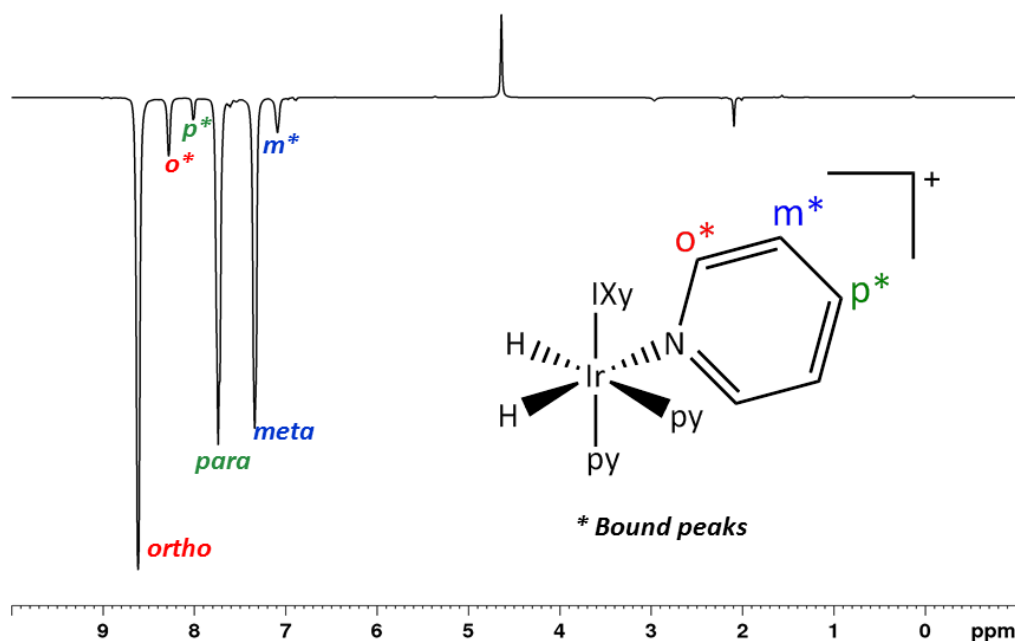
Figure 30: ^1H NMR spectrum of the SABRE active IXy complex, seen in 2, [Ir(H)₂(IXy)(py)₃]Cl. This complex forms after activation with *para*hydrogen, shaken for 10s at approximately 65 G. During this reaction, COD falls off hydrogenates to COA and pyridine binds to the iridium metal centre forming the *tris*-IXy complex. Polarisation is transferred from the *para*hydrogen derived hydrides to the substrate, pyridine.

3.1.5 Reaction of 1 with py and H₂ in CD₃OD at 233 K

3.1.5.1 Initial H₂ addition and hydride migration in IrCl(H)₂(COD)(IXy)(py)

The SABRE precursor, [Ir(H)₂(IXy)(COD)(py)]Cl in CD₃OD, was formed when hydrogen was added to a solution containing **1** with 5 equivalents (2-fold excess) of pyridine at 233 K. The sample is shaken for about 10 seconds outside the spectrometer and a ^1H NMR spectrum was immediately acquired. The resulting peaks for the two chemically inequivalent singlet hydrides at δ -12.16 and -17.42 which couple to each other in the ^1H NMR spectrum seen in Figure 31. These hydride signals correspond with the complex **1c**. It is also possible to observe a small hydride peak at δ −22.42 which corresponds to the

SABRE active complex, $[Ir(H)_2(IXy)(py)_3]Cl$ (**2**) also seen in Figure 31, however to a much lesser extent. Signals for **1b** are not seen due to the rapid formation of $[Ir(COD)(IXy)(py)]Cl$.
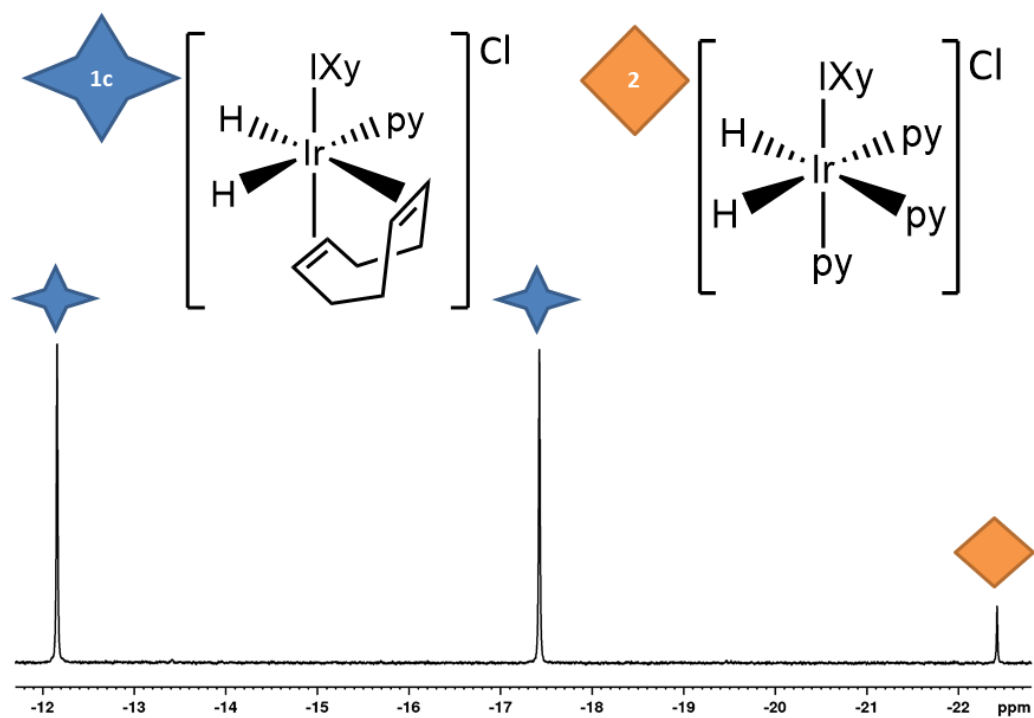
Figure 31: ¹H HMR spectrum of the hydride region corresponding to [Ir(H)₂(COD)(IXy)(py)]Cl at 233K in CD₃OD.

3.1.5.2 *Formation of [IrCl(H)₂(IXy)(py)₃]Cl*
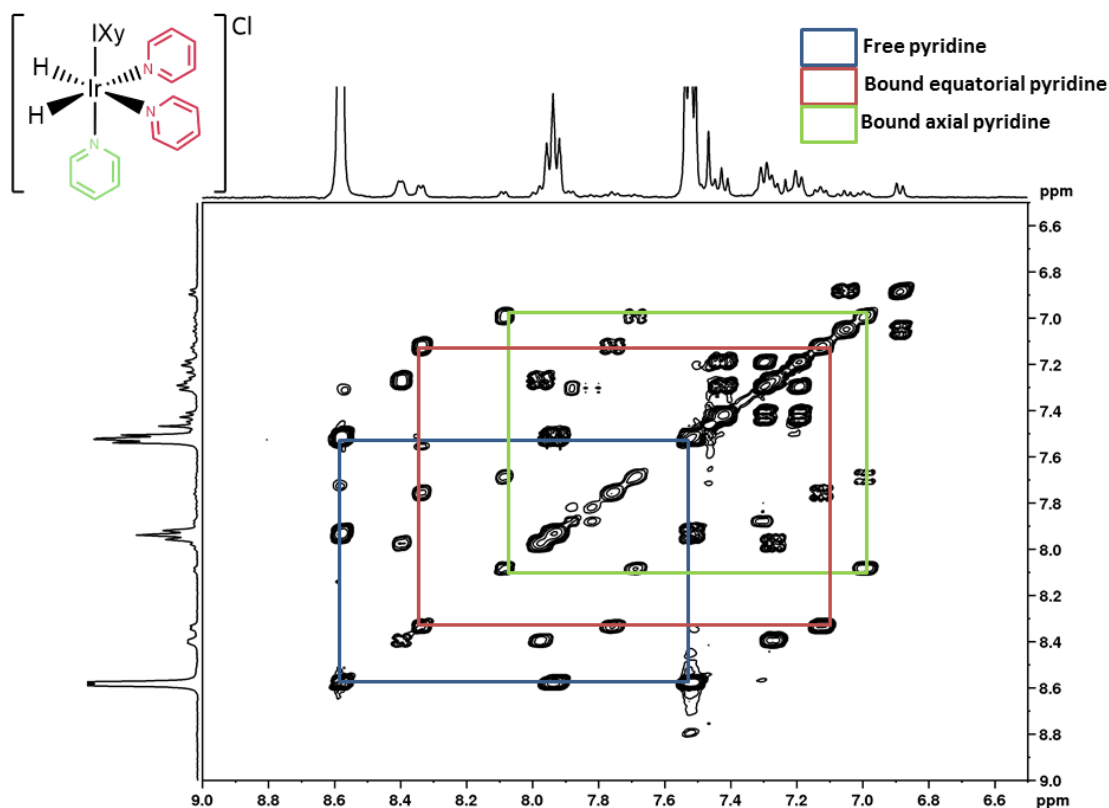
Figure 32: ¹H COSY NMR spectrum showing the bound and free pyridine of the SABRE active complex [Ir(H)₂(IXy)(py)₃]Cl (4). The blue square shows the three free pyridine peaks for the *ortho*, *para* and *meta* proton peaks within this solution. The red square shows the three bound pyridine peaks for both equatorial pyridines, with the *ortho*, *para* and *meta* protons being observed at the same chemical shift for each equatorial pyridine bound to the complex. The green square shows the three bound axial pyridine proton peaks that are correlated to each other, being the *ortho*, *para* and *meta* proton peaks.

3 bar of *para*-H₂ is added to the NMR tube and placed in a cold dry-ice acetone solution at 233 K for 3 minutes. The NMR tube is then shaken for 10 seconds in a 65 G magnetic field and a 1 scan ¹H NMR spectrum is acquired. In the ¹H NMR spectrum the equivalent hydride signal at δ −22.76 corresponds to the SABRE active complex **2** with 3 pyridines bound to the complex. The ¹H COSY NMR spectrum, seen in Figure 32, shows the region of the substrate, pyridine, where we can identify the pyridine resonances that correspond to the SABRE active complex. The blue square corresponds to signals at δ 8.58, 7.93 and 7.53, and these peaks are all identified as the free pyridine in solution where δ 8.58 is the *ortho*, δ 7.93 is the *para* and δ 7.53 is the *meta* peaks for the free pyridine. The ¹H COSY NMR spectrum helps us to identify which protons are correlated to each other, helping us to distinguish the structure of the complexes in the solution. We can also see that the red

and green squares are proton peaks in the same complex as they show correlation to the equivalent hydride peak seen at δ −22.76. The red square shows the correlation between the bound equatorial pyridine protons which are seen at δ 8.34 for the *ortho* pyridine protons, δ 7.75 for the *para* pyridine protons and δ 7.13 for the *meta* pyridine protons. The green square indicates that this is the bound *axial* pyridine peak and the corresponding chemical shifts for the *ortho* pyridine protons are seen at δ 8.09, for the *para* protons are seen at δ 7.69 and for the *meta* proton peaks at δ 6.98. The SABRE active catalyst, **2**, was fully characterised by NMR and this can be found in section 6.4.5.

3.1.6 Reaction of 1 with py and H$_2$ in CD$_3$OD at 298 K

3.1.6.1 *Initial H$_2$ addition to IrCl(COD)(IXy)(1) and hydride migration in IrCl(H)$_2$(COD)(IXy)(2)*

Usually, when a SABRE complex undergoes hydrogen addition, hydride complexes are detectable with a single ^{1}H NMR spectrum; this is because signals are not broadened through exchange processes so we are able to identify them clearly. IrCl(COD)(IXy) is dissolved in CD$_3$OD with 5 equivalents of pyridine, we observe the formation of **1b**, then hydrogen is added at 3 bar pressure and we would expect to see the formation of **1c**. Initially, from a 1 scan ^{1}H NMR spectrum there was no evidence for the formation of complex **3** but there was evidence that hydrogen was in solution by identifying a single peak at δ 4.5. A 32 scan ^{1}H NMR was also performed; however we were unable to observe the precursor, **1c**.

3.1.6.2 Reaction of IrCl(COD)(IXy) (1) with py and p-H₂ and formation of [Ir(H)₂(IXy)(py)₃](Cl) (4)
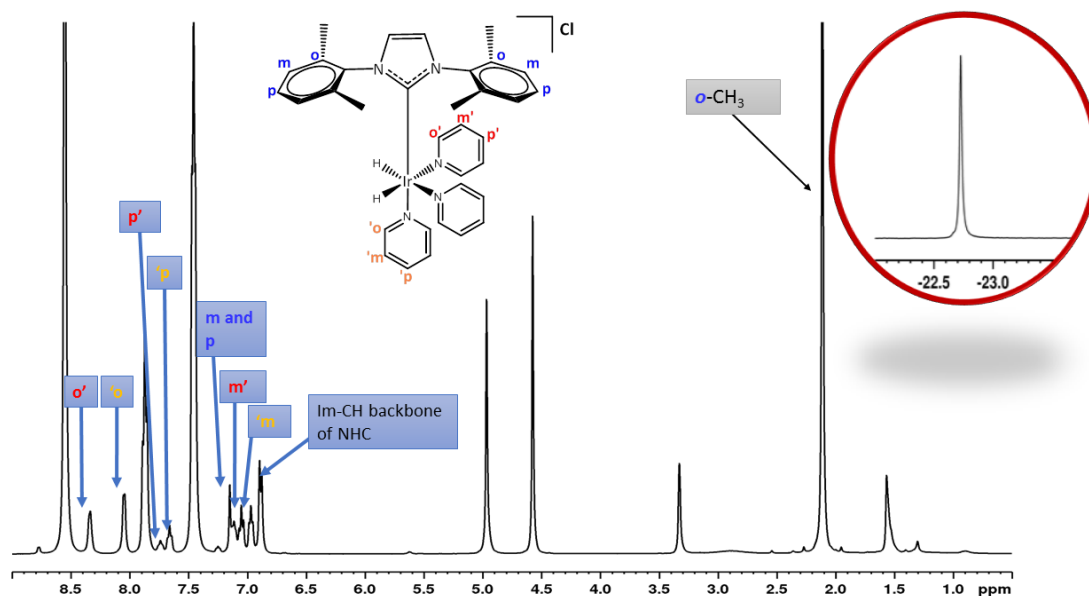
Figure 33: ¹H NMR spectrum of the SABRE active complex, [Ir(H)₂(IXy)(py)₃]Cl, that forms with a 5 equivalents (2-fold excess) of pyridine in CD₃OD. In this spectrum, one clear hydride signal is observed at around δ −22.8 which indicates that once the reaction has fully activated in CD₃OD only one clear *tris* complex forms.

Upon the addition of hydrogen to CD₃OD solutions containing [Ir(COD)(IXy)(py)]Cl, it was not possible to see complex **1c** forming at 298 K, this could be due to the rotation of the complex occurring too slowly resulting in signal broadening and the fast pyridine exchange.

Once *p*-H₂ was added to the solution and the sample shaken at an approximate 65G magnetic field, we observe antiphase hyperpolarised hydride signals for **1c** at δ -12.40 and -17.50. It was also possible to observe the formation of **2** with a corresponding equivalent hydride signal at δ-22.76. After repeating the shake and drop method for about 15 minutes, complex **1c** can be observed slowly reducing in concentration until it is no longer present in solution and the only remaining complex left is **2**. In Figure 33, we can also observe peaks for the pyridine *trans* to the hydride peaks at δ 8.34 for the *ortho* bound pyridine protons, δ 7.74 for the *para* bound pyridine protons and δ 7.12 for the *meta* bound pyridine protons. For the bound pyridine *trans* to the NHC, we observe chemical shifts at δ 8.06, 7.67 and 6.91. The peaks remaining are for the NHC, IXy, where the corresponding proton peaks are observed for the *meta* and *para* protons at δ 7.15 and for the *ortho* CH₃ peak at δ 2.15, and the peaks not annotated are for the solvent

peak at δ 5.0, the hydrogen peak at δ 4.5 and the product when COD hydrogenates to COA which is observed at δ 1.5.

The maximum signal enhancement, seen in Figure 34, on the *ortho* protons of the pyridine was 102-fold (shaken at 65G with a 3-fold excess of pyridine). Previous publications have reported the *para*, *meta* and *ortho* proton peaks of pyridine are enhanced in the negative part of the spectrum.
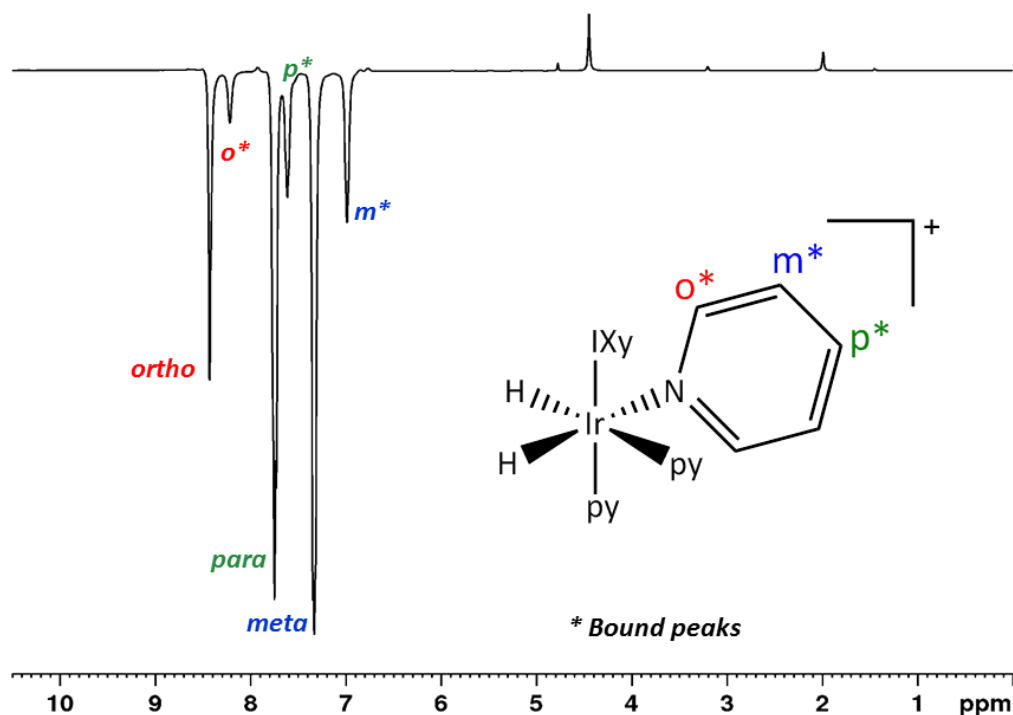
Figure 34: A 1 scan hyperpolarised ¹H NMR spectrum, showing both the free and bound pyridine peaks as antiphase signals, indicating that complex 4 does undergo SABRE hyperpolarisation.

3.2   IrCl(COD)(ITol) (3)

Previously in section 2.3, the synthesis and characterisation of the NHC, IrCl(COD)(ITol) was explained. In this section, we will discuss how the IrCl(COD)(ITol) complex reacted with pyridine and H_2 and hypothesise that a SABRE active complex forms but due to the less bulky substituents on the NHC, that the SABRE efficiency may not be as strong as the IXy catalyst.

3.2.1 Reaction of 3 with py in CD₂Cl₂

Complex **3** (5mg, 8.56 µmol) was dissolved with 5 equivalents of pyridine (3.45 µL, 42.8 µmol), in 600 µL of CD_2Cl_2. The solution changed from a light yellow to a dark yellow once pyridine was added. There was however, no evidence that pyridine binds to the iridium

centre in the associated ¹H NMR spectrum provided in Figure 35, as the resonances remain in the original positions. We are able to identify, in Figure 35, the free pyridine resonances of the *ortho*, *para* and *meta* protons at δ 8.60, 7.73 and 7.34. The NMR spectrum also shows the *meta* –CH of the ITol aromatic NHC at δ 7.99 and the *ortho*-CH resonance overlapping with the imidazolium backbone at δ 7.31. The COD signals are illustrated in Figure 35, at δ 4.35 for the CH of COD and the CH_2 of COD are seen at δ 1.82, 1.45 and 1.22. The *para* CH_3 of the ITol aromatic component is identified at δ 2.48, leaving the last unlabelled peak corresponding to the solvent at δ 5.35.

Complex **3** was also tested with pyridine in various concentrations at 1 equivalent (0.69 µL) and 3 equivalents (2.07 µL) and at various temperatures of 243 K and 266 K, however we were still unable to observe pyridine binding to the metal centre in CD_2Cl_2. This low reactivity is unusual as we expect to see pyridine bind to the metal centre. As previously stated, this could be due to the low polarity of the solvent which is known to affect the formation of SABRE-active complexes.[71]
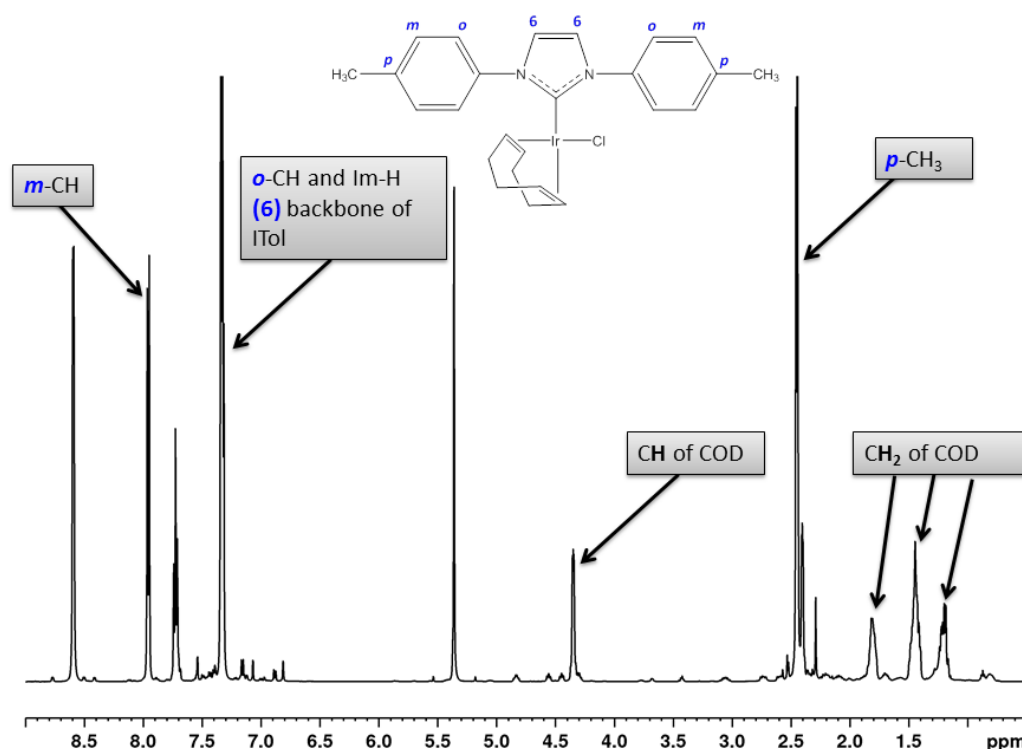
Figure 35: A 32 scan ¹H spectrum of [IrCl(COD)(ITol) (5mg, 8.17µmol) with 2-fold excess of py (3.29µL, 40.8µmol) in 600µL of CD_2Cl_2 at 400 MHz and at a temperature of 243K; showing the peaks of the ITol catalyst before undergoing activation. The geometry of this structure IrCl(COD)(IXy) adopts the square planar conformation seen in chapter 6.4.7.

We are also able to observe a very small amount of a CH activated complex, seen in Figure 36, which corresponds to the very small signals, which is originally seen in the

starting material for complex **3** and yields a corresponding hydride signal at δ -17.17. We are able to identify this as a C-H activated product due to similar CH activated products in the literature.[79]
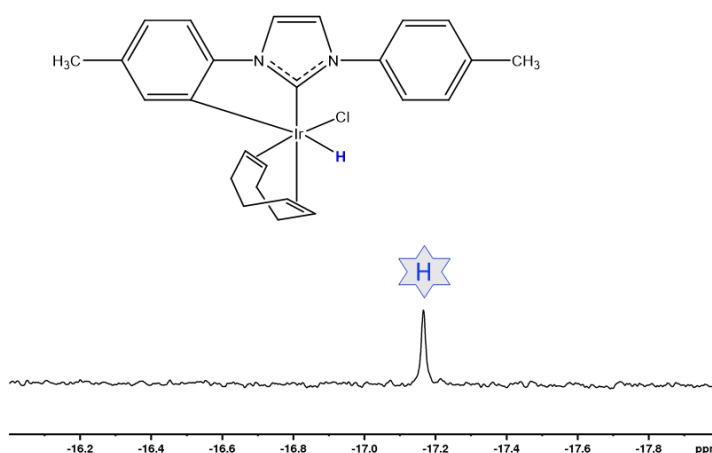
Figure 36: A ^{1}H NMR spectrum of the hydride region corresponding to the CH activated product of ITol, IrCl(H)(COD)(ITol)].

3.2.2 Reaction of 3 with py in CD$_3$OD

Once CD$_2$Cl$_2$ was found to be an unsuitable solvent for the formation of [Ir(COD)(ITol)(py)]Cl, CD$_3$OD was used instead due to its greater polarity as the solvent. A solution containing **3** was dissolved in CD$_3$OD with 5 equivalents of pyridine to see if the complex [Ir(COD)(ITol)(py)]Cl was able to be observed. However, once again we were unable to observe pyridine binding to the metal centre, even when temperatures of 243 K and 263 K were used. Different concentrations of pyridine were also added but the binding of pyridine was not observed. Due to the starting material having a small amount of the CH activated product shown previously in Figure 36, the solution containing **3** with 5 equivalents of pyridine in CD$_3$OD also containing the CH activated product seen with CD$_2$Cl$_2$, with corresponding hydride signals at δ −17.09.

3.2.3 Reaction of 3 with py in H$_2$ in CD$_2$Cl$_2$ at 298 K

3.2.3.1 *Initial H$_2$ addition of 5 and hydride migration in IrCl(H)$_2$(COD)(ITol)*

We previously stated that there was no evidence that the precursor complex [Ir(COD)(ITol)(py)]Cl forms once pyridine is added to complex **3** in CD$_2$Cl$_2$ at 298 K. Hydrogen was then added to the solution and shaken outside of the magnetic field so that it dissolves within the solution, we are not able to observe the formation of

IrCl(H)$_2$(COD)(ITol). However, what we can observe, seen in Figure 37, is the SABRE active complex, [Ir(H)$_2$(ITol)(py)$_3$]Cl (**4**), in a higher concentration to the CH activated product already in solution. The corresponding hydride signal for the SABRE-active *tris* complex is observed at δ -24.11, while the CH activated product remains at a low concentration with the corresponding hydride signals found at δ -17.17. Due to the CH activated complex **3a** increasing in solution once hydrogen gas was added, the complex is fully characterised by for ^{1}H NMR in section 6.4.
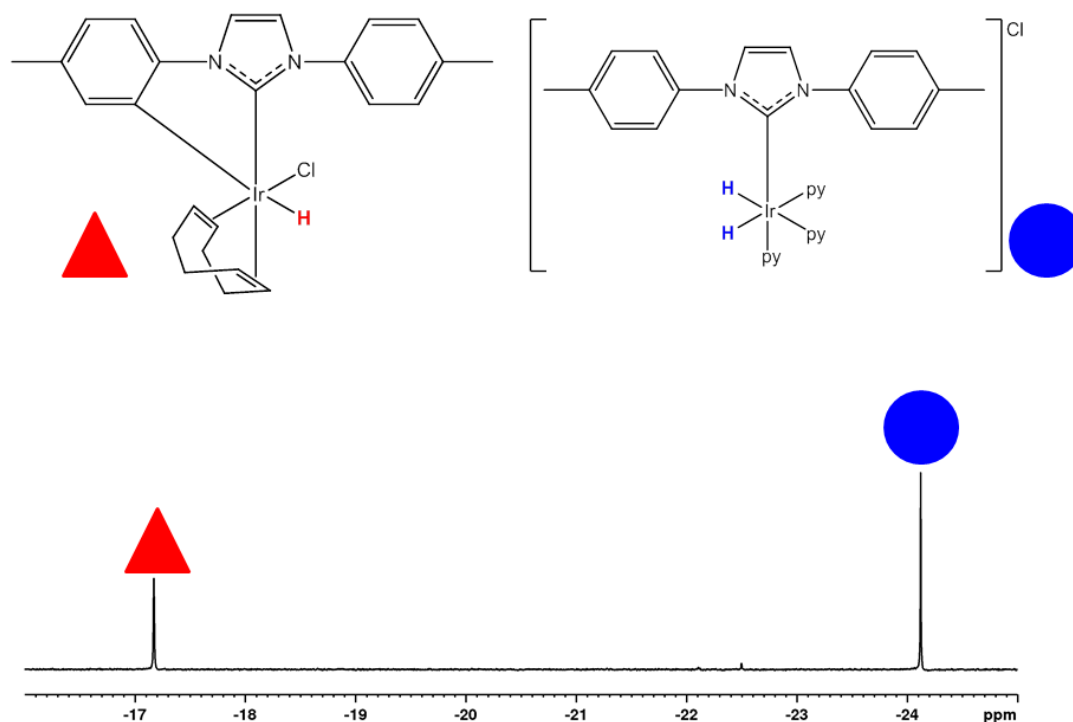
Figure 37: ^{1}H HMR spectrum of the hydride region corresponding to the SABRE active complex, [Ir(H)$_2$(COD)(ITol)(py)$_3$]Cl and the CH activated complex IrCl(H)(COD)(IXy) at 298 K in CD$_2$Cl$_2$.

3.2.3.2   *Reaction of IrCl(COD)(ITol) (3) with py and p-H$_2$ and the formation of [Ir(H)$_2$(ITol)(py)$_3$]Cl (4)*

When *para*hydrogen is added to a solution containing IrCl(COD)(NHC) with 5 equivalents of substrate in CD$_2$Cl$_2$, once the NMR tube has been shaken in an approximate 65 G magnetic field, we would usually expect to see hyperpolarised signals for both the free and the bound substrate as polarisation is transferred from the *para*hydrogen derived hydrides to the substrate. The bound substrate then continuously exchanges with the free substrate in solution until *para*hydrogen is used up. When IrCl(COD)(ITol) with 5 equivalents of pyridine in CD$_2$Cl$_2$ is activated with *para*hydrogen, we would expect to observe the formation of the traditional tris SABRE active complex, [Ir(H)$_2$(L)(sub)$_3$]Cl, with

a corresponding equivalent hydride signal at around δ -22. We do observe the formation of this complex in the solution, with a corresponding hydride resonance at -24.11 as seen in Figure 38.
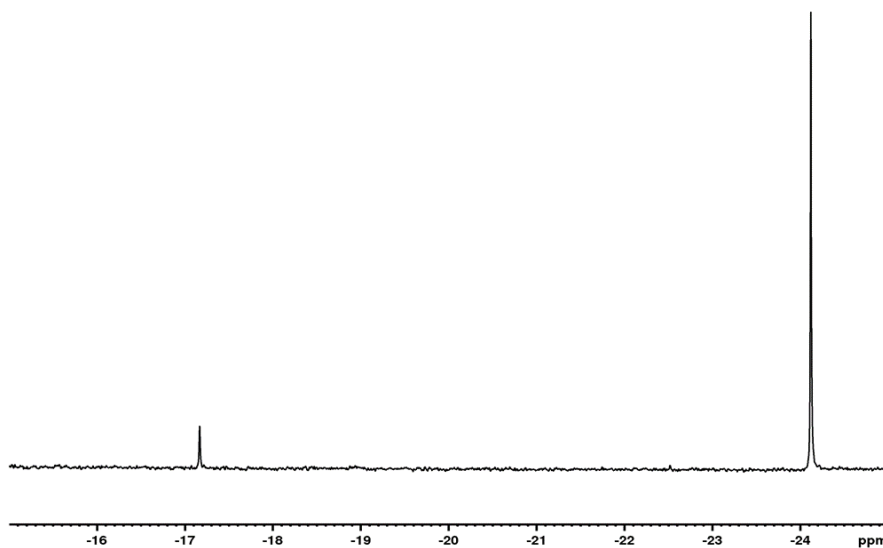
Figure 38: ^{1}H NMR spectrum of the hydride region, once *para*-H$_2$ has been added to a solution containing, IrCl(ITol)(COD) with 5 equivalents of pyridine in CD$_2$Cl$_2$ and shaken in an approximate 65 G magnetic field for 10 seconds.

However, once a 1 scan ^{1}H hyperpolarised NMR spectrum is taken, we only observe a very small amount of polarisation in the *ortho*, *para* and *meta* protons of the free pyridine in solution, this is illustrated in Figure 39, with a total 11-fold signal enhancement. This is considered to be very low, for a SABRE-active complex.
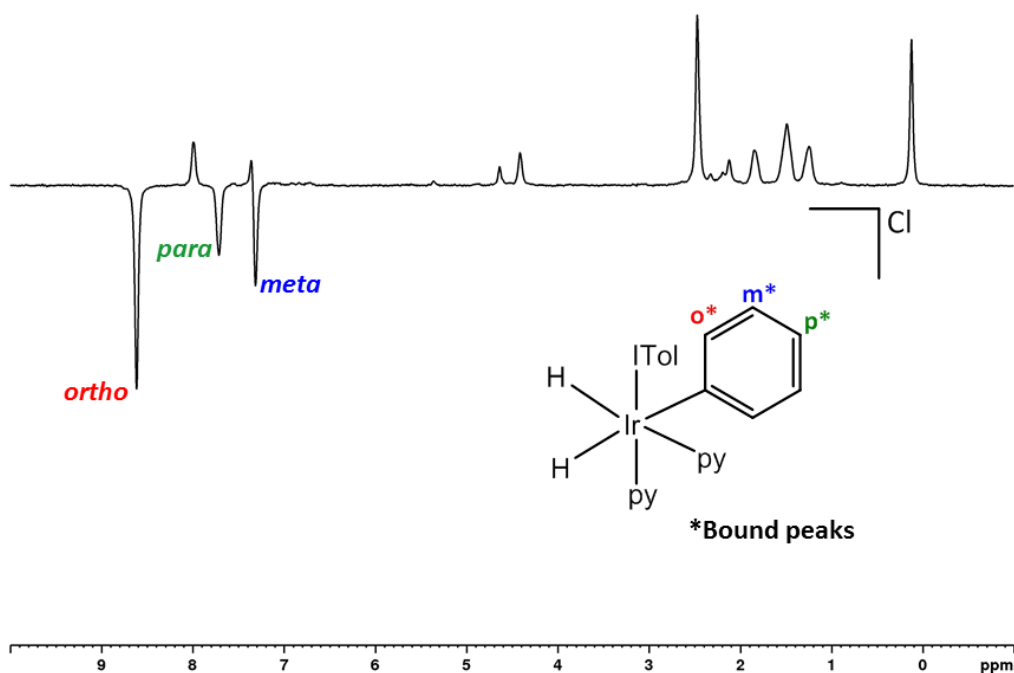
Figure 39: A 1 scan hyperpolarised ^{1}H NMR spectrum, showing the free pyridine resonances in solution are polarised as we observe antiphase signals. However, we are unable to detect the polarisation of the bound peaks for the SABRE active complex.

3.2.4 Reaction of 3 with py in H₂ in CD₃OD at 233 K

3.2.4.1 Initial H₂ addition of 3 and hydride migration in IrCl(H)₂(ITol)(COD)

As previously explained, When a solution containing IrCl(COD)(IXy) and pyridine in CD$_3$OD is activated with hydrogen, we typically see this is the formation of intermediates where pyridine binds to the metal centre forming **1b** or **1c**. However in this instance, when hydrogen is added to a solution containing **3** with 5 equivalents of pyridine in CD$_3$OD, we are unable to observe the formation of IrCl(H)$_2$(ITol)(COD) or [Ir(H)$_2$(ITol)(COD)(py)]Cl as pyridine does not bind and COD does not hydrogenate and fall off. Therefore, the 18-electron SABRE-active complex [Ir(H)$_2$(ITol)(py)$_3$]Cl does not form. This is due to the slow rotation that may be preventing the observation of the spectral lines in the NMR spectrum.

3.2.4.2 Reaction of IrCl(COD)(ITol) (3) with py and p-H₂ and the formation of [Ir(H)₂(ITol)(py)₃]Cl

A sample containing **3** with 5 equivalents of py in CD$_3$OD was shaken at an approximate 65 G magnetic field with 3 bar pressure of *para*-H$_2$. As discussed previously in section 3.1.5.1, where a similar compound known as IrCl(COD)(IXy) was analysed, we were also unable to observe the SABRE-tris complex **4** forming. However, as the reaction takes place at 233 K, we do not see the *tris* complex forming as the temperature is too cold for the

COD to hydrogenate. We continue to observe the free *ortho*, *meta* and *para* pyridine resonances at δ 8.58, 7.94 and 7.42, but SABRE is not able to take place as 233 K in CD$_3$OD.

3.2.5 Reaction of 3 with py and H$_2$ in CD$_3$OD at 298 K

3.2.5.1 Initial H$_2$ addition to IrCl(COD)(ITol)(3) and hydride migration in IrCl(H)$_2$(COD)(ITol)

When a solution containing IrCl(COD)(ITol) and pyridine in CD$_3$OD is activated by hydrogen, we expect to see the formation of complex IrCl(H)$_2$(COD)(ITol)(py) where pyridine displaces Cl and binds to the central metal. However, when hydrogen is added to a solution containing **3** with 5 equivalents of pyridine in CD$_3$OD at 298 K, as observed with this solution at 233 K, we are unable to observe the formation of the SABRE-active complex [Ir(H)$_2$(ITol)(py)$_3$]Cl. We are also unable to observe the formation of the intermediates, IrCl(H)$_2$(ITol)(COD) or [Ir(H)$_2$(ITol)(COD)(py)]Cl as pyridine does not bind and COD remains bound to the metal centre. This reaction was attempted at both 233 K and 298 K both result in the same problem, which as previously stated is due to COD not hydrogenating. We do observe the free *ortho*, *meta* and *para* pyridine resonances, which remain relatively the same as the solution at 233 K, at δ 8.56, 7.88 and 7.45. once *para*-H$_2$ is added what we expect to observe is the hyperpolarisation in both the bound and free pyridine of the SABRE active complex, [Ir(H)$_2$(COD)(ITol)(py)$_3$]Cl.

3.2.5.2 Reaction of IrCl(COD)(ITol) (3) with py and p-H$_2$ and the formation of [Ir(H)$_2$(ITol)(py)$_3$]Cl

When 5 equivalents of pyridine is dissolved in a solution of CD$_3$OD with **3**, there is no evidence at 298 K, that pyridine binds by replacing Cl and forms the complex [Ir(COD)(ITol)(py)]Cl. However, a CH activated complex (seen previously in Figure 36) where the carbon on the tolyl has bound to the central metal iridium atom is observed.
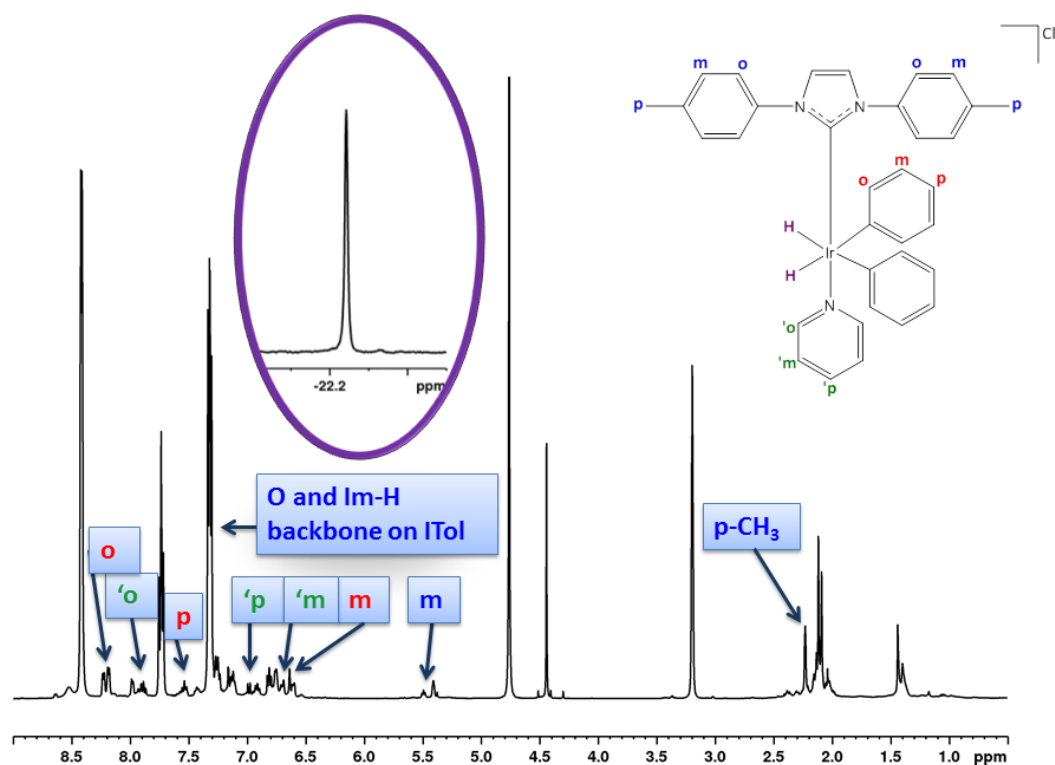
Figure 40: ^{1}H NMR spectrum where 32 scans were taken to identify the formation of [Ir(H)$_2$(ITol)(py)$_3$]Cl, once parahydrogen was added at 3 bar pressure and the shake and drop method was applied for 10 seconds causing a reaction to occur.

The free pyridine peaks are identified at δ 8.41, 7.73 and 7.32, indicating that pyridine is free in solution. Upon the addition of hydrogen to the solution in CD$_3$OD, it was not possible to see the usual complex [Ir(H)$_2$(NHC)(COD)(py)]Cl or any other intermediates in the solution at 298 K.

Once *p*-H$_2$ was added to the solution, the sample was shaken at 65 G for 10 seconds. We were able to observe the formation of the SABRE-active tris complex [Ir(H)$_2$(ITol)(py)$_3$]Cl with the corresponding ^{1}H NMR spectrum seen in Figure 40, which contains a corresponding hydride signal at δ −22.24. In Figure 40, we can also observe resonances for the *equatorial* (bound *trans* to the hydride) pyridine peaks at δ 8.30 for the *ortho* bound pyridine protons at δ 7.47 for the *para* bound pyridine protons at δ 6.48 and for the *meta* bound pyridine protons. For the axial (bound *trans* to the NHC) bound pyridine peaks, we observe chemical shifts at δ 7.80, 7.00 and 6.69. The peaks remaining are for the ITol NHC, where the corresponding proton peaks are observed for the *ortho* protons at δ 7.35 which also overlaps with the Imidazolium backbone. The *meta* protons are observed at δ 5.57 and for the *para* CH$_3$ peak at δ 2.34. The peaks not annotated are for the solvent peak at δ 5.0, the hydrogen peak at δ 4.5 and COE (cyclooctene) which yield corresponding resonances at observed at δ 1.50, 2.10 and 5.60.

The maximum signal enhancement in CD_3OD on the *ortho* protons of the pyridine was 0.5-fold (shaken at 65G with a 5 equivalents of pyridine) which after 15 minutes no longer polarises. This could be due to the aromatic substituents not being bulky enough so the complex loses its stability.

3.3   IrCl(COD)(^{t}BuBIM) (5)

In this section, we will discuss how another symmetric complex was synthesised and used to examine whether the SABRE-active form of this complex would undergo SABRE. We were also interested in understanding if this complex, which has less bulkier nitrogen substituents could work better than the most efficient SABRE catalysts, IMes. We examined this complex with pyridine and hypothesise that a SABRE active complex forms but due to the less bulky substituents on the NHC, that the SABRE efficiency may not be as great as IXy or IMes catalyst due to both NHCs being more strongly electron-donating species.

3.3.1   Synthesis of IrCl(COD)(^{t}BuBIM) (5)
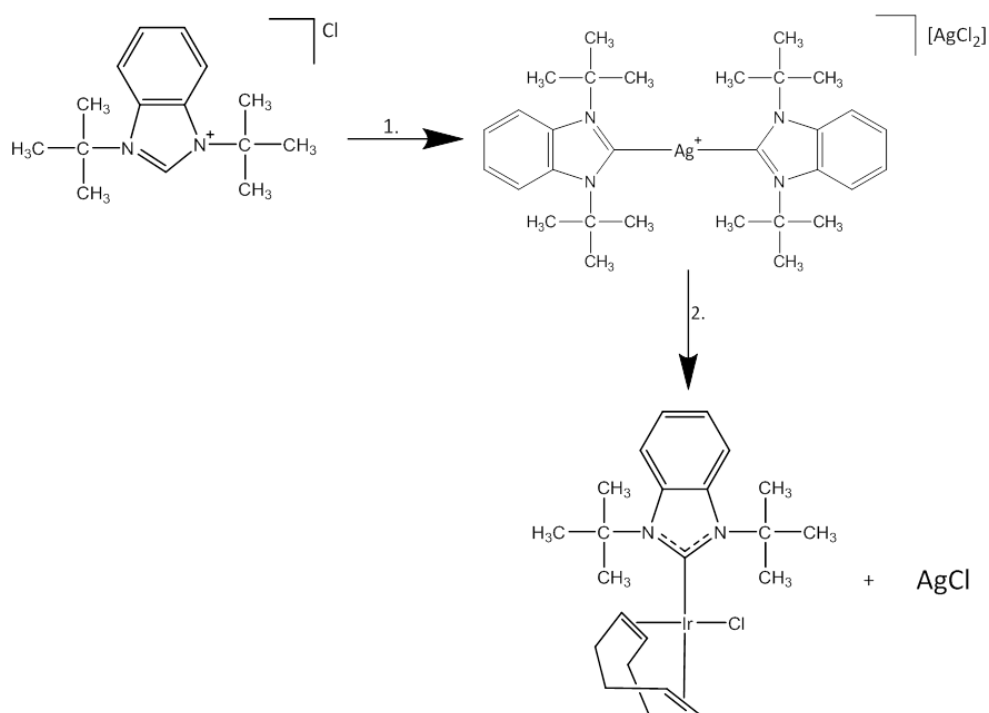
Figure 41: Schematic steps to show the synthesis of IrCl(COD)(^{t}BuBIM) with ^{t}BuBIM = 1,3-Di-tert-butylimidazolium chloride (adapted from Gülcemal et al 2013.[80]) . Step 1: Stirring with Ag_2O under N_2 gas shielded from light in dry DCM for at rt for 24h. 2. Stirred with [Ir(COD)Cl]$_2$ at rt in dry DCM for 24h.

Complex **5** was synthesised under a nitrogen atmosphere and a mixture of 1,3-Di-tert-butylbenzimidazolium chloride (52.5 mg, 0.20 mmol) and Ag_2O (38.0 mg, 0.16 mmol) was suspended in dry CH_2Cl_2 (10 mL) and stirred at room temperature for 24h shielded from light, seen in Figure 41. $[Ir(COD)Cl]_2$ (110.1 mg, 0.16 mmol) was added to the suspension with another 10 mL of dry CH_2Cl_2 and the reaction mixture was stirred at room temperature for 24h. The resulting suspension was filtered over Hyflo® Super Cel®. CH_2Cl_2 was evaporated leaving a dark red solid. Under a nitrogen atmosphere the solid was washed with Et_2O (3mL) and removed firstly by pasture pipette then the rest evaporated. The remaining solid appeared a dark red colour.

3.3.2 SABRE of IrCl(COD)(^{t}BuBIM) (5)

Once complex **5** was successfully synthesised, it was dissolved in CD_3OD with a 5-fold excess of pyridine. The complex [Ir(COD))(tBuBIM)(py)]Cl was not seen on the ^{1}H NMR spectrum so there is no evidence that Cl is rapidly replaced by a pyridine molecule in the solution, as had been seen before in the case of IrCl(COD)(IMes) complex. 3 bars of p-H_2 were added to the solution and it was shaken at an approximately 65 G magnetic field. The COD molecule had not fallen off after hydrogenating into COE and no enhancement could be seen. To speed up the initial reaction, the complex was warmed up to about 40˚C but unfortunately, the catalyst started to decompose with the solution changing colour to a dark red so it was determined that it would not be suitable for SABRE.

To truly assess this issue, It is recommended that the complex be tested with a different substrate or a different solvent and also adding a co-ligand, which has also been proven to provide greater polarisation enhancements with certain SABRE-active complexes.[81] Once complex 5 was successfully synthesised, the complex was dissolved in CD_3OD with a 5-fold excess of pyridine. The complex [Ir(py)(tBuBIM)(COD)]Cl was not seen on the ^{1}H NMR spectrum so there was no evidence that Cl is rapidly replaced by a pyridine molecule in the solution, as it was seen before in the case of IrCl(IMes)(COD) complex. 3 bars of p-H_2 were added to the complex and it was shaken at an approximately 65 G magnetic field. The COD molecule had not fallen off after hydrogenising into COE and no enhancement could be seen. To speed up the initial reaction, the complex was warmed up to about 40˚C but unfortunately, the catalyst started to decompose so it was determined that it would not be suitable for SABRE.

3.4 IrCl(IMes)(COD) (6)

At the beginning of section 3.1, we examine symmetric NHC complexes with pyridine in both CD_2Cl_2 and CD_3OD and successfully identify their SABRE efficiencies and intermediates that form during the different reactions. In this section we investigated a related complex that form with 3,5-lutidine. This complex acts as a control to identify if either symmetric or asymmetric SABRE-active complexes have better efficiencies. IrCl(COD)(IMes) is currently the complex which holds the highest enhancements with pyridine making it the most efficient and effective SABRE complex known for SABRE.[1] In this section, we will discuss how IrCl(COD)(IMes) went through a series of reactions and hypothesise that it will form a SABRE active catalyst and have the highest signal enhancement, therefore remaining the most efficient SABRE catalysts.

3.4.1 Reaction of 6 with 3,5-Lutidine in CD_3OD

IrCl(COD)(IMes) was dissolved in a solution containing CD_3OD with 5 equivalents of 3,5-lutidine. When IrCl(COD)(IMes) with 4 equivalents of pyridine in CD_3OD, the formation of the complex [Ir(COD)(IMes)(py)]Cl which is proven by the bound pyridine region of the corresponding ^1H NMR spectrum.[1] However when 5 equivalents of 3,5-lutidine is added to a solution containing IrCl(COD)(IMes) in CD_3OD, we are unable to observe the formation of [Ir(COD)(IMes)(3,5-lutidine)]Cl at 298 K. This temperature causes the NMR lines to broaden, distorting the NMR spectrum.

3.4.2 Initial H_2 addition to IrCl(COD)(IMes) and hydride migration in [Ir(H)$_2$(COD)(IMes)]Cl at 298 K
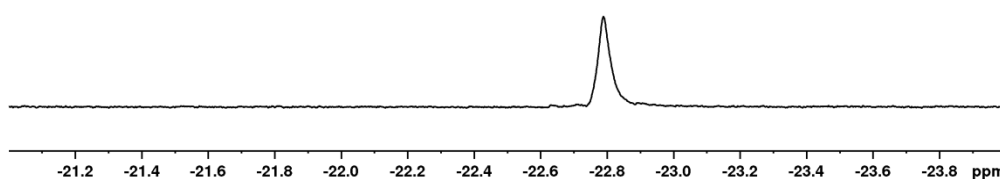
Figure 42: A ^1H NMR spectrum of the hydride region corresponding to the CH activated product of ITol, [Ir(H)$_2$(IMes)(3,5-lutidine)$_3$]Cl.

When hydrogen is added to a solution containing IrCl(COD)(IMes) with 5 equivalents of substrate in CD_2Cl_2, once the NMR tube has been shaken outside of the spectrometer, we would usually expect to see the formation of the complex, [Ir(H)$_2$(COD)(IMes)]Cl, where the hydrogen hydrides would bind to the metal centre. However, we do not observe this formation but instead see the SABRE-active *tris* complex, [Ir(H)$_2$(IMes)(3,5-lutidine)$_3$]Cl, forming with a corresponding hydride signal at δ −22.80, seen in Figure 42.

3.4.3 Reaction of IrCl(COD)(IMes) with py and p-H₂ at 298 K and the formation of [Ir(H)₂(IMes)(3,5-Lutidine)₃]Cl (7)

In CD_3OD, Complex **6** was dissolved with 5 equivalents of 3,5-lutidine and the formation of [Ir(COD)(ITol)(py)]Cl was not observed due to the fast rotation of the nitrogen substituents on the NHC causing the NMR lines to broaden. Upon the addition of hydrogen to the solution in CD_3OD, it was not possible to see usual complex [Ir(H)₂(IMes)(COD)(3,5-lutidine)]Cl or [Ir(H)₂(COD)(IMes)]Cl in the solution at 298 K.

P-H₂ was added to the solution and the sample was shaken at 65 G for 10 seconds. We were able to observe the formation of the SABRE-active *tris* complex [Ir(H)₂(IMes)(3,5-lutidine)₃]Cl with the corresponding ¹H NMR spectrum seen in Figure 43. The hydrides yield a corresponding signal at δ −22.80. We can observe resonance for the *equatorial* (bound *trans* to the hydride) pyridine peaks at δ 7.99 for the *ortho* bound 3,5-lutidine protons, at δ 7.44 for the *para* bound 3,5-lutidine protons and at δ 2.01 for the *meta* bound 3,5-lutidine protons. For the axial (bound *trans* to the NHC) bound 3,5-lutidine peaks, we observe chemical shifts at δ 7.67, 7.33 and 2.19. The corresponding proton resonances are observed for the imidazolium backbone protons at δ 7.30 and the *meta* protons are observed at δ 6.73. The *para* CH₃ peak at δ 2.23 and the *ortho* CH₃ proton resonance observed at δ 2.10. The peaks not annotated are for the free *ortho*, *para* and *meta* 3,5-lutidine observed at δ 8.20, 7.55 and 2.35. The solvent peak is observed at δ 5.0, the hydrogen peak at δ 4.5 and COA (cyclooctane) which yield corresponding resonances at observed at δ 1.5.
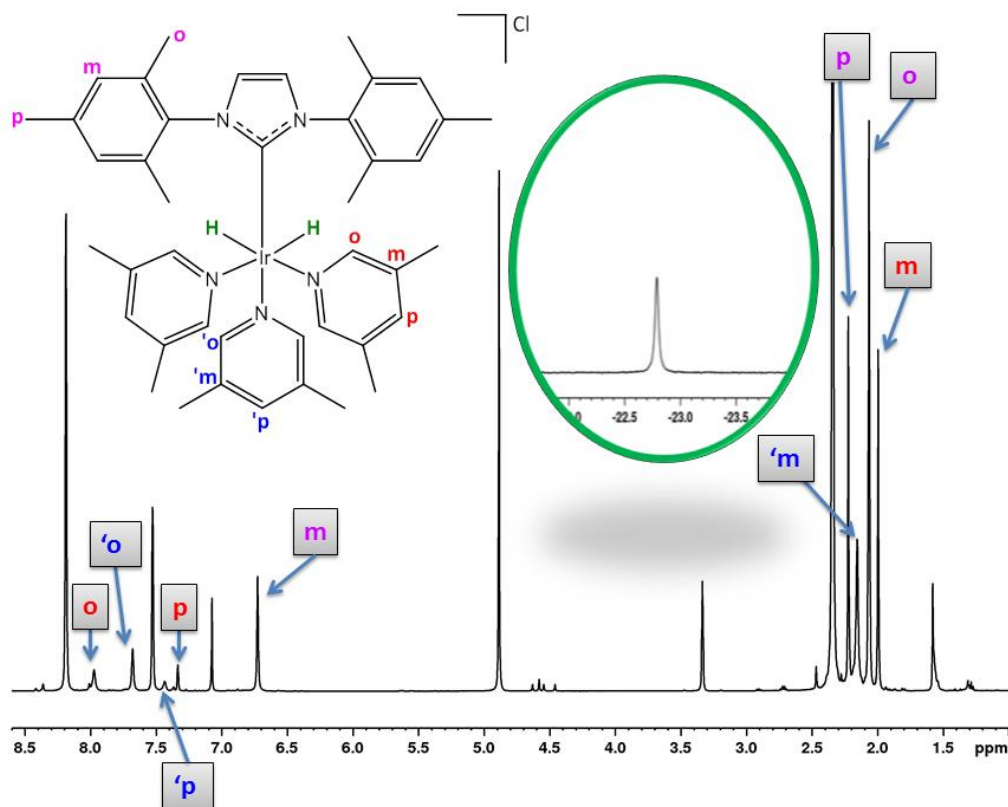
Figure 43: A 32 scan ^{1}H NMR spectrum identify the formation of [Ir(H)$_2$(IMes)(3,5-lutidine)$_3$]Cl, once parahydrogen was added at 3 bar pressure and shaken at 65 G magnetic field for 10 seconds causing a reaction to occur.

Figure 44 illustrates a 1 scan ^{1}H NMR spectrum when complex **6** is shaken at 65 G with a 5 equivalents of 3,5-lutidine. We are able to observe the free and bound 3,5-lutidine resonances polarisation to antiphase NMR resonances. The free 3,5-lutidine are for the free *ortho*, *para* and *meta* 3,5-lutidine are observed at δ 8.20, 7.55 and 2.35. The maximum total signal enhancement in this solution in the free 3,5-lutidine resonances was 346-fold.
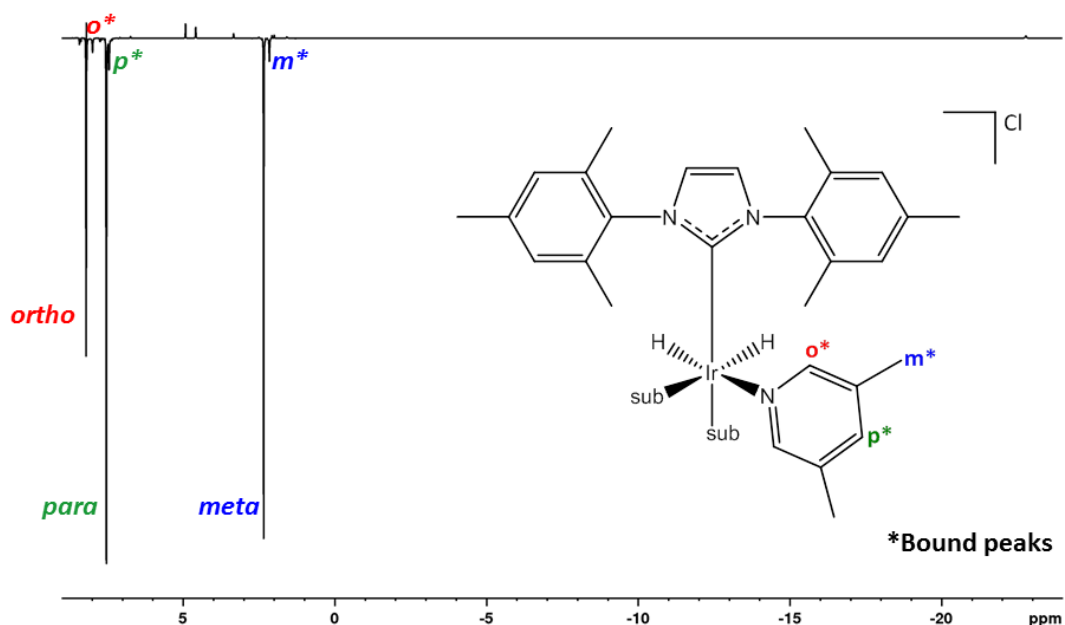
Figure 44: A 1 scan hyperpolarised ^{1}H NMR spectrum, showing the free and bound equatorial 3,5-lutidine resonances in solution are polarised and observe antiphase signals. This indicated that the SABRE-active complex [Ir(H)$_2$(IMes)(3,5-Lutidine)$_3$]Cl forms with the corresponding resonances for the bound equatorial 3,5-lutidine seen at δ 7.99, 7.44 and 2.23.

3.5 Summary and Discussion

In this chapter, SABRE-active complexes were formed for both IrCl(COD)(IXy) and IrCl(COD)(ITol) and polarisation was achieved for both with pyridine as the substrate.

To form the SABRE-active catalyst [Ir(H)$_2$(IXy)(py)$_3$]Cl, IrCl(COD)(IXy) went through a series of reactions and displacements. In CD$_3$OD, the chloride was displaced by the substrate, pyridine, and formed [Ir(COD)(IXy)(py)]Cl, as seen in Figure 27. Under hydrogen, further reaction leads to an intermediate by oxidative addition where the hydrogen binds *trans* to the COD and *trans* to pyridine. The result is [Ir(H)$_2$(COD)(IXy)(py)]Cl, as seen in Figure 31. When this reaction was performed in CD$_2$Cl$_2$, these intermediates were seen at 233 K and 298 K, as shown in Figure 28 and Figure 29. The final reaction occurs when COD undergoes hydrogenation and forms SABRE active catalyst, [Ir(H)$_2$(IXy)(py)$_3$]Cl, of Figure 33. The formation of the SABRE-active catalyst, [Ir(H)$_2$(IXy)(py)$_3$]Cl, is more rapid in methanol where its charge is better solvated and this results in the fact that the [Ir(H)$_2$(COD)(IXy)(py)]Cl is only seen at 233 K.

IrCl(COD)(ITol) forms the SABRE-active catalysts, [Ir(H)$_2$(ITol)(py)$_3$]Cl very inefficiently as seen in Figure 40. This is because of CH-activation of the ITol ring leads to decomposition, hence we might predict the ITol system is less suitable for SABRE. This is reflected in practice as [Ir(H)$_2$(IXy)(py)$_3$]Cl produces a higher polarisation enhancement at 102-fold

when compared [Ir(H)$_2$(ITol)(py)$_3$]Cl at 0.5-fold. This is difference in behaviour is due to the bulkier nitrogen substituents on the [Ir(H)$_2$(IXy)(py)$_3$]Cl where the extra CH$_3$ group provides more steric stability which allows the pyridine to dissociate more readily.[1] It has been reported previously by Lloyd et al[1] that providing the NHC ligand is sufficiently electron-rich, good catalyst stability ensues. As ligand loss is dissociative, it was hypothesised that we might use the steric bulk of the NHC to develop a more efficient SABRE catalyst and that it controls both the electronic and steric parameters of the NHC, thereby the bulkiness of the NHC has an effect on the polarisation transfer process.[1] The results described in this chapter support this hypothesis.

We also determined that reacting **1** and **3** in different solvents produces different intermediates so choosing the right SABRE solvent is important and can affect the efficiencies of the SABRE-active catalysts.

The SABRE-active complex of IMes, [Ir(H)$_2$(IMes)(py)$_3$]Cl, currently is the most efficient SABRE-active catalyst providing the greatest polarisation enhancements with a total signal enhancement with 4 equivalents of pyridine at 5500-fold. Therefore, IMes was used as a control with 3,5-lutidine as the substrate. We observe that when IrCl(COD)(IMes) reacts with 5 equivalents of 3,5-lutidine in CD$_3$OD and *para*-H$_2$, and the SABRE-active catalyst [Ir(H)$_2$(IMes)(3,5-lutidine)$_3$]Cl forms providing large polarisation enhancements of over 300-fold. This tells us that the substrate 3,5-lutidine acts as a good substrate for this catalyst even though the substrate is bulky. It is however less well polarised that pyridine in accordance with the faster dissociation rate.

4 SABRE with asymmetric *N*-Heterocyclic carbene complexes

4.1 IrCl(COD)(PhCarCH₃) (8)

Previously in section 3, we observed the reaction of iridium bound symmetric NHC complexes with pyridine and examined these using NMR to determine their intermediates but to also investigate whether they were appropriate and efficient SABRE catalysts. In this section we will investigate reactivity with 3,5-Lutidine. Complexes IrCl(COD)(MesCarBenzyl) and IrCl(COD)(MesCarHomoBenzyl) were synthesised in the Duckett group whereas the IrCl(COD)(PhCarCH₃) and IrCl(COD)(MesCarCH₃) complexes were purchased. The synthesis and characterisation of the NHC, IrCl(COD)(MesCarBenzyl) and IrCl(COD)(MesCarHomoBenzyl) were previously explained in section 2.4. In this section, we will discuss how the 4 asymmetric complexes went through a series of reactions and hypothesise that for each a SABRE active complex will form but however, due to the rate constants and thermodynamic parameters stated in section 2.7.1 where the SABRE active complex, [Ir(H)₂(MesCarHomoBenzyl)(3,5-lutidine)₃]Cl, has the highest $\Delta G^{\neq}$ at 133 kJ and the fastest exchange rates at 1.190 s⁻¹ at 298 K, 3.700 s⁻¹ at 303 K and 10.80 s⁻¹ at 313 K which we hypothesise will also have the greatest SABRE enhancements.

4.1.1 Reaction of 8 with 3,5-lutidine in CD₃OD

1.3 mg of IrCl(COD)(PhCarCH₃) was dissolved in a solution with 5 equivalents of 3,5-lutidine in CD₃OD. We expect to see the formation of the complex [Ir(COD)(PhCarCH₃)(3,5-Lut)]Cl where lutidine displaces the chloride and binds to the iridium metal centre.[1] However, this reaction is not observed so we are able to identify the free 3,5-lutidine in solution with the corresponding *ortho*, *para* and *meta*-CH₃ resonances at δ 8.06, 7.40 and 2.21. We are also able to assign all the corresponding peaks for the IrCl(COD)(PhCarCH₃) which is fully characterised in section 6.4.

4.1.2 Initial H₂ addition to IrCl(COD)(PhCarCH₃) and hydride migration in IrCl(H)₂(COD)(PhCarCH₃) at 298 K

Hydrogen was added to IrCl(COD)(PhCarCH₃) with 5 equivalents of 3,5-Lutidine in CD₃OD and shaken outside of the NMR spectrometer. The colour instantly changes from yellow to colourless indicating that a reaction has occurred. When a ¹H NMR spectrum is taken, we can see that the SABRE active complex [Ir(H)₂(PhCarCH₃)(3,5-lutidine)₃]Cl has formed. The corresponding ¹H NMR spectrum shows a hydride signal at δ −22.37. We expect this reaction to occur quickly due to the temperature being 298 K, so the 3,5-lutidine is able to

displace the chloride and cause the COD to hydrogenate. The hydride region of the resulting ^{1}H NMR spectrum is shown in Figure 45. It contains one pair of hydride resonances which are both chemically equivalent to each other and indicates the formation of one product which is the SABRE active complex, $[Ir(H)_2(PhCarCH_3)(3,5-lutidine)_3]Cl$.
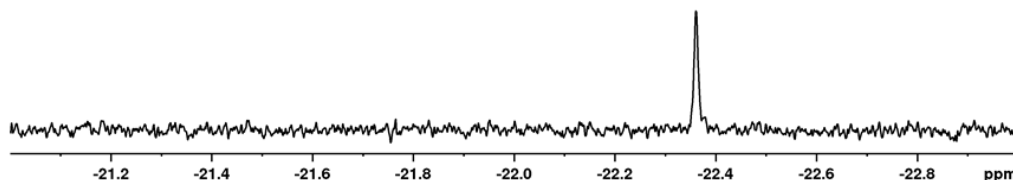
Figure 45: ^{1}H NMR spectrum showing the hydride region of the complex with one single diagnostic hydride resonance at δ −22.37 indicating the formation of the SABRE active *tris* complex.

4.1.3 Reaction of IrCl(COD)(PhCarCH$_3$) with py and p-H$_2$ at 298K and the formation of [Ir(H)$_2$(PhCarCH$_3$)(3,5-Lutidine)$_3$]Cl (9)

Once *p*-H$_2$ was added to the solution, the sample was shaken for 10 seconds at an approximate 65 G magnetic field. We observe antiphase, hyperpolarised bound substrate signals of the SABRE active *tris* complex, $Ir(H)_2(PhCarCH_3)(3,5-Lutidine)_3]Cl$ as seen in Figure 46. The corresponding proton signal in the substrate region for the bound equatorial *ortho*, *para* and *meta*-CH$_3$ protons are at δ 8.03, 7.54 and 2.29 with the free 3,5-lutidine resonances for the *ortho*, *para* and *meta*-CH$_3$ protons are found at δ 8.10, 7.30 and 2.20.
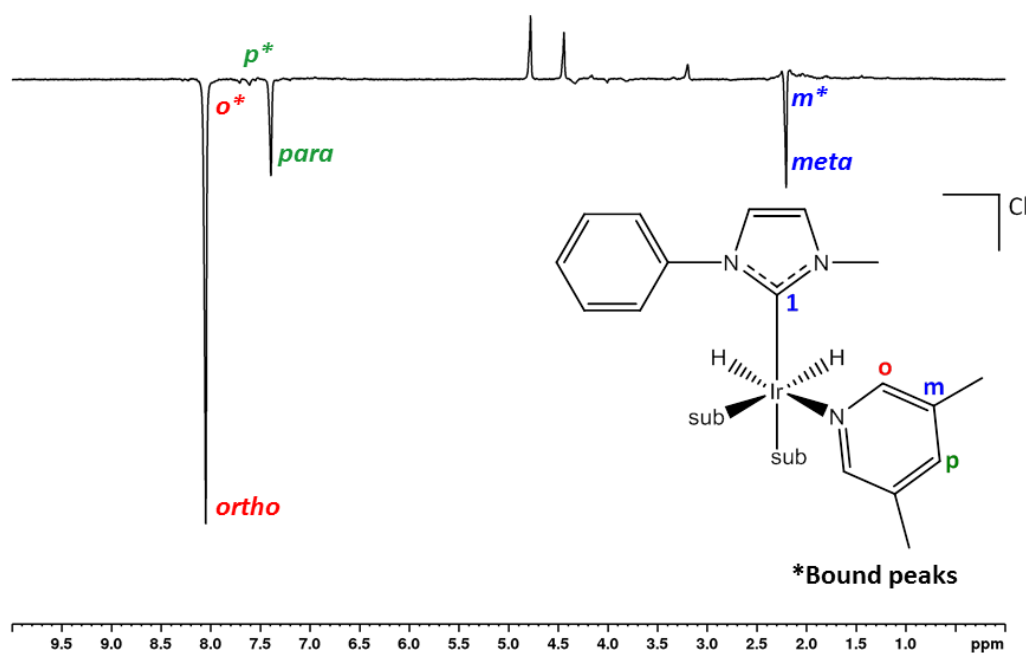
Figure 46: Hyperpolarised 1 scan ^{1}H NMR spectrum showing the free 3,5-lutidine peaks polarising the *ortho*, *meta* and *para* protons but also the bound equatorial 3,5-lutidine protons in the *ortho*, *meta* and *para* positions indicating the formation of the SABRE active tris complex [Ir(H)$_2$(PhCarCH$_3$)(3,5-Lutidine)$_3$]Cl.

We are also able to identify the bound axial 3,5-lutidine resonances at δ 7.64 for the *ortho* protons, δ 7.16 for the *para* protons and δ 2.20 for the *meta* CH$_3$ protons. In Figure 46, the remaining peaks are for the imidazolium backbone protons at δ 7.11, the *ortho* and *meta* protons of the phenyl ring identified at δ 6.83, the *para* proton on the phenyl ring found at δ 7.10 and the CH$_3$ bound to the nitrogen on the carbene at δ 2.22.

The maximum signal enhancement on the *ortho* protons of the lutidine was 8-fold when the sample was shaken at 65 G with 5 equivalents of 3,5-lutidine. The *para* protons had a maximum signal enhancement of 3-fold and the *meta* CH$_3$ protons had a maximum signal enhancement of just 1-fold, seen in Figure 46.

4.2 [IrCl(COD)(MesCarCH$_3$)] (10)

In section 4, we discussed that four asymmetric NHC complexes were examined with 3,5-lutidine as the substrate. In this section, we will be investigating another asymmetric NHC complex with 3,5-lutidine which has a similar structure to [IrCl(COD)(PhCarCH$_3$)] but on the phenyl ring has CH$_3$ groups on the *ortho* and *para* positions. The complex will be examined with SABRE through a series of reactions to determine its intermediates but to also investigate whether it is an efficient SABRE catalyst. I hypothesise that this SABRE active catalyst, [Ir(H)$_2$(MesCarCH$_3$)(3,5-Lutidine)$_3$]Cl, will form and be more efficient in

SABRE than $[Ir(H)_2(PhCarCH_3)(3,5-Lutidine)_3]Cl$ due to the extra CH_3 groups providing more electron-donation and therefore, more stability to the structure.

4.2.1 Reaction of 10 with 3,5-Lutidine in CD₃OD

CD_3OD was the solvent chosen due to its polar characteristics and $[IrCl(COD)(MesCarCH_3)]$ with 5 equivalents of 3,5-lutidine was dissolved in 600 µL of CD_3OD. When a similar solution of $[IrCl(COD)(IMes)]$ and pyridine were dissolved the CD_3OD, we observe the formation of $[Ir(COD)(IMes)(py)]$ where one pyridine molecule binds to the iridium metal centre displacing chloride. For this reaction, we observe one 3,5-lutidine molecule binding to the metal centre and displacing chloride forming $[Ir(COD)(MesCarCH_3)(3,5-lut)]Cl$ (**10a**). The corresponding ^{1}H NMR spectrum is shown in Figure 47, where we are able to observe the following:

The corresponding resonances for the coordinated 3,5-Lutidine are observed at δ 7.99, 7.50 and 2.20 for the *ortho*, *meta* and *para*-CH_3 proton. The remaining unlabelled peaks correspond to the COD CH and CH_2 protons which yield corresponding resonances at δ 4.41, 3.82 and 1.40-1.30. The imidazolium backbone of the $MesCarCH_3$ NHC appears at δ 7.20 and 6.88 with *meta* protons on the $MesCarCH_3$ aromatic appear at δ 6.79. Finally, the CH_3 protons on the NHC appear at δ 3.15 for the *para* protons of the mesityl ring, δ 2.50 and 2.43 for the *ortho* protons on the mesityl ring, and at δ 1.68 for the CH_3 protons bound to the nitrogen on the imidazolium NHC centre.

The other unaccounted for peaks refer to the solvent residual at δ 4.9 and also the free pyridine peak for the *ortho*, *para* and *meta* protons of the 3,5-lutidine seen in the aromatic region at δ 8.20, 7.50 and 2.40.
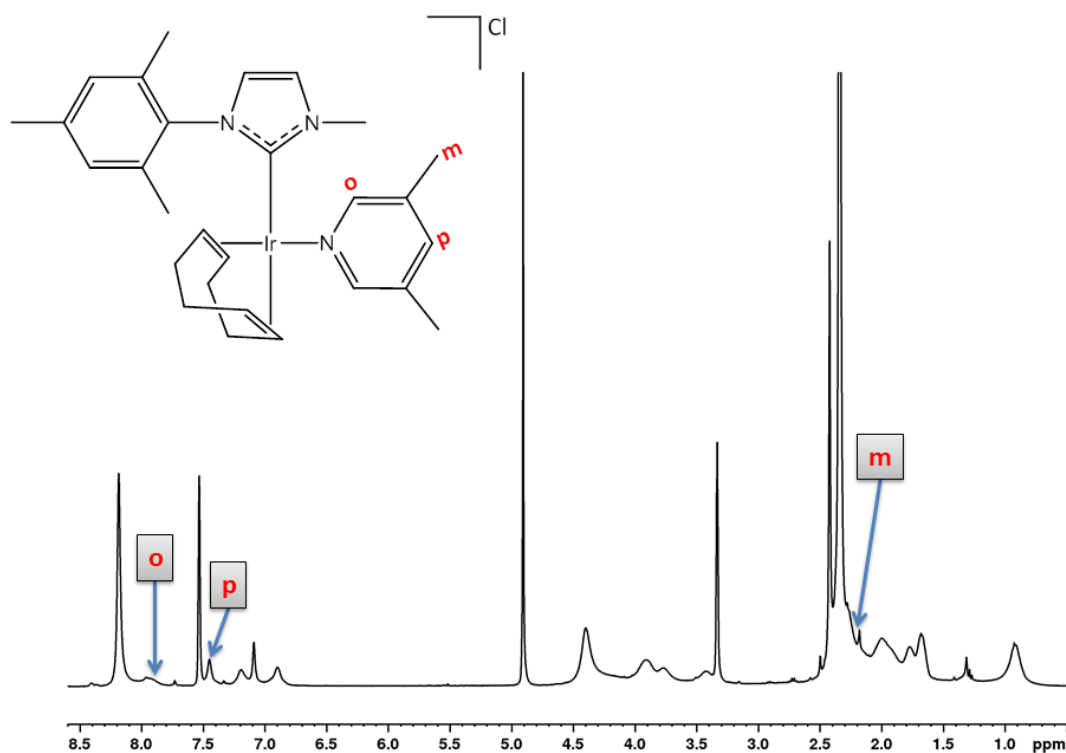
Figure 47: A 32 scan ^{1}H spectrum of IrCl(COD)(MesCarCH$_3$) with 5 equivalents of 3,5-lutidine in 600µL of CD$_3$OD at 400 MHz at a temperature of 298 K forming [Ir(COD)(MesCarCH$_3$)(3,5-lutidine)]Cl. This spectrum shows the bound *ortho*, *meta* and *para* protons of the 3,5-lutdidine at δ 7.99, 7.50 and 2.20.

4.2.1 Initial H$_2$ addition to IrCl(COD)(MesCarCH$_3$) and hydride migration in IrCl(H)$_2$(COD)(MesCarCH$_3$)

Hydrogen was added to [Ir(COD)(MesCarCH$_3$)(3,5-lut)]Cl to form the SABRE precursor, [Ir(H)$_2$(COD)(MesCarCH$_3$)(3,5-lut)]Cl in CD$_3$OD, where now that once 3,5-lutidine has bound to NHC complex, there is a 4-fold excess of 3,5-Lutidine. The sample is then shaken for about 10 seconds outside the spectrometer and a ^{1}H NMR spectrum was immediately taken to monitor the reaction expected to take place. However, we see the immediate formation of the SABRE active *tris* complex, [Ir(H)$_2$(COD)(MesCarCH$_3$)$_3$]Cl, with resulting equivalent hydride resonances at δ – 22.35 which is illustrated in Figure 48.
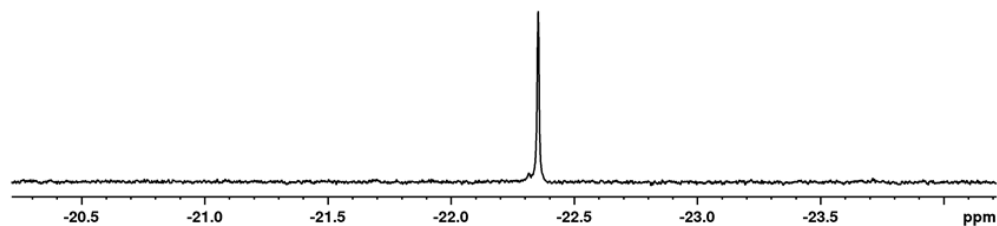
Figure 48: ^{1}H NMR spectrum of the hydride region of [IrCl(COD)(MesCarCH$_3$) with 5 equiv of 3,5-Lutidine with hydrogen gas activation forming the SABRE active *tris* complex, [Ir(H)$_2$(MesCarCH$_3$)(3,5-Lut)$_3$](Cl).

4.2.2 Reaction of IrCl(COD)(MesCarCH$_3$) with py and p-H$_2$ at 298K and the formation of [Ir(H)$_2$(MesCarCH$_3$)(3,5-Lutidine)$_3$]Cl (11)
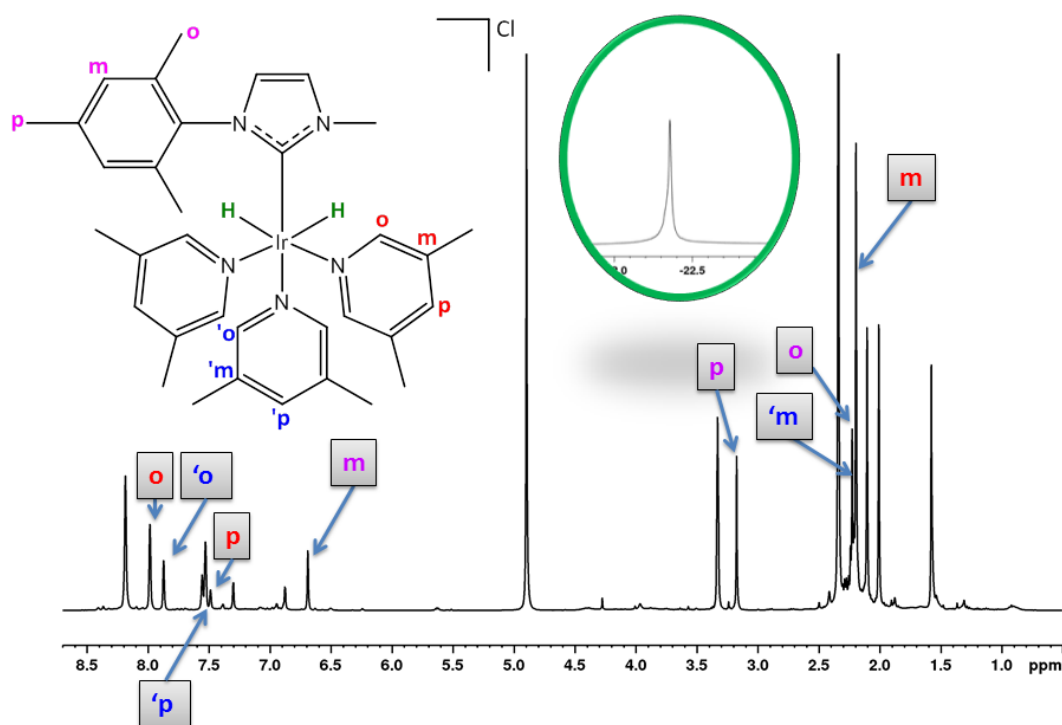
Figure 49: ^{1}H NMR spectrum of the SABRE active complex, [Ir(H)$_2$(MesCarCH$_3$)(3,5-lutidine)$_3$]Cl, that forms with 5 equivalents of 3,5- lutidine in CD$_3$OD. In this spectrum, one clear hydride signal is observed at about δ −22.40, this is the fully activated SABRE *tris* complex that forms, with three bound 3,5-Lutidine substrate molecules which illustrated in this spectrum.

3 atm of *para*-H$_2$ was added to the NMR tube and shaken for 10 seconds in a 65 G magnetic field and a 1 scan ^{1}H NMR spectrum was acquired. In the ^{1}H NMR spectrum, seen in Figure 49, the equivalent hydride signal at δ −22.35 corresponds to the SABRE active complex. The corresponding signals for the region of the substrate, 3,5-lutidine, are seen for the equatorial bound 3,5-lutidine at δ 7.99 for the *ortho* bound protons, δ 7.56

for the *para* bound protons and the *meta* CH$_3$ protons at δ 2.20. We are also able to characterise the corresponding signals for the axial bound 3,5-lutidine at δ 7.88, 7.49 and 2.01 for the *ortho*, *para* and *meta*-CH$_3$ protons. Along with the free 3,5-lutidine at δ 8.20, 7.55 and 2.30, this is all the substrate signals identified for the is the *ortho*, δ 7.93 is the *para* and δ 7.53 is the *meta* peaks for the complex [Ir(H)$_2$(MesCarCH$_3$)(3,5-Lutidine)$_3$]Cl. The ^{1}H NMR spectrum allows us to also identify the signals for the MesCarCH$_3$ NHC, with corresponding resonances at δ 7.30 and 6.88 for the imidazolium backbone protons, at δ 6.69 for *meta* protons of the mesital ring, the CH$_3$ *para* protons at δ 3.18 and the CH$_3$ *ortho* protons at δ 2.23. The final CH$_3$ corresponds to the CH$_3$ substituent bound to the nitrogen of the imidazolium with a resonance at δ 2.11. The SABRE active catalyst, , was fully characterised by NMR and this can be found in section 6.4.17.
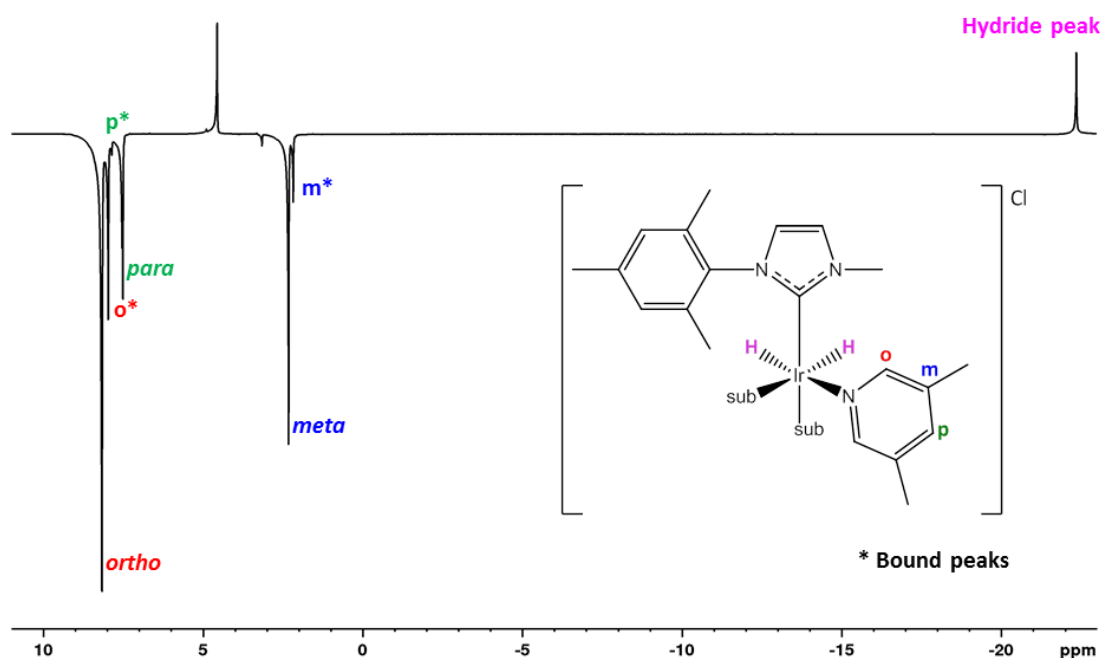
Figure 50: ^{1}H hyperpolarised NMR spectrum of the SABRE active complex, [Ir(H)$_2$(MesCarCH$_3$)(3,5-Lut)$_3$][Cl]

We also observe the hyperpolarised spectrum in Figure 50, where once *para*hydrogen is added to a CD$_3$OD solution containing IrCl(COD)(MesCarCH$_3$) with 5 equivalents of 3,5-lutidine we observe the formation of [Ir(H)$_2$(MesCarCH$_3$)(3,5-Lutidine)$_3$]Cl, and also the hyperpolarisation from the *para*hydrogen derived hydrides that transfer polarisation to the bound 3,5-lutidine which exchanges with the free 3,5-lutidine causing antiphase signals for both the bound and free 3,5-lutidine signals. Figure 50, successfully shows us that the complex, [Ir(H)$_2$(MesCarCH$_3$)(3,5-Lutidine)$_3$]Cl, forms but also that it is an efficient SABRE complex with a total signal enhancement of 719.

4.3 [IrCl(COD)(MesCarBenzyl)] (12)

The next asymmetric NHC complex that will be examined with SABRE through a series of reactions to determine its intermediates and to also investigate whether it is an efficient SABRE catalyst is IrCl(COD)(MesCarBenzyl). I also hypothesise that this SABRE active catalyst, [Ir(H)$_2$(MesCarBenzyl)(3,5-Lutidine)$_3$]Cl, will form and be more efficient in SABRE than both [Ir(H)$_2$(PhCarCH$_3$)(3,5-Lutidine)$_3$]Cl and [Ir(H)$_2$(MesCarCH$_3$)(3,5-Lutidine)$_3$]Cl due the bulky nitrogen substituents on the NHC providing more electron-donation which in turn provides a more steric and electronically stability catalyst.

4.3.1 Reaction of 12 with 3,5-Lutidine in CD$_3$OD

To a solution containing [IrCl(COD)(MesCarBenzyl)] in CD$_3$OD, 5 equivalent of 3,5-lutidine was added and as stated, previously we expect to see the formation of [Ir(COD)(NHC)(sub)]Cl, however in this instance we are unable to observe the formation of [Ir(COD)(MesCarBenzyl)(3,5-lutidine)]Cl where 3,5-lutidine binds to the iridium centre. This is potentially due to the temperature being at 298 K causing the lines to broaden.

4.3.2 Initial H$_2$ addition to IrCl(COD)(MesCarBenzyl) and hydride migration in [Ir(H)$_2$(COD)(MesCarBn)(3,5-Lutidine)]Cl

Once the formation of [Ir(COD)(MesCarBenzyl)(3,5-lut)]Cl was unable to be observed, hydrogen was then added to witness the formation of the SABRE precursor, [Ir(H)$_2$(COD)(MesCarBenzyl)(3,5-Lutidine)]Cl (**12a**) in CD$_3$OD, to a solution containing with 5 equivalents of 3,5-lutidine as the substrate. The sample is shaken for about 10 seconds outside the NMR spectrometer and a ^{1}H NMR spectrum was immediately acquired. However, we were unable to observe the formation of [Ir(H)$_2$(COD)(MesCarBenzyl)(3,5-Lutidine)]Cl and in turn observed the SABRE-active complex, [Ir(H)$_2$(MesCarBenzyl)(3,5-Lutidine)$_3$]Cl forming. The hydrides resonance corresponds with this complex were observed at δ −22.30 seen in Figure 51.

4.3.3 Reaction of IrCl(COD)(MesCarBn) with py and *p*-H$_2$ at 298K and the formation of [Ir(H)$_2$(MesCarBn)(3,5-Lutidine)$_3$]Cl (13)

3 atm of *para*-H$_2$ is added to the NMR tube and is then shaken for 10 seconds in a 65 G magnetic field and a 1 scan ^{1}H NMR spectrum is acquired. In the ^{1}H NMR spectrum the equivalent hydride signal at δ −22.76 corresponds to the SABRE active complex **13** with 3 3,5-lutidine bound to the complex. SABRE-active catalyst, **13**, was fully characterised by NMR and this can be found in section 6.4.5.
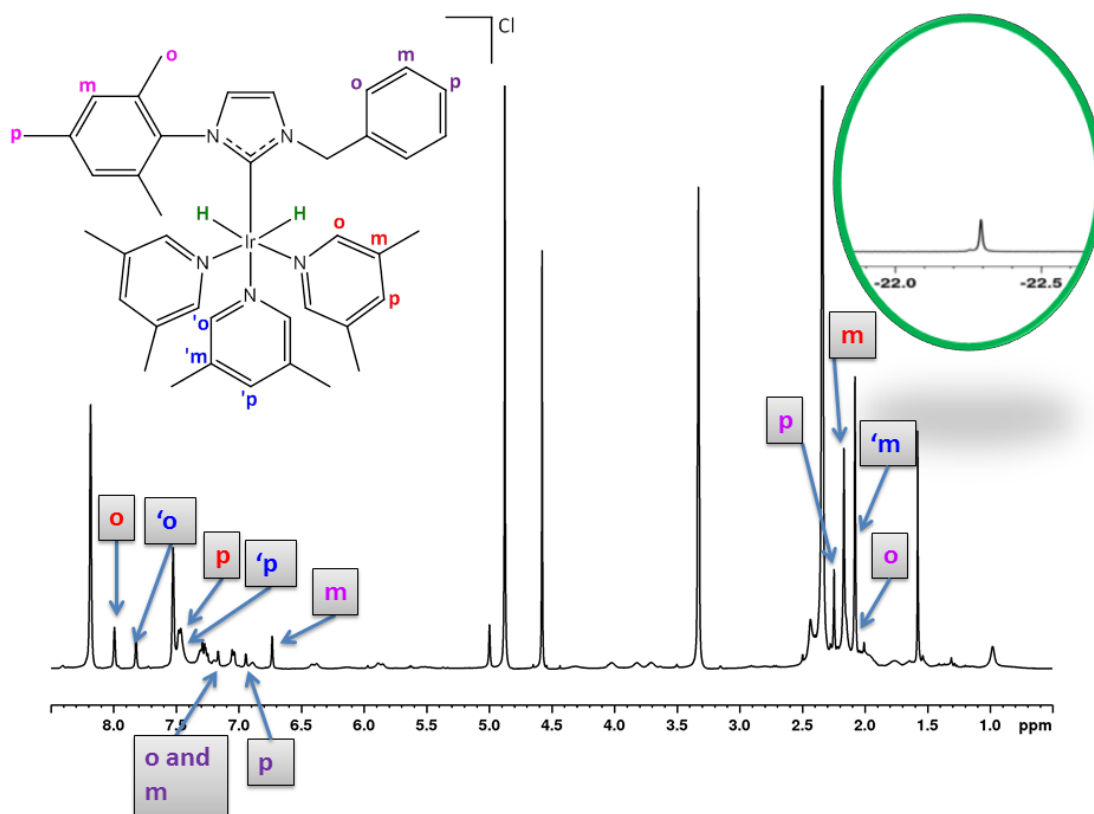
Figure 51: ¹H NMR spectrum of the SABRE active complex, [Ir(H)₂(MesCarBenzyl)(3,5-lutidine)₃]Cl, which forms when IrCl(COD)(MesCarBenzyl) and 5 equivalents of 3,5- lutidine are dissolved CD₃OD. In this spectrum, we observe a hydride signal is observed at about δ −22.40 and this is the activated SABRE *tris* complex that forms, with three bound 3,5-Lutidine substrate molecules.

The ¹H NMR spectrum seen in Figure 51, shows the SABRE active complex [Ir(H)₂(MesCarBenzyl)(3,5-lutidine)₃]Cl which forms when *para*-H₂ is dissolved in a complex at 3 bar pressure containing IrCl(COD)(MesCarBenzyl) with 5 equivalents of 3,5-lutidine in CD₃OD. The corresponding resonances that determine this complex are:

- The bound equatorial 3,5-lutidine resonance for the *ortho*, *para* and *meta* protons are observed at δ 7.99, 7.48 and 2.17

- The bound axial 3,5-lutidine resonances for the *ortho*, *para* and *meta* protons are observed at δ 7.82, 7.47 and 2.08

- The *ortho* and *meta* protons on the benzyl ring are observed at δ 7.30

- The imidazolium backbone protons of the carbene are observed at δ 7.17 and 6.94

- The *para* proton on the benzyl ring are observed at δ 7.04

- The *meta* protons on the phenyl ring are observed at δ 6.74

- The only CH_2 protons between the carbene centre and the benzyl ring are observed at δ 5.00
- The *ortho* CH_3 protons on the phenyl ring are observed at δ 2.07 the *para* CH_3 protons on the mesial ring are observed at δ 2.26
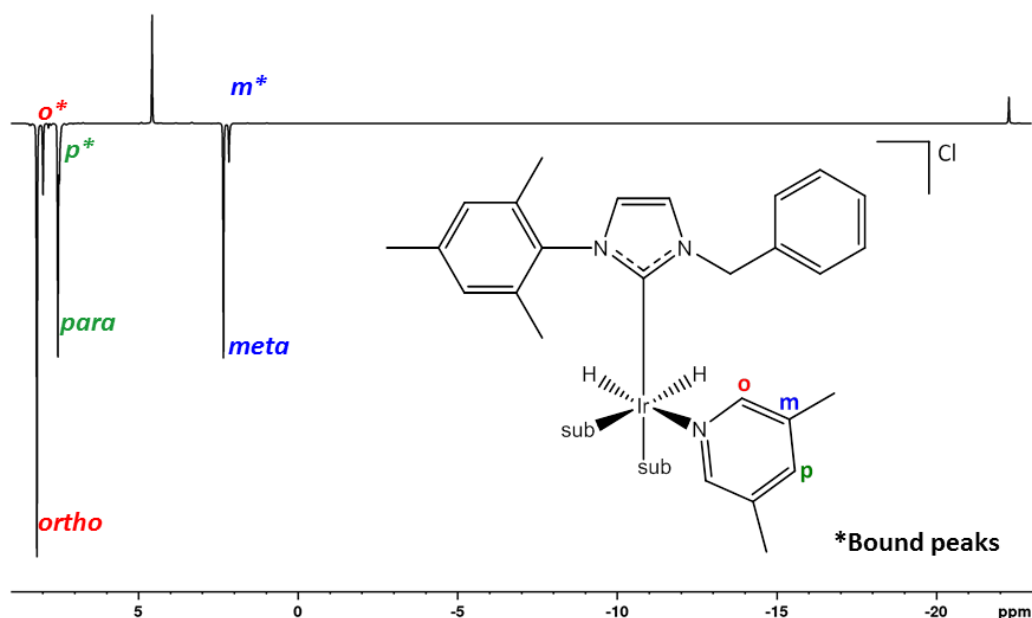
Figure 52: Hyperpolarised 1 scan ^{1}H NMR spectrum that illustrates the formation of the SABRE-active catalyst free 3,5-Lutidine [Ir(H)$_2$(MesCarBenzyl)(3,5-lutidine)$_3$]Cl which also undergoes polarisation and the free 3,5-lutidine resonances that also polarised which occurs due to the exchange between the free and bound 3,5-lutidine molecules.

We observe the hyperpolarised spectrum in Figure 52, when *para*hydrogen is added to a CD$_3$OD solution containing IrCl(COD)(MesCarBenzyl) with 5 equivalents of 3,5-lutidine where this formation of [Ir(H)$_2$(MesCarBenzyl)(3,5-Lutidine)$_3$]Cl is observed. The hyperpolarisation spectrum successfully shows us that the complex, [Ir(H)$_2$(MesCarCH$_3$)(3,5-Lutidine)$_3$]Cl, forms with a total signal enhancement of 911-fold. This is the highest signal enhancement produced out of the array of asymmetric complexes. Based on this enhancement, this complex becomes the most efficient SABRE-active catalyst amongst the other asymmetric SABRE-active catalysts so far, [Ir(H)$_2$(PhCarCH$_3$)(3,5-Lutidine)$_3$]Cl and [Ir(H)$_2$(MesCarCH$_3$)(3,5-Lutidine)$_3$]Cl, which have lower total signal enhancements of 1-fold and 719-fold.

4.4 [IrCl(COD)(MesCarHomoBenzyl)] (14)

The last asymmetric NHC complex that will be examined with SABRE and investigated to witness whether it is an efficient SABRE catalyst is IrCl(COD)(MesCarHomoBenzyl). It is

hypothesised that this SABRE active catalyst, [Ir(H)$_2$(MesCarHomoBenzyl)(3,5-Lutidine)$_3$]Cl, will form and due to the bulky nitrogen substituents that it could be a better SABRE-active catalyst with high efficiencies than [Ir(H)$_2$(PhCarCH$_3$)(3,5-Lutidine)$_3$]Cl, [Ir(H)$_2$(MesCarCH$_3$)(3,5-Lutidine)$_3$]Cl and [Ir(H)$_2$(MesCarBenzyl)(3,5-Lutidine)$_3$]Cl.

4.4.1 Reaction of 14 with 3,5-Lutidine in CD$_3$OD

[IrCl(COD)(MesCarHomoBenzyl)] and 5 equivalent of 3,5-lutidine was added to a solution containing 600 μL of CD$_3$OD and as stated previously we expect to see the formation of [Ir(COD)(NHC)(sub)]Cl. Unfortunately, in this instance we are unable to observe the formation of [Ir(COD)(MesCarHomoBenzyl)(3,5-lutidine)]Cl where 3,5-lutidine binds to the metal centre.

4.4.2 Initial H$_2$ addition to IrCl(COD)(MesCarHomobenzyl) and hydride migration in [Ir(H)$_2$(COD)(MesCarHomobenzyl)(3,5-lut)]Cl

When a solution containing IrCl(COD)(MesCarHomoBenzyl) and 3,5-lutidine at 5 equivalents in CD$_3$OD is activated by hydrogen, the sample is shaken outside the spectrometer so the hydrogen dissolves into the solution. We have previously seen in both section 3 and 0, that a complex with two hydrides and one 3,5-lutidine substrate bind to the iridium metal centre. This forms the complex [Ir(H)$_2$(COD)(MesCarHomobBnzyl)(py)]Cl and we would be able to observe bound pyridine substrates in the aromatic region of the NMR spectrum with corresponding hydrides in the hydride region. However, when hydrogen is added to a solution containing IrCl(COD)(MesCarHomoBenzyl) with 5 equivalents of 3,5-lutidine in CD$_3$OD, we are unable to observe the formation [Ir(H)$_2$(COD)(MesCarHomoBenzyl)(3,5-lut)]Cl or any intermediate. However, we are able to observe the formation of the SABRE-active *tris* complex, [Ir(H)$_2$(MesCarHomoBenzyl)(py)$_3$]Cl where three 3,5-lutidine substrates bind to the iridium metal centre along with the parahydrogen derived hydrides with a corresponding hydride signal at δ −22.40 which will be further explain in section 4.4.3.

4.4.3 Reaction of IrCl(COD)(MesCarHomoBenzyl) with py and *p*-H$_2$ at 298 K and the formation of [Ir(H)$_2$(MesCarHomoBenzyl)(3,5-Lutidine)$_3$]Cl (14)

Complex IrCl(COD)(MesCarHomoBenzyl) was dissolved in CD$_3$OD with 5 equivalents of 3,5-lutidine, however we are unable to observe lutidine binding to the metal centre and forming [Ir(COD)(MesCarHomoBenzyl)(3,5-lutidine)]Cl.

Upon adding hydrogen to the solution in CD_3OD, we do not observe the formation of [Ir(H)$_2$(COD)(MesCarHomoBenzyl)(py)]Cl but instead observe the reaction forming the SABRE tris complex [Ir(H)$_2$(PhCarCH$_3$)(3,5-Lutidine)$_3$]Cl immediately with corresponding hydride signals at δ −22.40.

Once *p*-H$_2$ was added to the solution and the sample was shaken for 10 seconds at an approximate 65 G magnetic field. We observe antiphase, hyperpolarised bound substrate signals of the SABRE active *tris* complex, Ir(H)$_2$(MesCarHomoBenzyl)(3,5-Lutidine)$_3$]Cl as seen in Figure 53. The corresponding proton signal in the substrate region for the free 3,5-lutidine peaks for *ortho*, *para* and *meta* protons are at δ 8.20, 7.55 and 2.34.
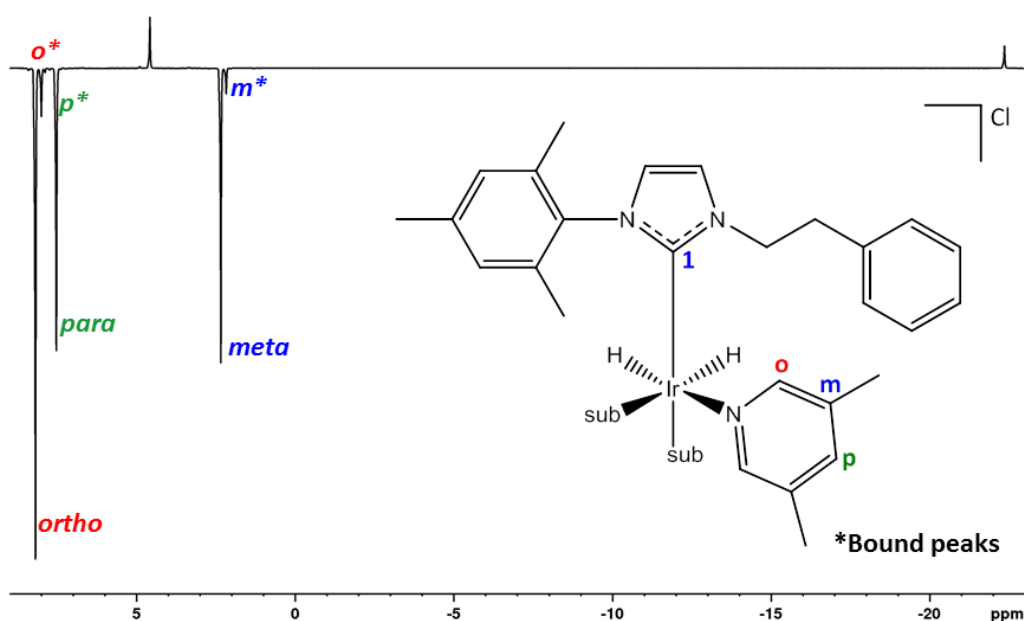
Figure 53: Hyperpolarised 1 scan ^{1}H NMR spectrum which shows the SABRE-active *tris* complex [Ir(H)$_2$(MesCarHomobenzyl)(3,5-Lutidine)$_3$]Cl, polarising in both the free and bound substrate region.

In the ^{1}H NMR spectrum seen in Figure 54, we observe the SABRE active complex [Ir(H)$_2$(MesCarHomoBenzyl)(3,5-lutidine)$_3$]Cl forming, once *para*-H$_2$ is dissolved in a complex at 3 bar pressure in a solution containing IrCl(COD)(MesCarHomoBenzyl) with 5 equivalents of 3,5-lutidine in CD_3OD. This yield corresponding ^{1}H NMR spectrum with resonances that determine that this SABRE-active complex has formed:

- The bound equatorial 3,5-lutidine resonances for the *ortho* is observed at δ 8.00, for the *para* protons at δ 7.51 and the *meta* protons observed at δ 2.17.
- The bound axial 3,5-lutidine resonances for the *ortho* is observed at δ 7.88, for the *para* protons at δ 7.47 and the *meta* protons observed at δ 2.11.
- The two imidazolium backbone protons of the carbene are observed at δ 7.31 and 6.88.

- The *meta* protons on the benzyl ring are observed at δ 7.24, the *para* proton on the benzyl ring are observed at δ 7.19 and the *ortho* protons on the benzyl ring are observed at δ7.03.

- The *meta* protons on the phenyl ring are observed at δ 6.69.

- The only two sets of CH_2 protons between the carbene centre and the benzyl ring are observed at δ 3.74 and 2.96.

- The *ortho* CH_3 protons on the phenyl ring are observed at δ 2.02 and the *para* CH_3 protons on the mesityl ring are observed at δ 2.23.
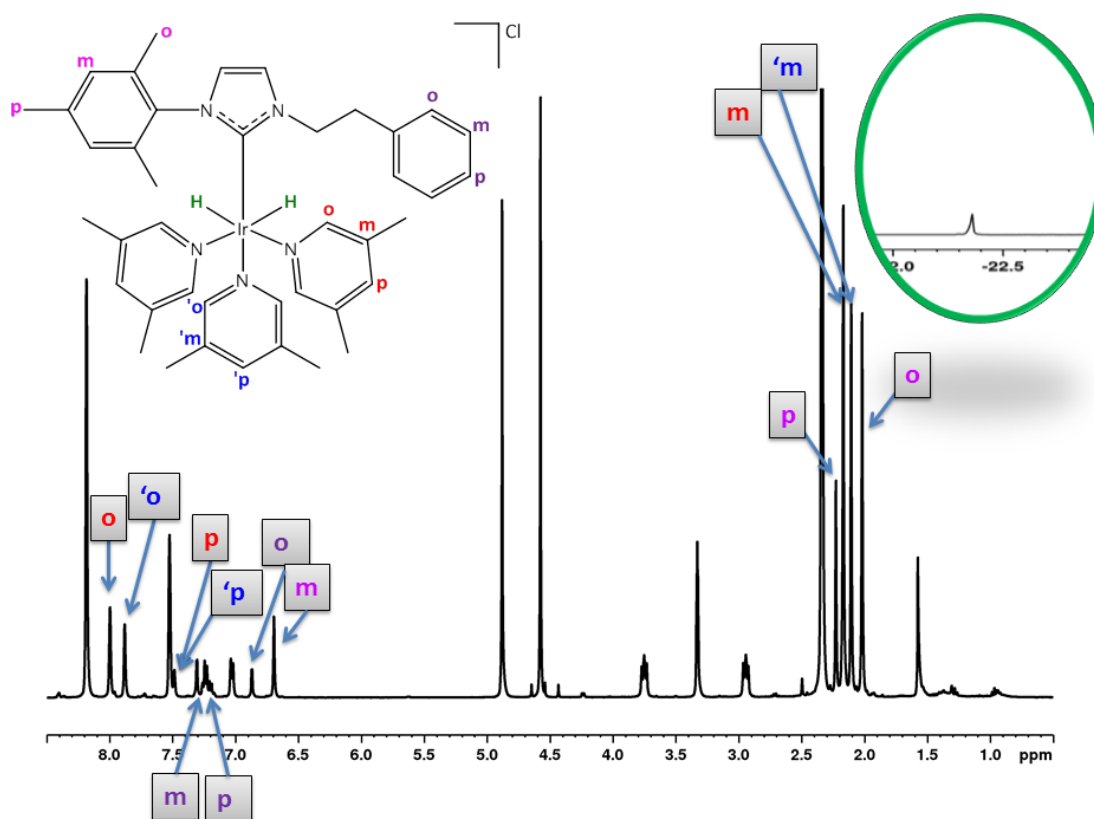
Figure 54: A 32 scan ^{1}H NMR spectrum which observes the resonance peaks which correspond to the formation of the SABRE-active catalyst [Ir(H)$_2$(MesCarHomoBenzyl)(3,5-lutidine)$_3$]Cl, which forms once parahydrogen is added to a solution containing IrCl(COD)(MesCarHomoBenzyl).

As illustrated in Figure 53, the hyperpolarised NMR spectrum shows the polarisation of both the free and the bound equatorial 3,5-lutidine. The hyperpolarised spectrum successfully shows us that [Ir(H)$_2$(MesCarHomoBenzyl)(3,5-Lutidine)$_3$]Cl forms with a total signal enhancement of 371-fold. This is the second highest signal enhancement produced out of the entire asymmetric complex which based on the hypothesis stated in section 4.4 is incorrect where it was hypothesised that the asymmetric SABRE-active catalyst with the

largest N-substituent would produce the largest total signal enhancements. This hypothesis will be discussed in more detail later.

4.5 Summary and Discussion

In this chapter, asymmetric SABRE-active catalysts were examined with 3,5-lutidine as the substrate of choice. 3,5-lutidine is a pyridine-derivative and found in a number of drug molecules which can go on to potentially be used as MRI contrast agents. The asymmetric complexes, IrCl(COD)(NHC) where NHC=PhCarCH$_3$, MesCarCH$_3$, MesCarBenzyl or MesCarHomoBenzyl, underwent a series of reactions and displacements where they all formed SABRE-active catalysts [Ir(H)$_2$(NHC)(3,5-lutidine)$_3$]Cl where NHC = PhCarCH$_3$, MesCarCH$_3$, MesCarBenzyl or MesCarHomoBenzyl. All of these asymmetric complexes were observed to form SABRE-active catalysts and the hyperpolarised signal intensities that result were found to vary depending on the NHC.

The NHC with the least bulkiest nitrogen substituents is IrCl(COD)(PhCarCH$_3$) and produces the lowest polarisation levels at 11-fold when compared to the other asymmetric catalysts. The NHC with the most bulkiest nitrogen substituents is IrCl(COD)(MesCarHomoBenzyl) and is better than the former complex in accordance with faster ligand dissociation. The highest polarisation level results from SABRE-active catalyst [Ir(H)$_2$(MesCarBenzyl)(3,5-lutidine)$_3$]Cl at 911-fold. This indicates that a fine balance is needed between being too sterically bulky, and the ligand loss rate being too rapid for polarisation transfer, as well as being too small and the bonding being too strong. [Ir(H)$_2$(MesCarHomoBenzyl)(3,5-lutidine)$_3$]Cl seems to reflect a happy medium having one large nitrogen substituent, and one smaller substituent. These two side chains now acts to improve polarisation transfer from the hydrides to the substrate (illustrated in Figure 18). Hence the original premise of this work is proven.

It is believed that an asymmetric complexes have the potential to exceed the performance of the commonly used SABRE-active catalyst associated with the current literature. It should be emphasised that the conditions used for polarisation transfer with these asymmetric complexes were not fully optimised, although a standard set of conditions were used, so hence they are comparable. It is recommended in the future these studies are repeated at different temperature and with a wider range of substrates to further develop this theme.

It took around 4 years of optimisation for the original SABRE catalysts to produce the published results of Rayner et al.[82] It is therefore believed these results reflect a

significant addition to the body of work already reported for SABRE. It has been learnt that CH bond activation needs to be avoided as this affects the SABRE catalysts longevity.

5 Conclusions and Future Work

5.1 Conclusions - Symmetric vs Asymmetric

This thesis has demonstrated that changing the NHC on the SABRE-active catalyst can either increase or decrease SABRE efficiencies. The work in this thesis was started by investigating two new symmetric complexes, 1 and 3, and optimising them for SABRE. The synthetic route was explained and the SABRE-active forms of these complexes were analysed by looking at their exchange rates and analysing the thermodynamic parameters.

The results of these data allowed it to be concluded that changing the NHC can beneficially affect the steric effects of SABRE and affect the ligand exchange. By analysing the rate constants and thermodynamic properties for the ligand loss of pyridine, it was determined that there is a direct correlation to electronic and steric bulk, whereby increasing the steric bulk, which in turn increases the electron donating power of the NHC, decreases the Gibbs free energy making it more negative.[1] This draws a link between polarisation efficiencies, ligand exchange and the NHC complexes examined. Figure 55 shows a graph with the calculated Gibbs free enthalpy (explained in section 7.2) and actually indicates that the SABRE-active complex of [IrCl(COD)(IXy)] has the lowest Gibbs free enthalpy out of all the complexes examined, which from the theory stated previously is not correct. We would expect IMes to have the lowest Gibbs free energy from the steric bulk of the catalyst. This data concludes that the efficiency of SABRE catalysts cannot be predicted and that not steric alone cannot determine the hyperpolarisation efficiency of a SABRE catalyst.
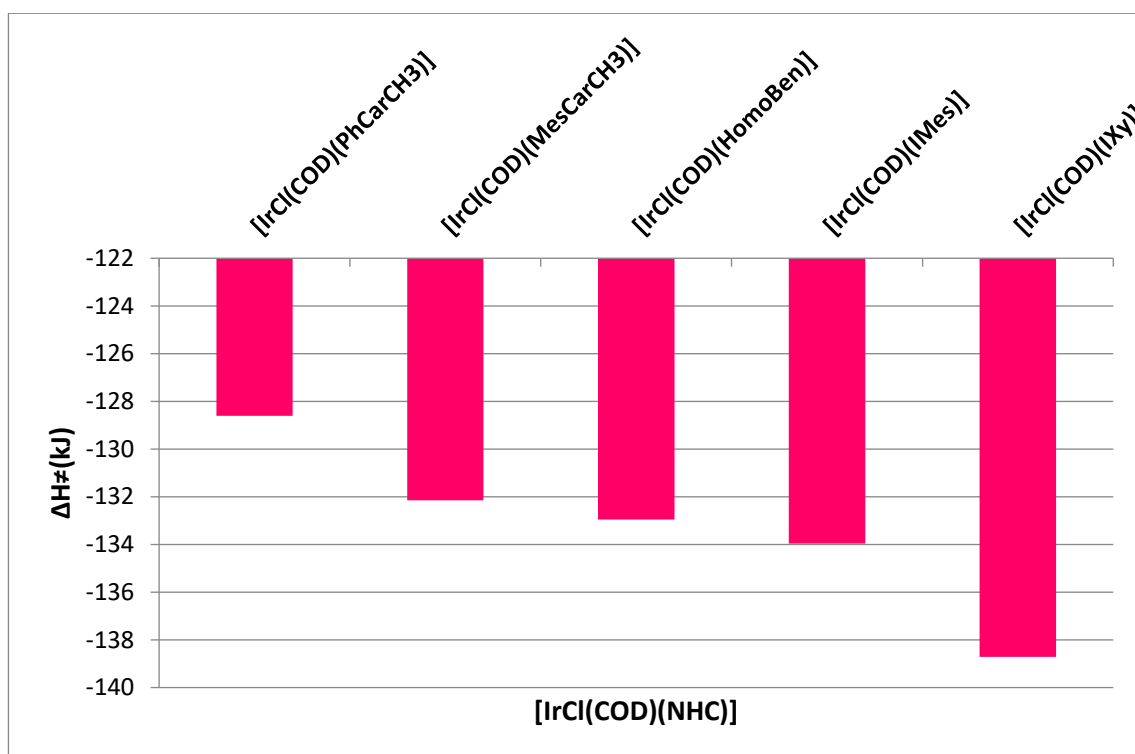
Figure 55: A graph of the Gibbs free entropy (ΔH$^{\neq}$) plotted as a function of the NHC utilised in the complex IrCl(COD)(NHC).

For the two symmetric complexes, IXy and ITol, key components were optimised such as solvent, substrate concentration and temperature. Both $[Ir(H)_2(IXy)(py)_3]Cl$ and $[Ir(H)_2(ITol)(py)_3]Cl$ were able to polarise, however $[Ir(H)_2(ITol)(py)_3]Cl$ had very low polarisation levels of 0.5-fold and we were unable to observe the exchange rate. This makes $[Ir(H)_2(IXy)(py)_3]Cl$ a better choice as its polarisation levels were much higher at a total polarisation enhancement of 102-fold. The solvents role had a significant effect as well on the polarisation transfer and the intermediates that were visible through the experiments. Both methanol and dichloromethane were the solvents investigated, for $[Ir(H)_2(IXy)(py)_3]Cl$ with pyridine as the substrate, maximum signal enhancements and the intermediates were more clearly identifiable in methanol. Whereas, for $[Ir(H)_2(ITol)(py)_3]Cl$ with pyridine as the substrate, intermediates were not observed for either solvents but had a higher signal enhancement of 11-fold in dichloromethane. Ruddlesden et al proved that the low polarity solvents can affect the efficiency of charged nature species so to fully optimise these complexes a range of solvents and substrates would need to be tested to understand how these would affect their SABRE efficiencies.[71]

We also investigated asymmetric NHC complexes, along with IMes as the control, with 3,5-lutidine as the substrate. As CD_3OD is the solvent used with IrCl(COD)(IMes) and pyridine which is currently the SABRE-active catalyst with the greatest SABRE efficiencies, were also used as the solvent in the asymmetric studies. We were able to polarise with all

the SABRE-active asymmetric complexes, however [Ir(H)$_2$(MesCarBenzyl)(3,5-lutidine)$_3$]Cl produced the greatest signal enhancements even higher than [Ir(H)$_2$(IMes)(3,5-lutidine)$_3$]Cl making it the most efficient SABRE catalyst in. [Ir(H)$_2$(PhCarCH$_3$)(3,5-lutidine)$_3$]Cl had the lowest polarisation enhancements; we expect this due to the nitrogen substituents not being bulky enough.

As [Ir(H)$_2$(MesCarBenzyl)(3,5-lutidine)$_3$]Cl produced the highest polarisation enhancements at 911-fold out of both the symmetric and the asymmetric complexes, this complex is the most efficient SABRE catalyst in this research. However, to be truly able to compare the symmetric and asymmetric complexes, both pyridine and 3,5-lutidine would need to be examined with all complexes and various controls such as temperature, substrate concentration and solvent used would need to be examined with both the symmetric and asymmetric complexes.

From all the data collected in this thesis, it can be determined that the asymmetric SABRE-active catalysts have the potential to exceed the commonly used symmetric SABRE-active catalyst associated with SABRE.

While this thesis has aimed to demonstrate the effects on polarisation transfer when varying the NHC ligand and how this can affect the hyperpolarisation enhancement, it has also brought to the attention that there are many limitations. The polarisation transfer can be affected by many variables which means that optimisation can be difficult and a prolonged process.

5.2 Future work - Symmetric complexes

For the symmetric complexes studied throughout this thesis, **1** and **5**, two different temperatures of 233 K and 298 K were used when pyridine was added to complex; this was then analysed and characterised to determine the structures formed when the substrate was added, but more importantly when *para*hydrogen was added at 3 bar pressure to activate the complex. A hyperpolarisation method known as the shake and drop method was then used to achieve polarisation transfer through a chemical exchange in an approximate 65 G magnetic field. To examine the complex more intently, temperature between 233 K and 298 K should also be analysed to determine which temperature achieves the greatest SABRE enhancements thereby identifying when the catalyst is at its most efficient.

The other key areas which need further investigation would be to examine the reproducibility of the polarisation transfer achieved in an NMR tube. The shake and drop method is currently used throughout this thesis to achieve polarisation, however the lack

of reproducibility has been questioned so a hyperpolarisation method using a flow system is a way to overcome the reproducibility problem. This would then allow us to develop more understanding of the SABRE symmetric catalysts **4** and **7** by studying the effects certain characteristics have on changing the efficiency of the SABRE active complexes. The effects that could be studied to broaden our understanding are: the amount of time *para*hydrogen is bubbled through the sample solution in the mixing chamber which within the flow system is used instead of an NMR tube. Also, the pressure of parahydrogen gas placed in the solution along with the how the magnetic field strength can affect the polarisation transfer stage.[83]

5.3   Future work - Asymmetric complexes

Throughout this thesis, 3,5-Lutidine was the substrate of choice and worked well along with the NHC stabilised iridium complexes to form SABRE-active complexes. However, to be able to optimise the catalyst efficiencies for SABRE and to prove whether asymmetric or symmetric complexes give larger polarisation enhancements therefore making them more efficient SABRE active catalysts, then pyridine and 3,5-lutidine need to be examined for both symmetric and asymmetric complexes to derive which SABRE active-catalysts works the best for SABRE before optimising the conditions of the catalyst by substrate concentration and temperature. Ideally, as the human body's optimum temperature is around 310 K, the catalysts must work most efficiently as this temperature if they were used as MRI contrast agents. Therefore, it is important to study and determine which SABRE active catalysts exhibits the most efficiency at these temperatures by performing temperature studies.[1, 84] It would also be interesting to determine the rate of ligand exchange for IrCl(COD)(MesCarBenzyl) and determine whether it competes with SABRE efficiencies of both IrCl(COD)(IXy) and IrCl(COD)(MesCarHomoBenzyl).

5.4   Other Areas of interest

An area of interest is the development of a SABRE catalyst which is biologically safe to use within the human body so not only does the catalyst itself need to be biochemically safe but also the solvent system that contains the SABRE catalyst must be safe to use in clinical settings.[85] Throughout this project, CD_3OD and CD_2Cl_2 were used which unfortunately can be toxic to the human body so other solvents such as ethanol and water are preferred to be used instead. There has been great difficulty with using water where polarisation has not been as efficient producing short lived hyperpolarisation in proton NMR.[48] However, since completing this thesis; hyperpolarisation has been achieved by Colell *et al*, where a SABRE catalyst has directly hyperpolarised in ^{15}N nuclei in pure H_2O or D_2O.[49, 86]

During this thesis work was also began to investigate acetone as a co-ligands. This can improve the polarisation enhancements which in turn improves the efficiency of the SABRE-active catalyst. This work has previously been examined by the Duckett group where acetonitrile has been used as the co-ligand increasing the ^{1}H signal enhancement from 20-fold to 60-fold.[81]

Currently all the NMR spectroscopic work achieved throughout this thesis is done on a high field (9.4T) NMR spectrometer, and recently within the Duckett group a low cost low-field permanent magnet system (1T) has been used to detect signal enhancement intensities from SABRE active catalysts. This low-cost NMR is much more desirable as less money is required to run these experiments.[87]

6   Experimental

6.1   Instrumentation

6.1.1   NMR Spectrometry

All characterisation of complexes by NMR spectroscopy was carried out using Avance III 400 MHz and Avance III 500 MHz spectrometers, where the ^{1}H frequency is measured at 400.1 MHz and 500.1 MHz. The ^{13}C NMR frequency is measured at 100.6 MHz for the 400 MHz and 202.5 MHz for the 500 MHz. Data processing and acquisitions were examined using Bruker Topspin software versions 3.5. The ^{15}N NMR frequency is measured at 40.6 MHz for the 400 MHz and 50.7 MHz for the 500 MHz.

NMR deuterated solvents used throughout the course of this research were d_2-dichloromethane and d_4-methanol. For d_2-dichloromethane (DCM), the residual reference signal is d_1-dichloromethane proton (CDHCl$_2$) and for d_4-methanol, the residue reference signal is the proton in d_3-methanol (CHD$_2$OD).

Multiplicities are stated as s for singlet, d for doublet, t for triplet, q for quartet and m for multiplet. J couplings are quoted in Hertz (Hz).

6.1.2   Mass Spectrometry

ESI is a relatively soft ionisation analytical technique used to detect different ionic substances in a compound. The molecular ion signals were observed on a Bruker micrOTOF time of flight mass spectrometer using electrospray ionisation (ESI) techniques. An ESI source was used to collect the data (ESI-MS).

6.1.3   *Para*hydrogen preparation

*Para*hydrogen is produced by cooling hydrogen gas to around 30K over a paramagnetic material, Fe$_2$O$_3$, which acts as the catalyst. This process occurs in a closed cycle helium refrigeration unit producing p-H$_2$ where the concentration is over 99%. The pressure of *para*hydrogen used was at 3 bar.

6.2   Standard methods

6.2.1   Hyperpolarisation method – Shake and Drop

Hyperpolarisation methods were examined using 5mm NMR tube equiped with a Young's valve. The sample, 5 mg of chosen complexes (symmetric complexes) with 5 equivalents of substrate and 0.6mL of solvent, was used unless stated otherwise. A sample was then

degassed using a high vacuum line to evacuate air out of the NMR tube and activated by adding hydrogen gas at a pressure of 3 bar.

For each shake and drop experiment, the evacuation of the headspace of the NMR tube is required so that p-H_2 (3 bar) can be added. The sample is then shaken at approximately 65 G using the stray magnet field outside of the NMR spectrometer for 10 seconds before quickly inserting the tube into the NMR spectrometer. A single scan is collected with a 90° pulse angle and the receiver gain set to 1 as standard.

6.2.2 Calculations of enhancement factors

The calculations used for NMR enhancements, ε, were calculated using the formula:

$$\varepsilon = \frac{\text{Hyperpolarised signal integral}}{\text{Thermal signal integral}}$$

The acquisitions for both the thermal and the hyperpolarised signal were kept the same along with the receiver gain and the number of scans. Thermal signals were taken after the activated sample had reached thermal equilibrium and aligned with the magnetic field in the spectrometer, which could be anytime between 1 to 10 minutes after polarisation.

A hyperpolarised signal appears as a negative enhanced peak so when quoted the enhancement factor is also negative.

6.3 Synthesis

The symmetric and asymmetric complexes made within the Duckett Group by Peter Rayner except for the asymmetric complexes [IrCl(PhCarCH$_3$)(COD)] and [IrCl(MesCarCH$_3$)(COD)]. The complex IrCl(COD)(^{t}BuBIM) was synthesised by me.

6.3.1 Iridium Dimer [Ir(COD)Cl]$_2$
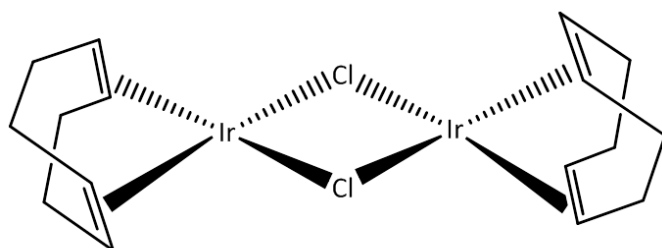
Figure 56: Iridium Dimer where COD = 1,5-cyclooctadiene

Isopropanol (3 mL) and distilled water (1.25 mL) were stirred under nitrogen gas for 10 minutes. Iridium trichloride (250 mg, 0.84 mmol) was added to a microwave vial (2.5 mL- 5.0 mL) with a stirrer bar and flushed with nitrogen gas for 10 minutes.

Into the flask containing isopropanol and distilled water, 1,5 – cyclooctadiene (3.5eq.) was added and stirred under nitrogen for another 10 minutes. The resulting solution was added to the microwave vial which was flushed with nitrogen gas for a further 10 minutes. The vial was then placed in the microwave at 90 °C for 20 minutes. The vial was again placed in the microwave for a further 20 minutes at 90 °C and then at 80 °C for 25 minutes. The vial is then left in the freezer for 24 hours.

6.3.2 Symmetric complexes

6.3.2.1   [IrCl(IMes)(COD)]
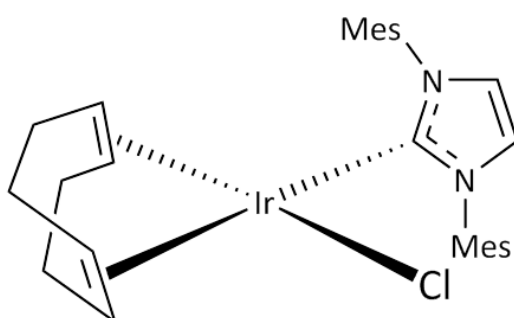
Figure 57: IMes Carbene [IrCl(IMes)(COD)] which was synthesised within the Duckett Group where IMes = 1,3-bis-(2,4,6-trimethylphenyl)-imidazol-2-ylidene

[IrCl(IMes)(COD)] was synthesised within the Duckett group according to the procedures in the literature[88].

6.3.2.2   [IrCl(IXy)(COD)]
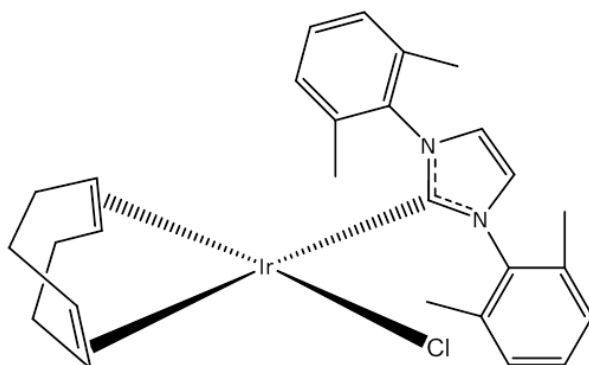
Figure 58: IXy Carbene [IrCl(IXy)(COD)] which was synthesised within the Duckett Group

Glyoxal (1.0 eq.) was added with formic acid (2 drops) in a stirred solution of 2,6-Dimethylaniline (2.0eq.) in Methanol or Ethanol at rt. The resulting solution was then stirred for 16 hours at rt forming a yellow precipitate. The yellow precipitate was then filtered and washed with methanol and ethanol then dried under a vacuum to give an N,N'-Bis(2,6-dimethylphenyl)-1,2-ethanediimine (Ethylenediimine). To the ethylenediimine, a paraformaldehyde (1.1eq.) in 4M hydrochloric acid (1.5eq.) solution was added dropwise in ethyl acetate under nitrogen gas. The resulting solution is then stirred for 16 hours at rt forming an off white precipitate. The precipitate is then washed and filtered with ethyl acetate then dried under vacuum forming imidazolium chloride. KO^{t}Bu (2.4eq.) was added to a solution of the carbene (2.2eq.) in THF under nitrogen gas and stirring at rt and then stirred for 30 minutes at rt. [Ir(COD)Cl$_2$ (1.0eq.) was added to the resulting solution and stirred for a further 2hours at rt. The solvent was then removed via reduced pressure and purified over flash column chromatography on silica with DCM giving the IXy carbene shown in Figure 58.

Yield: 95 %

6.3.2.3 [IrCl(ITol)(COD)]
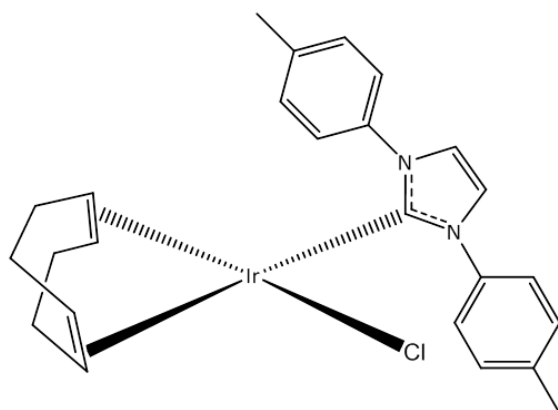
Figure 59: ITol carbene [IrCl(ITol)(COD)]

The ITol carbene complex was synthesised by using a similar procedure seen for IrCl(IXy)(COD). To the *p*-Toluidine solution (2.0 eq.) stirring, glyoxal (1.0 eq.) and formic acid (2 drops) were added in methanol or ethanol at rt. The solution was then stirred for 16h at rt forming a yellow precipitate. This was then filtered and washed with methanol and ethanol and then dried under vacuum giving the ethylenediimine. To this, paraformaldehyde (1.1eq.) in 4M HCL in 1,4-dioxane (1.5 eq.) The solution was added dropwise to the ethylenediimine (1.0eq.) in ethyl acetate at rt under nitrogen gas. The solution was then stirred for 16 hours forming an off white precipitate. This was then filtered, washed with ethyl acetate and dried under vacuum giving 1,3-Bis(4-

methylphenyl)imidazolium chloride. To the imidazolium chloride carbene (2.2 eq.) in THF, KO^{t}Bu (2.4 eq.) was added and stirred at rt for 30 minutes. Then, a solution containing \[Ir(COD)Cl]$_2$ (1.0 eq.) was added to the resulting solution and stirred for 2h at rt. The solvent was then removed under reduced pressure and purified by flash column chromatography on silica with DCM giving, a yellow crystalline solid, [IrCl(ITol)(COD)].

Yield: 70%

6.3.2.4   [IrCl(^{t}BuBIM)(COD)]
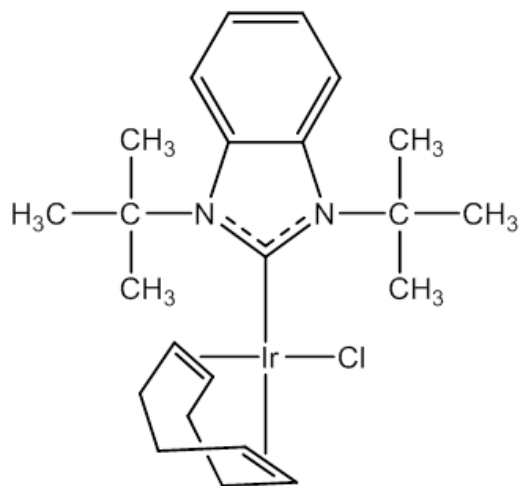
Figure 60: ^{t}BuBIM carbene [IrCl(^{t}BuBIM)(COD)]

1,3-Di-*tert*-butylimidiazolium chloride (145.7 mg, 0.546 mmol) and Ag$_2$O (63.9mg, 0.273 mmol) were added to DCM (5 mL) and stirred at rt for 2 hours. Foil was used to shield the suspension from light. [Ir(COD)Cl]$_2$ (183 mg, 0.273 mmol) was then added to the solution and stirred at rt for a further 4 hours. The resulting solution was then purified by column chromatography (on silica with DCM as the eluent), filtered and the solvent was removed under reduced pressure forming a yellow solid.

Yield: 62 %

6.3.3 Asymmetric complexes

6.3.3.1 *[IrCl(MesCarEtBn)(COD)]*
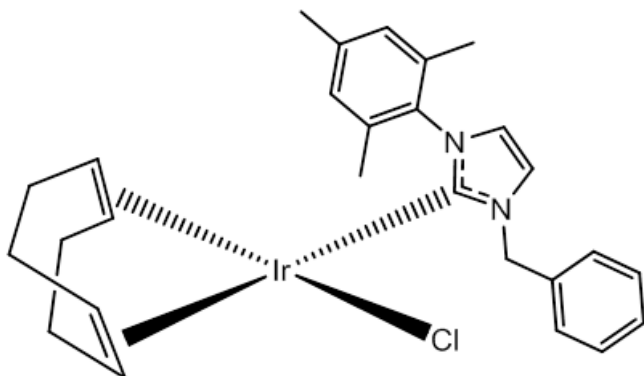
Figure 61: IMesCarEtBn Carbene [IrCl(MesCarEtBn)(COD)] which was synthesised within the Duckett Group where IMes = 1,3-bis-(2,4,6-trimethylphenyl)-imidazol-2-ylidene

MesCarEtBn.BPH$_4$ (101 mg, 0.170 mmol) was dissolved partially in acetone (20 mL). To the suspension, K$_2$CO$_3$ (127 mg, 0.920 mmol) was added and stirred for 15 minutes at room temperature before [Ir(COD)Cl]$_2$ (57.2 mg, 0.00852 mmol) was added. This formed a bright orange mixture which was then heated under reflux for 4 hours where the mixture changes to an orange-yellow in colour. The mixture was then cooled to room temperature and filtered through celite; then evaporated to give an orange-yellow residue. The residue was then re-dissolved in DCM (20 mL), where a white solid precipitates out. The mixture was then filtered through celite once again and the solvent was evaporated off to give an orange-yellow solid. The solid was re-dissolved in hexane (30 mL) and heated, whilst stirring, in a water bath at 40 °C for approximately 15 minutes. The solution was then filtered and the two previous steps were repeated twice more until a brown solid remains undissolved. The yellow solution that was continuous collected was combined and reduced in volume to approximately 10mL. The yellow solution was then placed in a freezer overnight to give the IEtBn carbene as yellow needle-like crystals.

Yield: 84 %

6.3.3.2 [IrCl(MesCarBn)(COD)]
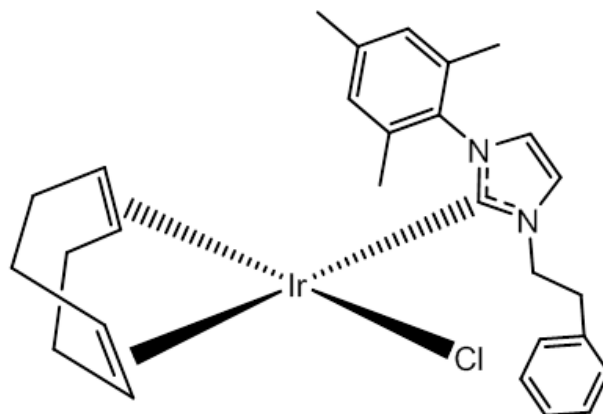
Figure 62: IMesCarBn Carbene [IrCl(IMesCarBn)(COD)] which was synthesised within the Duckett Group where IMes = 1,3-bis-(2,4,6-trimethylphenyl)-imidazol-2-ylidene

MesCarBn.BPH$_4$ (107 mg, 0.176 mmol) was dissolved partially in acetone (20 mL). To this suspension, K$_2$CO$_3$ (127 mg, 0.0917 mmol) was added and stirred for 15 minutes after which [Ir(COD)Cl]$_2$ (59.0mg, 0.0878 mmol) was added. A bright yellow mixture formed and was heated at reflux for 4 hours where the mixture appeared an orange-yellow colour. The mixture was then cooled down to room temperature and filtered through celite, then evaporated to give an orange-yellow residue. The residue was then dissolved in DCM (20 mL), where a white solid precipitates out. The mixture was filtered through celite and the solvent was evaporated giving an orange-yellow solid. The solid was then re-dissolved in hexane (30 mL) and heated, whilst stirring, in a water bath at 40 °C for *ca*. 15 minutes. The yellow solution was filtered and collected; with the previous two steps repeated twice more until a brown solid remains undissolved. All the yellow solutions collected were added together and reduced to approximately 10 mL in volume. The solution was placed in the freezer overnight to give [IrCl(MesCarBn)(COD)] as yellow-needle like crystals.

Yield: 73 %

6.4 Characterisation Data for Symmetric and Asymmetric *N*-Heterocyclic carbene complexes

6.4.1 IrCl(COD)(IXy)(1)
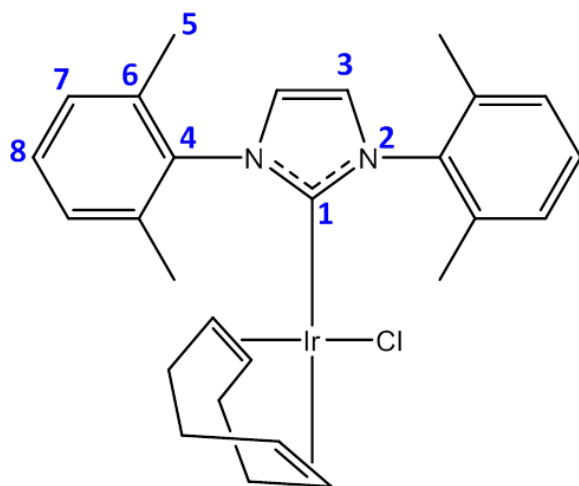
Figure 63: Labelled Schematic of 1

^{1}H NMR (400 MHz, CD$_2$Cl$_2$, 233 K): δ= 7.36 (t, 2**H**, **H**$_8$, J_{HH} = 7.58Hz), 7.24 (d, 4**H**, **H**$_7$, J_{HH} =7.55Hz), 7.07 (s, 2**H**, **H**$_3$), 3.97 (m, 2**H**, **CH**, COD), 2.98 (m, 2**H**, **CH**, COD), 2.40 (s, 6**H**, **H**$_5$), 2.26 (s, 6**H**, **CH**$_3$, **H**$_5$), 1.70 (m, 4**H**, **CH**$_2$, COD), 1.38-1.21 (m, 4**H**, **CH**$_2$, COD).

^{13}C NMR (101 MHz, CD$_2$Cl$_2$, 233 K): δ= 178.9 (N-**C**-N, **C**$_1$), 138.6 (N-**C**=C, **C**$_4$), 128.9 (C-**C**=C, **C**$_5$), 128.4, 127.7 (**C**=**C**-CH$_3$, **C**$_6$, **C**$_7$), 123.5 (**C**=**C**, 2**C**, **C**$_3$), 82.3 (2**C**H, COD), 52.3 (2**C**H, COD), 33.4, 28.9 (4**C**H$_2$, COD), 19.4, 18.5 (**C**H$_3$, **C**$_5$)

^{15}N NMR (41 MHz, CD$_3$OD, 263 K): δ= 192.2 (2**N**, **N**$_2$)

ESI$^+$-MS calculated M: C$_{27}$H$_{32}$N$_2$IrCl - 618.2 [M+CH$_3$CN]$^+$, 577.22 [M-Cl]$^+$
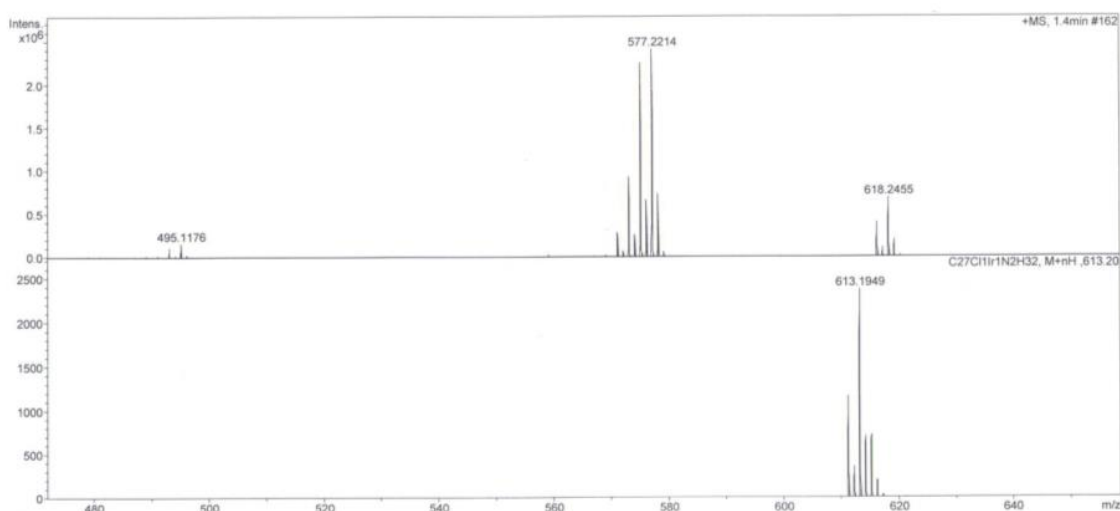
Figure 64: ESI Mass spectra of [IrCl(IXy)(COD)]

6.4.2 [Ir(COD)(IXy)(py)]Cl (1a)
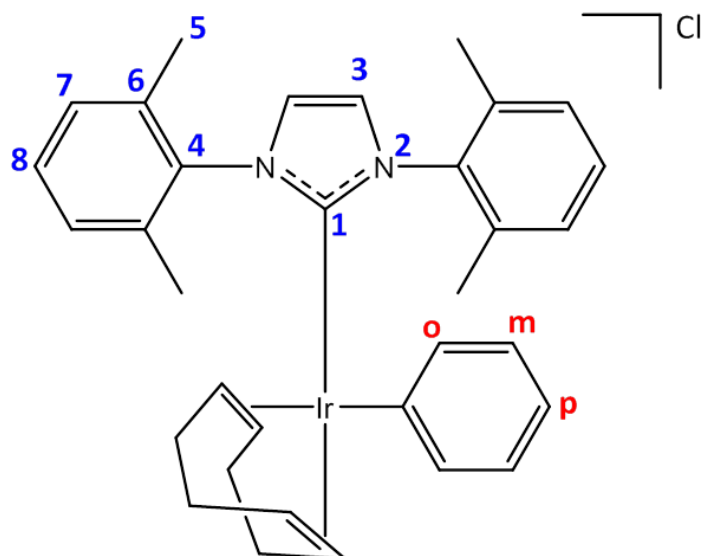
Figure 65: Labelled Schematic of 1a

^{1}H NMR (400 MHz, CD$_2$Cl$_2$, 294 K): δ= 7.88 (d, 2**H**, *o*-pyridine, J_{HH} = 4.98Hz), 7.82 (t, 1**H**, O-pyridine, J_{HH} = 7.64Hz) 7.49 (m, 4**H**, **H$_7$**) 7.46 (d, 2**H**, **H$_8$**, J_{HH} =7.37Hz) , 7.30 (t, 2**H**, *m*-pyridine, J_{HH} = 7.06Hz), 7.21 (d, 2**H**, **H$_3$**, J_{HH} =7.28Hz), 3.66 (t, 2H, J_{HH} = 2.84Hz, CH, COD), 3.31 (t, 2H, J_{HH} = 2.88Hz, CH, COD), 2.42 (s, 6**H**, **CH$_3$**, **H$_5$**), 2.10 – 1.59 (m, 8H, CH$_2$, COD), 1.92 (s, 6**H**, **CH$_3$**, **H$_5$**)

6.4.3 IrCl(H)$_2$(IXy)(COD) (1b)
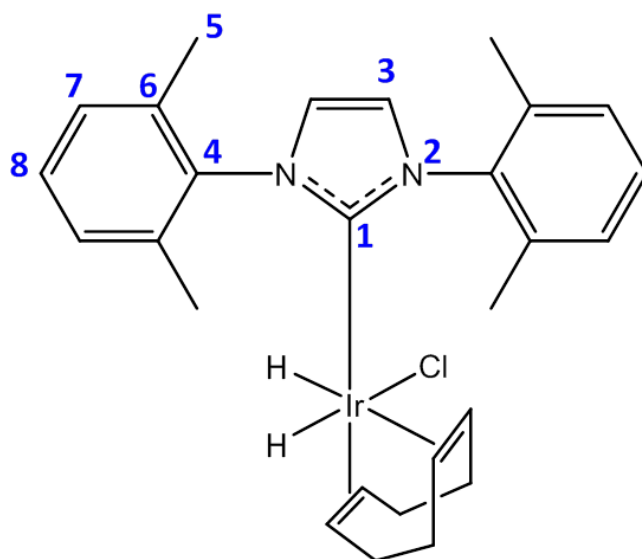
Figure 66: Labelled Schematic of 1b

^{1}H NMR (400 MHz, CD$_2$Cl$_2$, 233 K): 7.06 (m, 5**H**, **H**$_7$, **H**$_8$), 6.81 (s, 2**H**, **H**$_3$), 4.05 (2**H**, **H**C=C**H**, CH of COD), 3.05 (2**H**, **H**C=C**H**, CH of COD), 2.16 (12**H**, C**H**$_3$, **H**$_5$), 1.67, 1.33 (C**H**$_2$ of CD), −13.42 (1**H**, Hydride, trans to COD), −18.08 (1**H**, Hydride, trans to Cl).

6.4.4 [Ir(H)$_2$(IXy)(COD)(py)]Cl (1c)
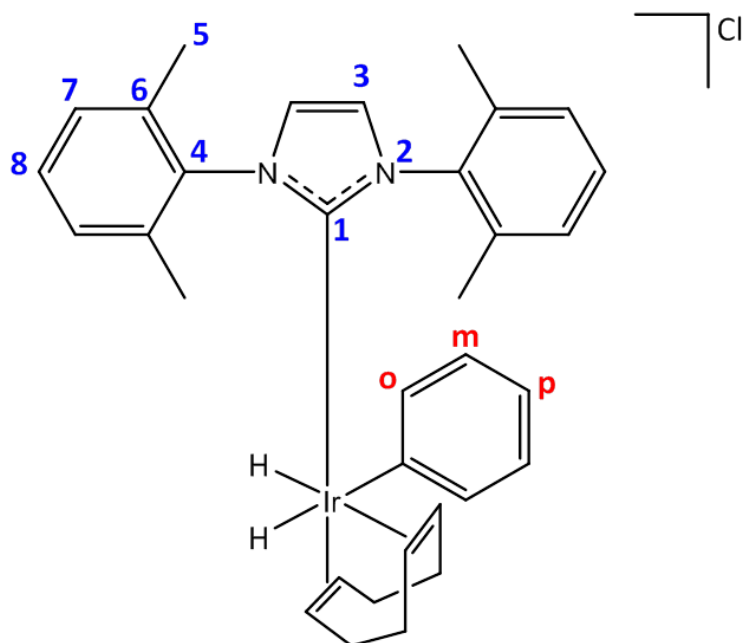
Figure 67: Labelled Schematic of 1c

^{1}H NMR (400 MHz, CD$_3$OD, 233 K): 8.39 (2**H**, *o*-py in equatorial position), 7.97 (1**H**, *p*-py in equatorial position), 7.45 (m, 5**H**, **H**$_7$, **H**$_8$), 7.27 (2**H**, *m*-py in equatorial position), 7.19 (s, 2**H**, **H**$_3$), 4.70 (2**H**, **H**C=C**H**, CH of COD), 4.24 (2**H**, **H**C=C**H**, CH of COD), 2.42 (12**H**, C**H**$_3$, **H**$_5$), 1.89, 1.31 (C**H**$_2$ of CD), −12.05 (1**H**, Hydride, trans to COD), −17.55 (1**H**, Hydride, trans to py).

6.4.5 [IrCl(H)₂(IXy)(py)₂] (1d)
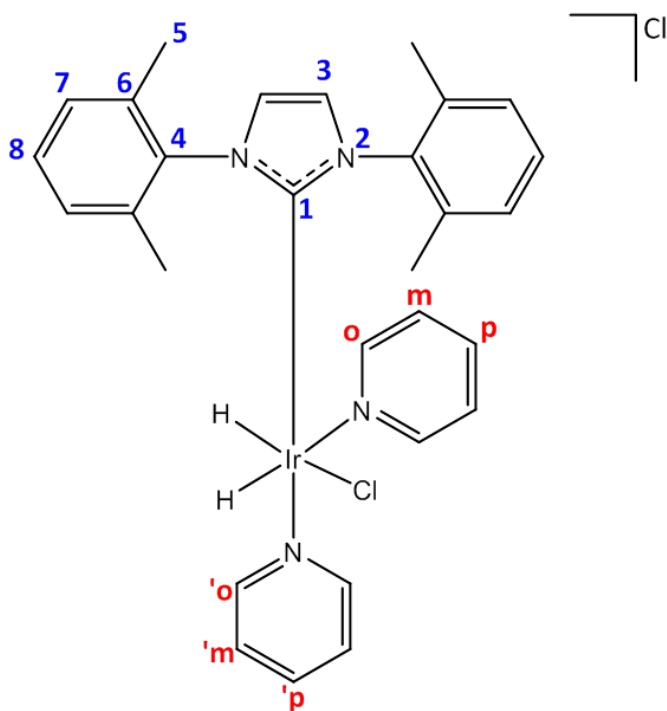
Figure 68: Labelled Schematic of 1d

¹H NMR (400 MHz, CD₂Cl₂, 294 K): δ 8.84 (br, 2**H**, '*o*-py in axial), 8.71 (d, 2**H**, *o*-py in equatorial), 7.42 (t, 1**H**, *p*-py in equatorial), 7.07 (t, 2**H**, '*m*-py in axial), 6.97 (m, 3**H**, 2**H**, **H**₈, CH-IXy overlap with 1**H**, '*p*-py in axial), 6.82 (m, 4**H**, 2**H**, *m*-py in equatorial overlap with 2**H**, **H**₃ ,C**H**-imidazolium), 5.60 (S, 4**H**, **H**₇ ,C**H**-IXy), 2.39 (s, 3**H**, CH₃-IXy, **H**₅), 2.28 (S, 9**H**, CH₃-IXy, **H**₅), -23.74 (s, 1H trans to py), -24.34 (s, 1H, trans to Cl).

6.4.6 [Ir(H)₂(IXy)(py)₃]Cl (2)
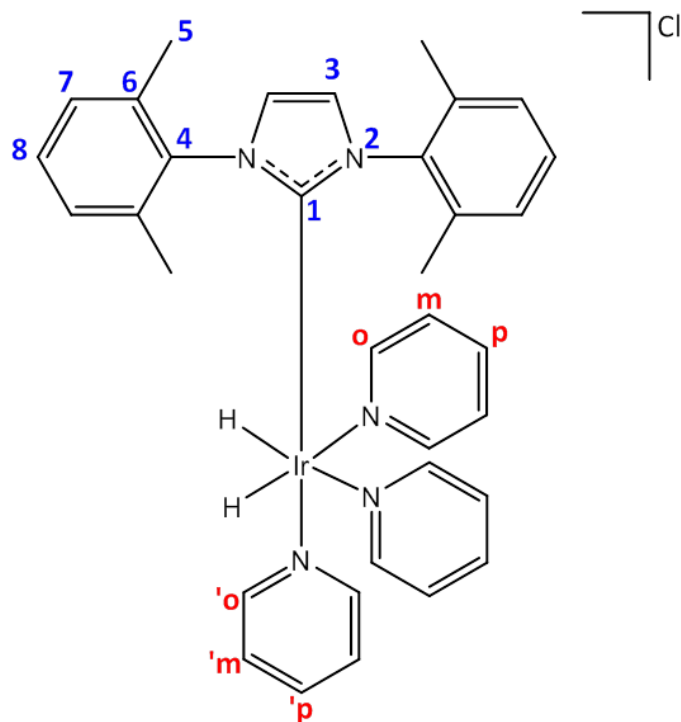
Figure 69: Labelled Schematic of 2

^{1}H NMR (400 MHz, CD₂Cl₂, 294K): 8.34 (4**H**, *o*-py in equatorial position), 8.06 (2**H**, '*o*-py in axial position), 7.74 (2**H**, *p*-py in equatorial position), 7.67 (1**H**, '*p*-py in equatorial position), 7.15 (m, 5**H**, **H**₇, **H**₈), 7.12 (4**H**, *m*-py in equatorial position), 6.91 (2**H**, '*m*-py in equatorial position), 6.85 (s, 2**H**, **H**₃), 2.15 (12**H**, C**H**₃, **H**₅), 22.73 (2**H**, Hydrides)

6.4.7 [IrCl(COD)(ITol)] (3)
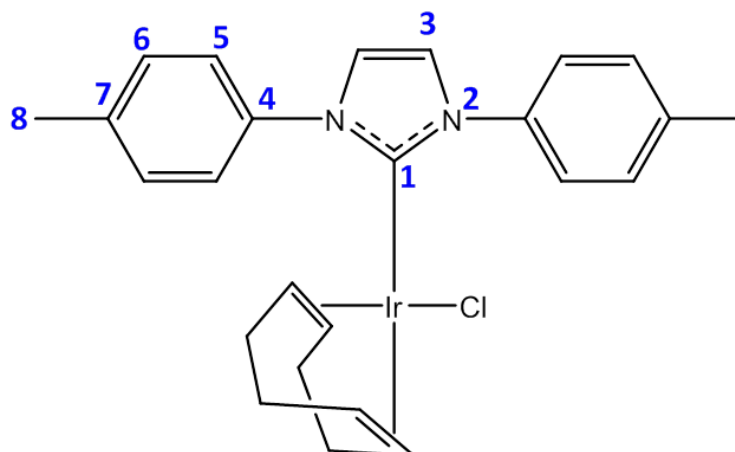
Figure 70: Labelled Schematic of 3

^{1}H NMR (400 MHz, CD$_2$Cl$_2$, 298 K): δ= 7.99 (d, 4**H**, CH, J_{HH}= 8.34Hz, **H$_6$**), 7.35 (d, 4**H**, J_{HH}= 8.27Hz, CH, **H$_5$**), 7.34 (s, 2**H**, **H$_3$**), 4.36 (m, 4**H**, CH, COD), 2.48 (S, 6**H**, CH$_3$, **H$_8$**), 1.82 (m, 2**H**, CH$_2$, COD), 1.45 (m, 4**H**, CH$_2$, COD), 1.22 (m, 2**H**, CH$_2$, COD).

^{13}C NMR (101 MHz, CD$_2$Cl$_2$, 298 K): δ= 180.80 (N=**C**=N, **C$_1$**), 137.95 (C-**C**=C, **C$_4$**), 129.02 (C-**C**=C, **C$_7$**) 128.60 (C-**C**=C, **C$_5$**), 125.34 (C=**C**-C, **C$_6$**), 121.40 (**C**=C, 2**C**, **C$_3$**), 82.42 (4**C**H, COD), 33.20 (4**C**H$_2$, COD), 29.50 (2**C**H$_2$, COD), 20.90 (2**C**H$_3$, 2**C**, **C$_8$**).

^{15}N NMR (51 MHz, CD$_2$Cl$_2$, 288 K): δ= 195.8 (2**N**, N$_2$)

ESI$^+$-MS calculated M: C$_{25}$H$_{29}$N$_2$IrCl − 585.16, 547.17[M-Cl]$^+$
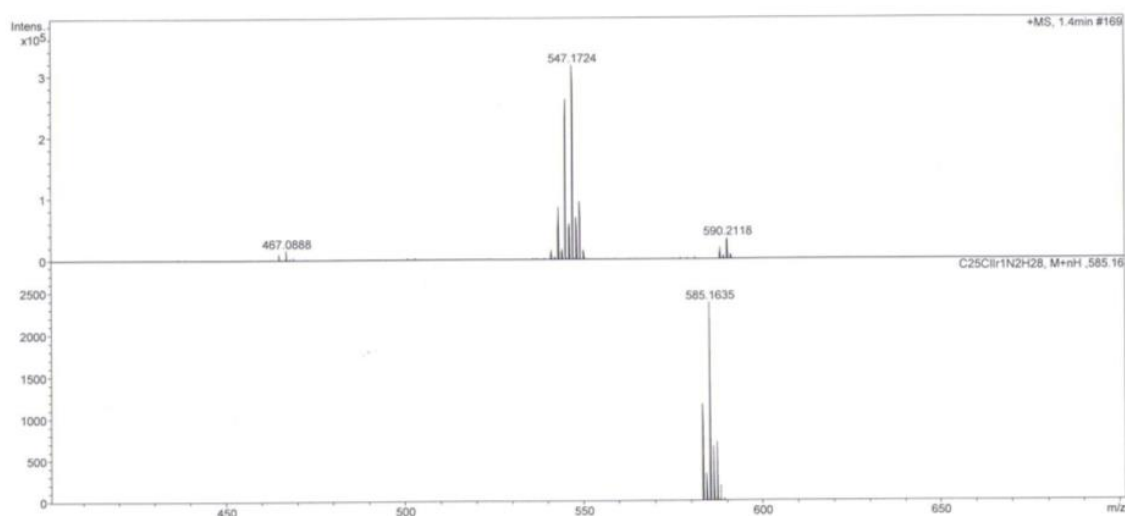
6.4.8 IrCl(H)(COD)(ITol) (3a)
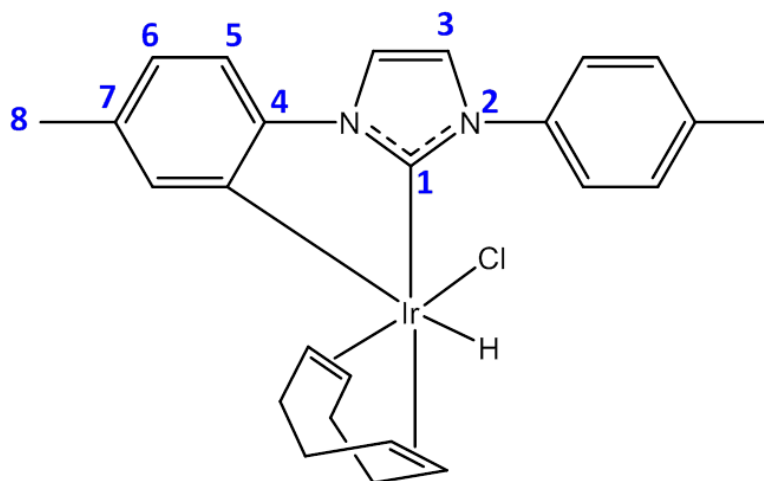
Figure 71: Labelled Schematic of 3a

^{1}H NMR (400 MHz, CD$_2$Cl$_2$, 298 K): δ= 7.80 (d, 4**H**, CH, J_{HH}= 8.34Hz, **H$_6$**), 7.35 (d, 4**H**, J_{HH}= 8.27Hz, CH, **H$_5$**), 7.34 (s, 2**H**, **H$_3$**), 4.42 (m, 4**H**, CH, COD), 2.33 (s, 6**H**, CH$_3$, **H$_8$**), 1.85 (m, 2**H**, CH$_2$, COD), 1.51 (m, 4**H**, CH$_2$, COD), 1.24 (m, 2**H**, CH$_2$, COD), -17.17 (hydride)

6.4.9 [IrCl(H$_2$)(ITol)(py)$_3$]Cl (4)
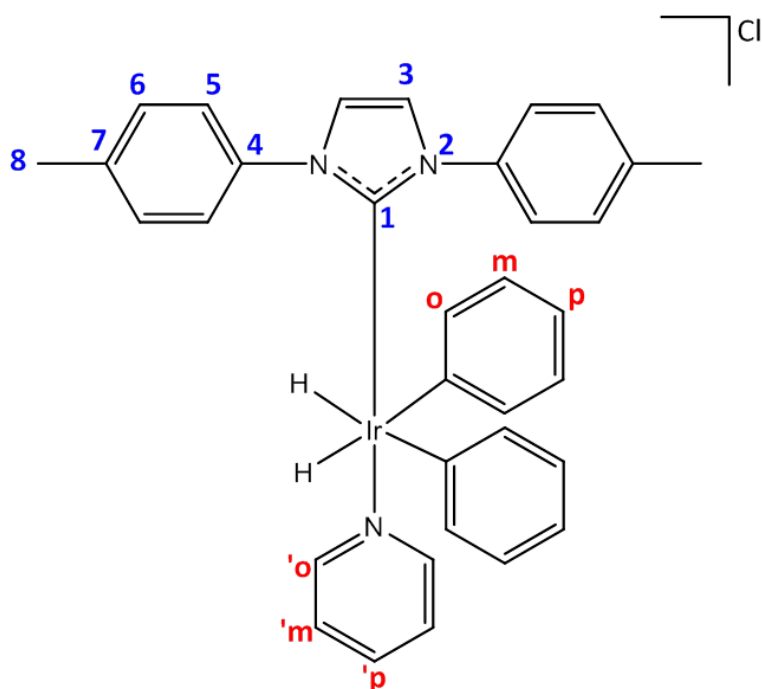
Figure 72: Labelled Schematic of 4

^{1}H NMR (400 MHz, CD$_3$OD, 298 K): 8.30 (4**H**, *o*-py in equatorial position), 7.80 (2**H**, '*o*-py in axial position), 7.47 (1**H**, *p*-py in equatorial position), 7.35 (d, 4**H**, CH, **H$_5$**), 7.34 (s, 2**H**, **H$_3$**), 7.00 (2**H**, '*p*-py in axial position), 6.69 (2**H**, '*m*-py in axial position), 6.48 (4**H**, *m*-py in equatorial position), 5.57 (s, 2**H**, **H$_6$**), 2.34 (12**H**, CH$_3$, **H$_5$**), −24.11 (2**H**, Hydrides)

6.4.10 [IrCl(COD)(tBuBIM)] (5)
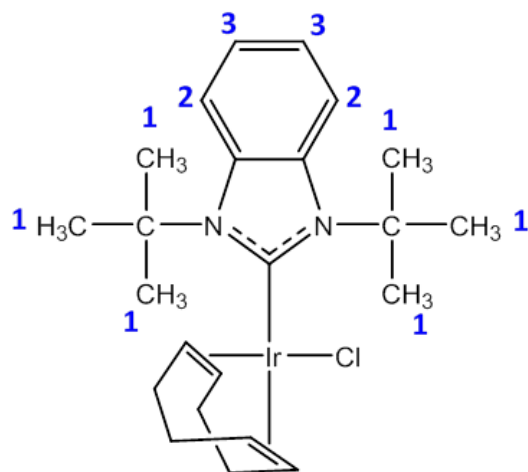
Figure 73: Labelled Schematic of 5

^{1}**H NMR (400MHz, CDCl$_3$, 298 K):** δ = 7.96 (dd, J = 3.2 Hz, 2H, H$_3$), 7.60 (dd, J = 3.2 Hz, 2H, H$_2$), 2.20 (m, 4H, COD-CH), 2.00 (s, 18H, CH$_3$, H$_1$),) 1.75-1.03 (m, 8H, COD-CH$_2$)

6.4.11 [IrCl(COD)(IMes)] (6)
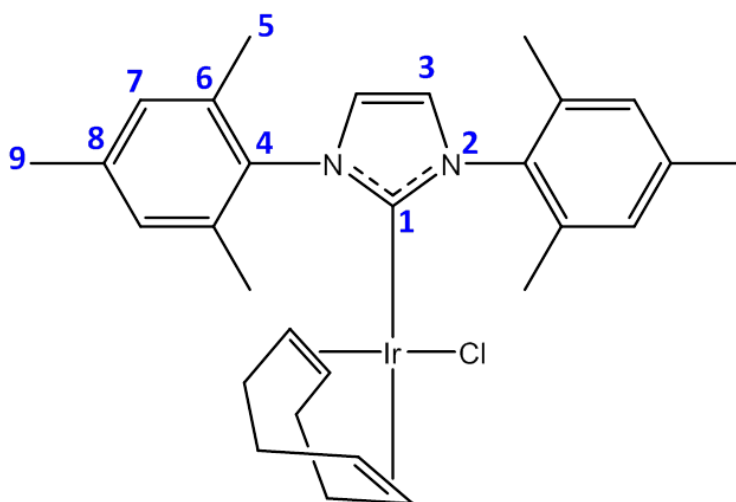
Figure 74: Labelled Schematic of 6

^{1}**H NMR (400 MHz, CD$_2$Cl$_2$, 298 K):** δ= 7.05 (*pseudo*-d, 4H,-CH, H$_7$), 7.02 (*pseudo*-d, 2H, H$_3$), 4.07 (m, 2H, =CH of COD), 3.04 (m, 2H, =CH of COD), 2.40 (s, 6H, CH$_3$, H$_9$), 2.34 (s, 6H, CH$_3$, H$_5$), 2.20 (s, 6H, CH$_3$, H$_5$), 2.10 – 1.59 (m, 8H, CH$_2$, COD), 1.92 (s, 6H, CH$_3$, H$_1$).

^{13}**C NMR (400 MHz, CD$_2$Cl$_2$, 294 K):** δ 180.50 (N-**C**-N, C$_1$), 138.61 (H$_3$C-**C**=C, C$_4$) 137.12 (N-**C**=C, C$_4$), 136.22 (C-**C**-CH$_3$, C$_6$, C$_8$), 134.63 (C-**C**-CH$_3$, C$_6$), 129.22, 128.19 (C=**C**-C, C$_7$), 123.48 (**C**=**C**, C$_3$), 81.80 (**C**=**C**, CH of COD), 51.50 (**C**=**C**, CH of COD), 33.40, 33.51, 33.35, 28.75 (**C**H$_2$ of COD), 20.74, 19.26, 17.98 (**C**H$_3$, C$_5$, C$_9$).

^{15}**N NMR (400MHz, CD$_2$Cl$_2$, 294K):** δ 191.60 (N$_2$).

6.4.12 [IrCl(H)₂(IMes)(3,5-Lutidine)₃]Cl (7)
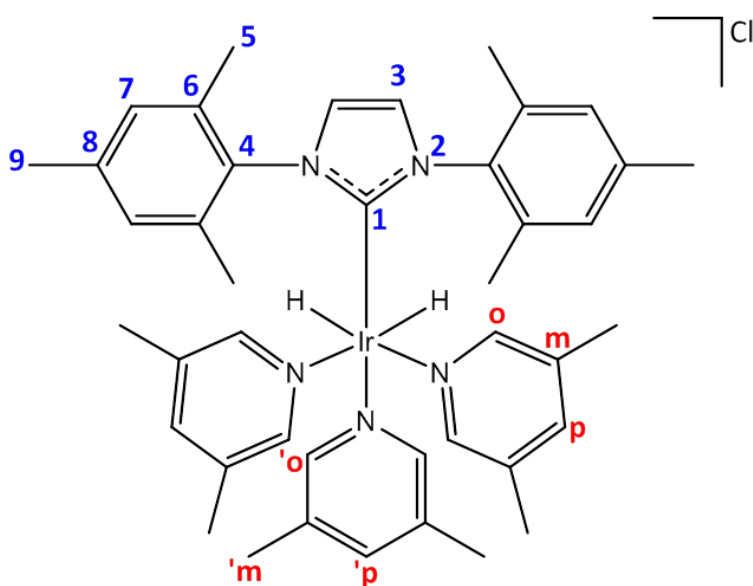
Figure 75: Labelled Schematic of 7

¹H NMR (400 MHz, CD₃OD, 298 K): δ 7.99 (s, 4**H**, *ortho*-C**H** lutidine in *equa.* position), 7.67 (s, 2**H**, '*o*-C**H** lutidine in *axial* position), 7.44 (s, **H**, '*p*-C**H** lutidine in *axial* position), 7.33 (s, 2**H**, *para*-C**H** lutidine in *equa* position), 7.30 (s, 2**H**, -C**H**=C**H**-, **H₃**), 6.73 (s, 4**H**, C**H**, **H₇**), 2.23 (s, 6**H**, C**H₃**, **H₉**), 2.19 (s, 12**H**, C**H₃**-lutidine in *axial* position), 2.10 (s, 6**H**, C**H₃**, **H₅**), 2.01 (s, 6**H**, C**H₃**-lutidine in *equa* position), −22.79 (s, 2**H**, hydrides)

¹³C NMR (500 MHz, CD₃OD, 298 K): δ 164.9 (**C**-carbene, **C₁**). 152.4 (*para*-**C**H, lutidine in *axial*), 152.3 (*para*-**C**H, lutidine in *equa*), 137.5 (*ortho*-**C**H, lutidine, *equa*), 135.9 (**C**(CH₃), lutidine, *axial*), 135.2 (**C**(CH₃), lutidine, *equa*), 134.9 (*ortho*-**C**H, lutidine, *axial*), 133.5, 135.1, 137.9 (**C**(CH₃)=CH, **C₄**, **C₈**), 128.11 (**C**H, **C₇**), 122.4 (-**C**H=CH-, **C₃**) , 17.4, 19.7 (**C**H₃, **C₅**, **C₉**), 16.7 (**C**H₃, lutidine *equa*), 16.1 (**C**H₃, lutidine *axial*)

6.4.13 [IrCl(COD)(PhCarCH$_3$) (8)
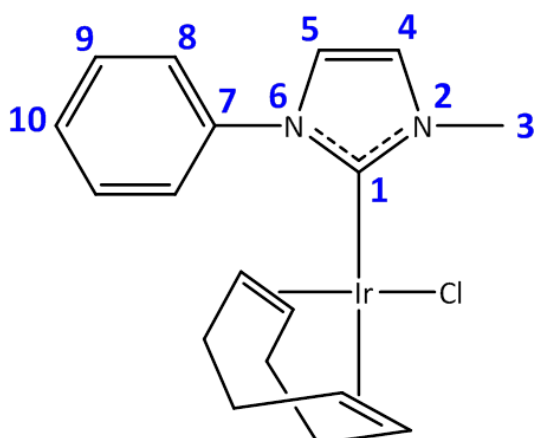
Figure 76: Labelled Schematic of 8

^{1}H NMR (400 MHz, CD$_2$Cl$_2$, 233 K): δ 8.03 (d , J_{H-H}=7.27 Hz, 2**H**, **H**$_8$), 7.51 (m, 2**H**, **H**$_9$), 7.45 (m, 1H. **H**$_{10}$), 7.41 (m, 4**H**, **H**$_7$, **H**$_8$), 7.23 (*pseudo*-s, 1**H**, **H**$_5$, **H**$_4$), 7.08 (*pseudo*-s, 1**H**, **H**$_5$, **H**$_4$), 4.56 (m, 1**H**, =C**H** of COD), 4.32 (m, 1**H**, =C**H** of COD), 2.91 (m, 1**H**, =C**H** of COD), 2.16 (m, 3**H**, C**H**$_2$ of COD), 1.89 (m, 1**H**, =C**H** of COD), 1.71 (3**H**, C**H**$_3$, **H**$_3$), 1.61 (m, 2**H**, C**H**$_2$ of COD), 1.52 (m, 1**H**, C**H**$_2$ of COD), 1.36-1.15 (m, 2**H**, C**H**$_2$ of COD).

^{13}C NMR (101 MHz, CD$_2$Cl$_2$, 298K): δ 179.70 (Im C=C, **C**$_4$, **C**$_5$), 128.70 (C=**C**-C, C$_9$), (**C**=C-C, C$_{10}$), 124.71 (C-**C**=C, **C**$_8$), 122.65, 121.02 (**C**=C, **C**$_4$, **C**$_5$), 83.29, 82.78 (=**C**H, CH of COD), 51.76, 51.75, 33.96, 29.31 (**C**H$_2$, CH$_2$ of COD overlap with CH$_3$, **C**$_3$)

^{15}N NMR (41 MHz, CD$_2$Cl$_2$, 294 K): δ 195.00, 176.36 (**N**$_2$, **N**$_6$).

6.4.14 [Ir(H)₂(PhCarCH₃)(3,5-Lutidine)₃]Cl (9)
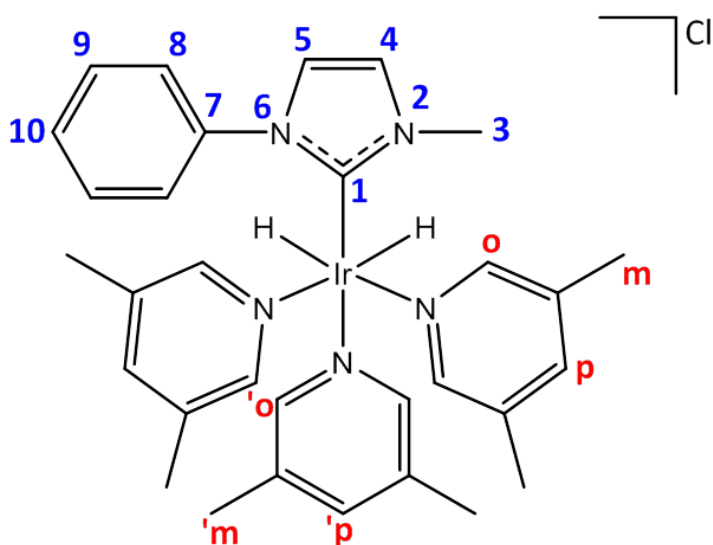
Figure 77: Labelled Schematic of 9

^{1}H NMR (400 MHz, CD₃OD, 298 K): δ 8.03 (s, 4**H**, *o*-C**H** lutidine in equa position), 7.64 (s, 2**H**, *'o*-C**H** lutidine in axial), 7.54 (s, 2**H**, *p*-C**H** lutidine in equa position), 7.16 (s, **H**, **'***p*-C**H** lutidine in axial position) 7.11 (s, 2**H**, C**H**, J_{HH}=1.95 Hz, **H**$_4$, **H**$_5$), 6.83 (m, 4H, **H**$_8$, **H**$_9$), 7.10 (d , J_{HH}=7.35 Hz, **H**$_{10}$), 2.29 (s, 6H, *'m* C**H**₃-lutidine in equa position), 2.22 (s, 3H, C**H**₃, **H**$_3$), 2.20 (s, 12H, *m* C**H**₃-lutidine in axial position), -22.24 (s, 2H, hydrides).

^{13}C NMR (126 MHz, CD₃OD, 303 K): δ 154.9 (**C**-carbene, **C**$_1$). 149.3 (**C**, *o*-CH of lutidine in equa position), 148.3 (**C**, *'p*-CH of lutidine in axial position), 138.6 (**C**=**C**, **C**$_4$, **C**$_5$), 137.9 (**C**, *p*-CH, lutidine of equatorial position), 135.9 (**C**-CH₃, lutidine, axial), 135.2 (**C**-CH₃, lutidine, equa), 133.0 (**C**, *'o*-CH, lutidine in axial position), 121.80, 121.30 (C=**C**-**C**=C, **C**$_8$, **C**$_9$), 109.8 (para-CH, **C**$_{10}$), 17.44, 16.52, (*m*-**C**H₃, lutidine of equa and axial overlaps with **C**H₃, **C**$_3$).

6.4.15 [IrCl(COD)(MesCarCH₃)] (10)
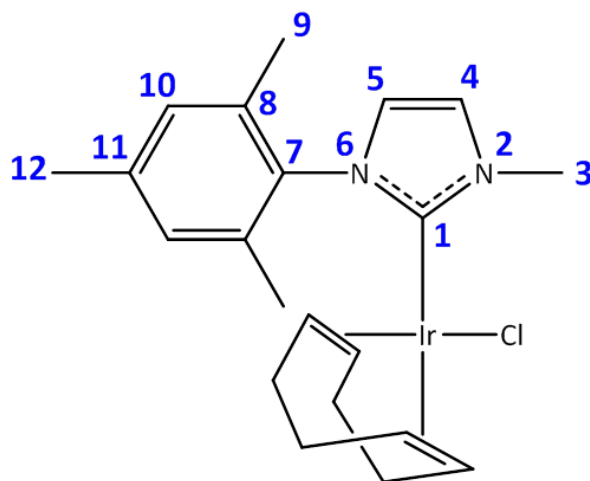
Figure 78: Labelled Schematic of 10

^{1}H NMR (500 MHz, CD$_3$OD, 243 K): δ 7.10 (d, 1**H**, J_{H-H}=1.75 Hz, Im-**H**$_5$), 7.04 (s, 1**H**, **H**$_{10}$), 6.95 (s, 1**H**, **H**$_{10}$), 6.97 (d, J_{H-H} = 1.75 Hz, 1**H**, Im-**H**$_4$), 4.30 (td, J_{H-H} = 7.65 Hz, J_{H-H} = 3.23 Hz, 1**H**, =C**H** of COD), 4.21 (td, J_{H-H} = 7.32 Hz, J_{H-H} = 3.09 Hz, 1**H**, =C**H** of COD), 3.15 (td, J_{H-H} = 7.03 Hz, J_{H-H} = 2.03 Hz, J_{H-H} = 1**H**, =C**H** of COD), 2.72 (td, J_{H-H} = 7.32 Hz, J_{H-H} = 3.50 Hz, 1**H**, =C**H** of COD), 2.36 (s, 3**H**, **H**$_9$), 2.26 (s, 3**H**, **H**$_9$), 1.97 (m, 1**H**, C**H**$_2$ of COD), 2.15 (m, 1**H**, C**H**$_2$ of COD), 2.05 (m, 1**H**, C**H**$_2$ of COD), 1.90 (s, 3H, **H**$_{12}$), 1.77 (m, 1**H**, C**H**$_2$ of COD), 1.70 (s, 3**H**, **H**$_3$), 1.54 (m, 2**H**, C**H**$_2$ of COD), 1.43 (m, 2**H**, C**H**$_2$ of COD), 1.19 (m, 1**H**, C**H**$_2$ of COD)

^{13}C NMR (101 MHz, CD$_2$Cl$_2$, 298K): δ 180.2 (Im-**C**$_1$), 138.7 (**C**$_9$), 136.6 (**C**$_9$), 135.8 (**C**$_{11}$), 134.3 (**C**$_{12}$), 129.1(**C**$_{11}$), 129.1 (**C**$_8$ overlaps with -CH meta of Mes), 128.0 (**C**$_{10}$), 128.0 (**C**$_8$ overlaps with meta-CH of Mes)**,** 122.7 (**C**$_4$), 122.0 (**C**$_5$), 82.6 (=**C**H of COD), 82.6 (=**C**H of COD), 51.2 (=**C**H of COD), 50.3 (=**C**H of COD), 17.53 (4**C**H$_2$ of COD)

^{15}N NMR (41 MHz, CD$_2$Cl$_2$, 298 K): δ= 188.9 (1N, N$_6$), 176.5 (1N, N$_2$)

6.4.16 [Ir(COD)(MesCarCH₃)(3,5-Lutidine)]Cl (10a)
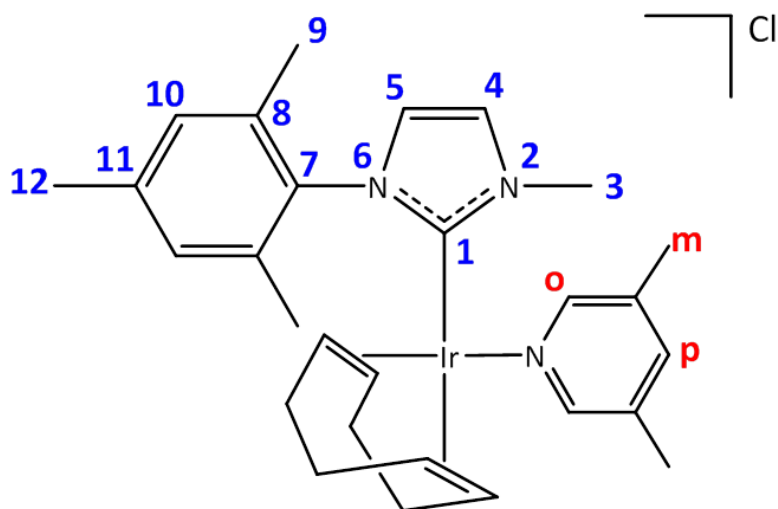
Figure 79: Labelled Schematic of 10a

^{1}H NMR (400 MHz, CD₃OD, 298 K): 7.99(s, 4**H**, *ortho*-C**H** lutidine in *equa.* position), 7.50 (s, 2**H**, *para*-C**H** lutidine in *equa* position), 7.30 (d, H, =C**H**-CH₅, imidazolium, J_{HH}=1.95 Hz, **H**₅), 6.88 (d, **H**, =C**H**, imidazolium, J_{HH}=1.95 Hz, **H**₄), 3.15 (3**H**, C**H**₃, **H**₁₂), 6.69 (s, C**H**, **H**₁₀), 4.41 (2**H**, C**H** of COD), 3.82 (m, 2**H**, C**H** of COD), 2.50 (3**H**, C**H**₃, **H**₉), 2.43 (3**H**, C**H**₃, **H**₉) 2.20 (s, 12**H**, *meta*-C**H**₃-lutidine in *equa* position), 2.11 (s, 3**H**, C**H**₃, **H**₄), 1.68 (3**H**, C**H**₃, **H**₃) 1.40 – 1.30 (m, 8**H**, C**H**₂ of COD)

6.4.17 [IrCl(H)$_2$(MesCarCH$_3$)(3,5-Lutidine)$_3$]Cl (11)
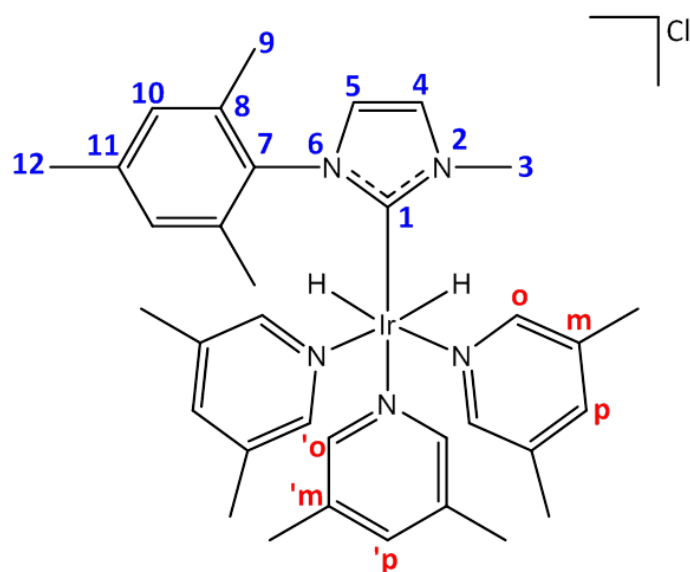
Figure 80: Labelled Schematic of 11

^{1}H NMR (400 MHz, CD$_3$OD, 298 K): δ 7.99(s, 4H, *o*-CH lutidine in *equv.* position), 7.88 (s, 2H, '*o*-CH lutidine in *axial* position), 7.50 (s, 2H, *p*-CH lutidine in *equa* position), 7.49 (s, H, '*p*-CH lutidine in *axial* position), 7.30 (d, H, =C**H**-CH$_3$, imidazolium, J$_{HH}$=1.95 Hz, **H$_4$**), 6.88 (d, H, -C**H**=, imidazolium, J$_{HH}$=1.95 Hz, **H$_5$**), 6.69 (s, C**H**, **H$_{10}$**), 3.18 (3**H**, CH$_3$, **H$_{12}$**), 2.23 (s, 6**H**, CH$_3$, **H$_9$**), 2.20 (s, 12**H**, *m*-CH$_3$-lutidine in *equa* position), 2.11 (s, 3**H**, CH$_3$, **H$_3$**), 2.01 (s, 6**H**, '*m*-CH$_3$-lutidine in *axial* position), -22.35 (s, 2**H**, hydrides, Ir-**H**).

^{13}C NMR (500 MHz, CD$_3$OD, 303 K): δ 158.9 (C-carbene, **C$_1$**), 152.7 ('*p*-CH, lutidine in axial), 151.2 (*p*-CH, lutidine in equa), 138.8 (*o*-CH, lutidine in equa), 135.9 (**C**(CH$_3$), lutidine, axial), 135.2 (**C**(CH$_3$), lutidine in equa), 137.9 ('*o*-CH, lutidine in axial), 122.0,128.4 (=C**H**-CH$_3$, C$_2$, C$_3$), 37.0 (CH$_3$, **C$_9$**), 19.6, 19.7 (CH$_3$, **C$_3$**), 17.2 (**C**H$_3$, lutidine in equa), 16.7 (**C**H$_3$, lutidine in axial).

6.4.18 IrCl(COD)(MesCarBenzyl) (12)
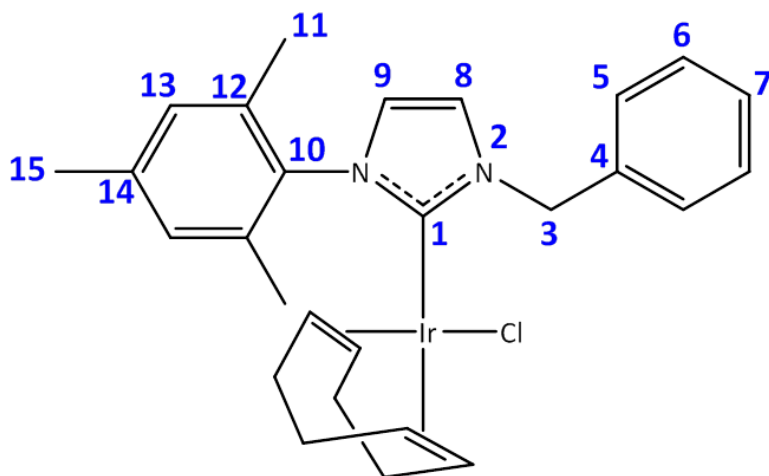
Figure 81: Labelled Schematic of 12

^{1}H NMR (500 MHz, CD$_3$OD, 298 K): δ 7.41 (m, 4**H**, **H$_5$**, **H$_6$**), 7.35 (m, 1**H**, **H$_7$**), 7.04 (s, 1**H**, **H$_{13}$**), 6.97 (d, $^3J_{H-H}$ = 1.98 Hz, 1**H**, Im-**H$_8$**), 6.94 (s, 1**H**, **H$_{13}$**), 6.80 (d, $^3J_{H-H}$ = 1.98 Hz, 1**H**, Im-**H$_9$**), 6.10 (d, $^2J_{H-H}$ = 15.1 Hz, 1**H**, **H$_3$**), 5.57 (d, $^2J_{H-H}$ = 15.1 Hz, 1**H**, **H$_3$**), 4.37 (dt, $^3J_{H-H}$ = 11.8 Hz, $^3J_{H-H}$ = 3.94 Hz, 1**H**, =C**H** of COD), 4.30 (dt, $^3J_{H-H}$ = 11.8 Hz, $^3J_{H-H}$ = 3.94 Hz, 1**H**, =C**H** of COD), 2.96 (dt, $^3J_{H-H}$ = 11.8 Hz, $^3J_{H-H}$ = 3.94 Hz, 1**H**, =C**H** of COD), 2.74 (dt, $^3J_{H-H}$ = 11.8 Hz, $^3J_{H-H}$ = 3.94 Hz, 1**H**, =C**H** of COD), 2.36 (s, 3**H**, **H$_{15}$**), 2.32 (s, 3**H**, **H$_{11}$**), 1.97 (m, 1**H**, C**H$_2$** of COD), 1.92 (s, 3**H**, **H$_{11}$**), 1.89 (m, 1**H**, C**H$_2$** of COD), 1.77 (m, 1**H**, C**H$_2$** of COD), 1.51 (m, 1**H**, C**H$_2$** of COD), 1.41 (m, 3**H**, C**H$_2$** of COD), 1.18 (m, 1**H**, C**H$_2$** of COD).

^{13}C NMR (126 MHz, CD$_3$OD, , 298 K): δ 180.9 (Im-**C$_1$**), 139.1 (**C$_{14}$**), 137.6 (**C$_4$**), 137.0 (**C$_{12}$**), 136.3 (**C$_{10}$**), 134.9 (**C$_{12}$**), 129.6 (**C$_{13}$**), 129.1 (**C$_5$**), 128.5 (meta-CH of Mes overlapped with meta-CH of phenyl ring, **C$_6$**, **C$_{13}$**), 128.2 (**C$_7$**), 123.7 (Im-**C$_9$**), 121.2 (Im-**C$_8$**), 83.5 (=**C**H of COD), 83.1 (=**C**H of COD), 55.2 (**C**H$_2$, **C$_3$**), 52.6 (=**C**H of COD), 51.5 (=**C**H of COD), 34.5 (**C**H$_2$ of COD), 33.0 (**C**H$_2$ of COD), 29.7 (**C**H$_2$ of COD), 29.1 (**C**H2 of COD), 21.2 (**C$_{15}$**), 19.6 (**C$_{11}$**), 18.0 (**C$_{11}$**).

^{15}N NMR (41 MHz, CD$_2$Cl$_2$, 298 K): δ 189.0 (2N, N$_2$)

ESI$^+$-MS calculated M: C$_{25}$H$_{32}$N$_2$IrCl – 577.22 [M-NaH]$^+$
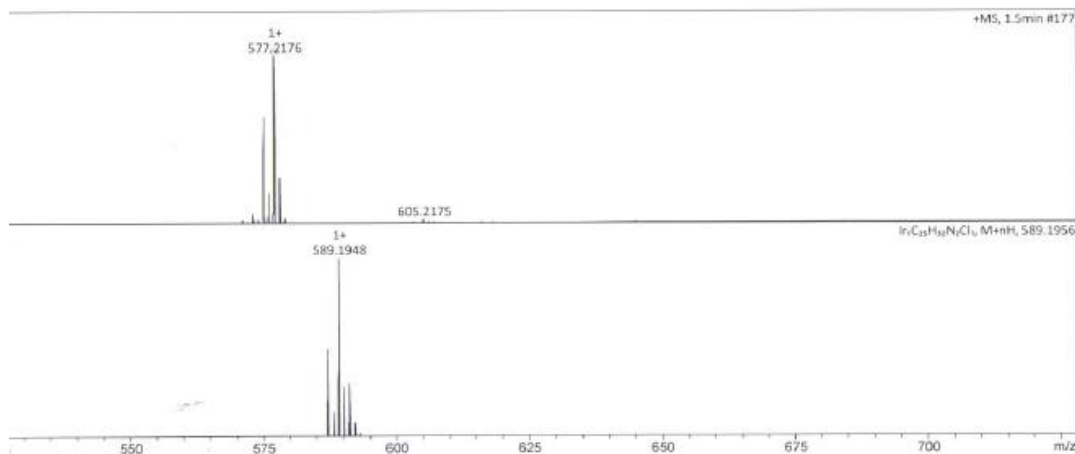
6.4.19 [Ir(COD)(MesCarBenzyl)(3,5-Lutidine)] Cl (12a)
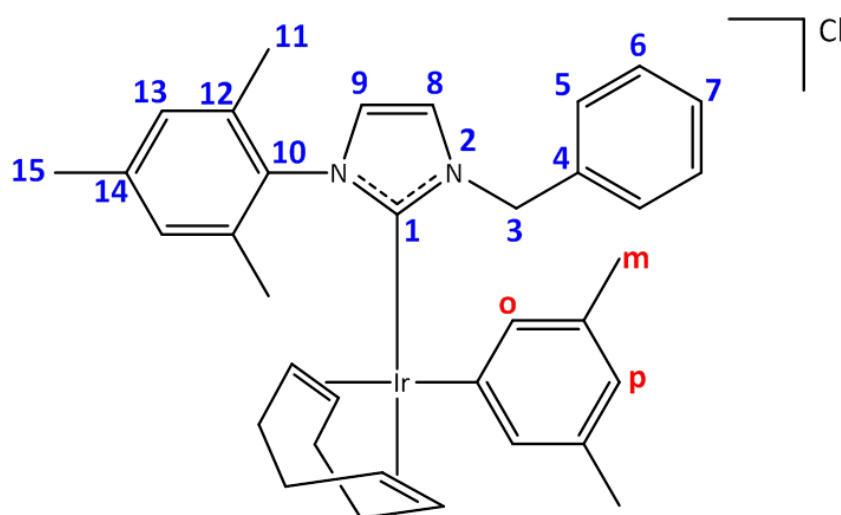
Figure 82: Labelled Schematic of 12a

^{1}H NMR (400 MHz, CD$_3$OD, 298 K): δ 7.99 (s, 4**H**, *o*-C**H** lutidine in *equa* position), 7.82 (s, 2**H**, '*o*-C**H** lutidine in *axial* position), 7.48 (s, 2**H**, *p*-C**H** lutidine in *equa* position), 7.47 (s, 1**H**, '*p*-C**H** lutidine in *axial* position), 7.30 (s, 2**H**, **H**$_5$, **H**$_6$), 7.17 (*pseudo*-d, 1**H**, Im-**H**$_8$), 7.04 (s, 1**H**, **H**$_7$), 6.94 (*pseudo*-d, 1**H**, Im-**H**$_9$), 6.74 (s, 2**H**, **H**$_{13}$), 5.00 (s, 2**H**, C**H**$_2$, **H**$_3$), 2.26 (s, 3**H**, **H**$_{15}$), 2.17 (s, 3**H**, *m*-C**H** lutidine in *equa* position), 2.08 (s, 3**H**, '*m*-C**H** lutidine in *axial* position), 2.07 (s, 3**H**, **H**$_{11}$), −22.27 (s, 2**H**, hydrides)

6.4.20 [Ir(H₂)(MesCarBenzyl)(3,5-Lutidine)₃]Cl (13)
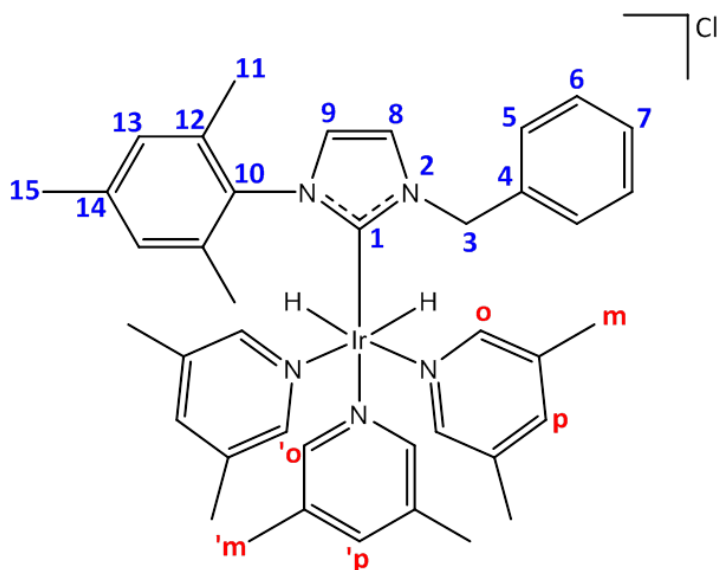
Figure 83: Labelled Schematic of 13

¹H NMR (400 MHz, CD₃OD, 298 K): δ 7.99 (s, 4**H**, *o*-C**H** lutidine in *equa* position), 7.82 (s, 2**H**, '*o*-C**H** lutidine in *axial* position), 7.48 (s, 2**H**, *p*-C**H** lutidine in *equa* position), 7.47 (s, 1**H**, '*p*-C**H** lutidine in *axial* position), 7.30 (s, 2**H**, **H₅**, **H₆**), 7.17 (*pseudo*-d, 1**H**, Im-**H₈**), 7.04 (s, 1**H**, **H₇**), 6.94 (*pseudo*-d, 1**H**, Im-**H₉**), 6.74 (s, 2**H**, **H₁₃**), 5.00 (s, 2**H**, C**H₂**, **H₃**),   2.26 (s, 3**H**, **H₁₅**), 2.17 (s, 3**H**, *m*-C**H** lutidine in *equa* position), 2.08 (s, 3**H**, '*m*-C**H** lutidine in *axial* position), 2.07 (s, 3**H**, **H₁₁**), −22.27 (s, 2**H**, hydrides)

¹³C NMR (101 MHz, CD₃OD, 298 K): δ 187.5 (carbene, **C₁**), 151.15 (4**C**, *o*-**C**H of lutidine in *equa*), 144.50 (2**C**, '*o*-**C**H of lutidine in *equa*), 138.98 (**C₁₄**), 137.97 (3**C**, *p*-**C**H and '*p*-CH of lutidine in *equa and axial position overlap*), 137.97 (**C₁₂**), 137.6 (**C₄**), 136.3 (**C₁₀**), 128.40 (Im-**C₉** overlapped with **C₇**) 129.1 (**C₅**), 128.20 (**C₁₃**) 128.01 (**C₅**, **C₆**), 126.88 (Im-**C₈**), 55.2 (C**H₂**, **C₃**), 19.73 (4**C**, *m*-**C**H of lutidine in *equa* overlap with **C₁₅**, **C₁₁**), 16.67 (2**C**, *m*-**C**H of lutidine in *equa* overlap with **C₁₅**, **C₁₁**)

6.4.21 IrCl(COD)(MesCarHomoBenzyl) (14)
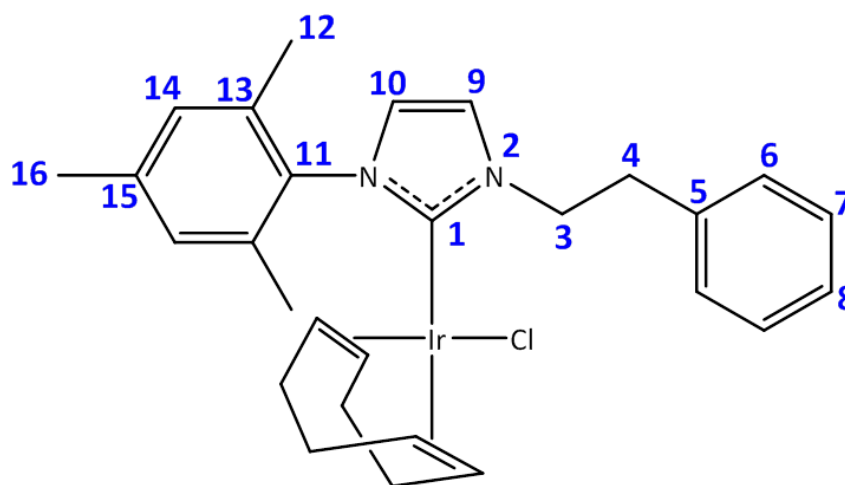
Figure 84: Labelled Schematic of 14

^{1}H NMR (500 MHz, CD₃OD, 298 K): δ 7.28 (m, 5**H**, **H**₆, **H**₇, **H**₈), 7.03 (s, 1**H**, **H**₁₄), 6.94 (d, $^3J_{\text{H-H}}$ = 1.92 Hz, 1**H**, Im-**H**₉), 6.92 (s, 1**H**, **H**₁₄), 6.74 (d, $^3J_{\text{H-H}}$ = 1.92 Hz, 1**H**, Im-**H**₁₀), 5.13 (dt, $^2J_{\text{H-H}}$ = 13.5 Hz, $^3J_{\text{H-H}}$ = 7.68 Hz, 1**H**, **H**₇), 4.46 (dt, $^2J_{\text{H-H}}$ = 13.5 Hz, $^3J_{\text{H-H}}$ = 7.68 Hz, 1**H**, **H**₃), 4.38 (dt, $^3J_{\text{H-H}}$ = 11.6 Hz, $^3J_{\text{H-H}}$ = 3.56 Hz, 1**H**, =C**H** of COD), 4.29 (dt, $^3J_{\text{H-H}}$ = 11.6 Hz, $^3J_{\text{H-H}}$ = 3.56 Hz, 1**H**, =C**H** of COD), 3.30 (t, $^3J_{\text{H-H}}$ = 7.40 Hz, 2**H**, **H**₄), 2.79 (dt, $^3J_{\text{H-H}}$ = 11.6 Hz, $^3J_{\text{H-H}}$ = 3.56 Hz, 1**H**, =C**H** of COD), 2.68 (dt, $^3J_{\text{H-H}}$ = 11.6 Hz, $^3J_{\text{H-H}}$ = 3.56 Hz, 1**H**, =C**H** of COD), 2.35 (s, 3**H**, **H**₁₆), 2.28 (s, 3**H**, **H**₁₂), 2.05 (m, 2**H**, C**H**₂ of COD), 1.87 (s, 3**H**, **H**₁₂), 1.76 (m, 1**H**, C**H**₂ of COD), 1.48 (m, 3**H**, C**H**₂ of COD), 1.36 (m, 1**H**, C**H**₂ of COD), 1.18 (m, 1**H**, C**H**₂ of COD).

^{13}C NMR (101 MHz, CD₃OD, 298 K): δ 180.1 (Im-**C**₁₆), 139.1 (**C**₁₅), 139.0 (**C**₅), 137.0 (**C**₁₃), 136.4 (**C**₁₁), 135.0 (**C**₁₃), 129.6 (**C**₁₄), 129.4 (**C**₇), 129.0 (**C**₆), 128.4 (**C**₁₄), 127.0 (**C**₈), 123.2 (Im-**C**₁₀), 121.1 (Im-**C**₉), 83.2 (=**C**H of COD), 82.7 (=**C**H of COD), 53.1 (**C**₃), 52.2 (=**C**H of COD), 51.7 (=**C**H of COD), 37.5 (**C**₄), 34.6 (**C**H₂ of COD), 33.1 (**C**H₂ of COD), 29.6 (**C**H₂ of COD), 29.3 (**C**H₂ of COD), 21.2 (**C**₁₆), 19.6 (**C**₁₂), 17.9 (**C**₁₂).

^{15}N NMR (CD₃OD, 41 MHz, 298 K): δ= 188.9 (1**N**, **N**₂, **N**₁)

ESI⁺-MS calculated M: $C_{27}H_{32}N_2IrCl$ – 591.24 [M-Cl]⁺
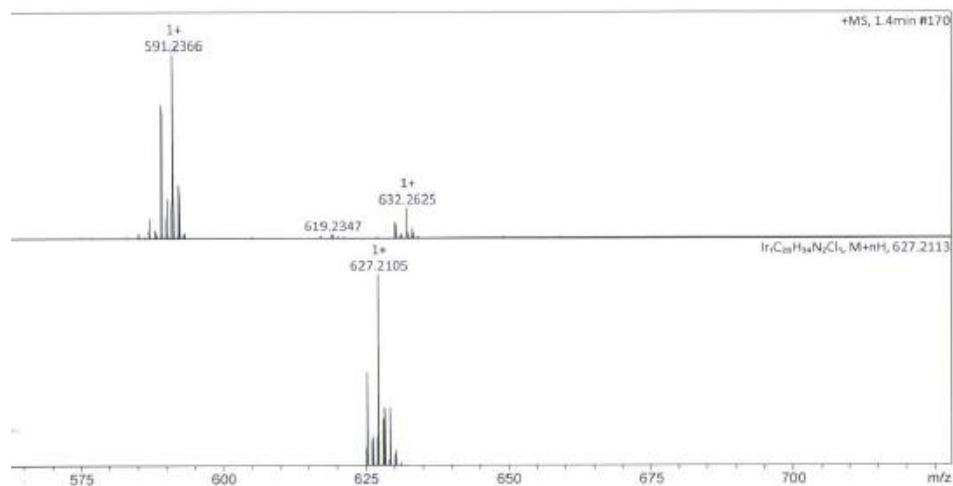
## 6.4.22 [Ir(H)₂(MesCarHomoBenzyl)(3,5-Lutidine)₃]Cl (15)
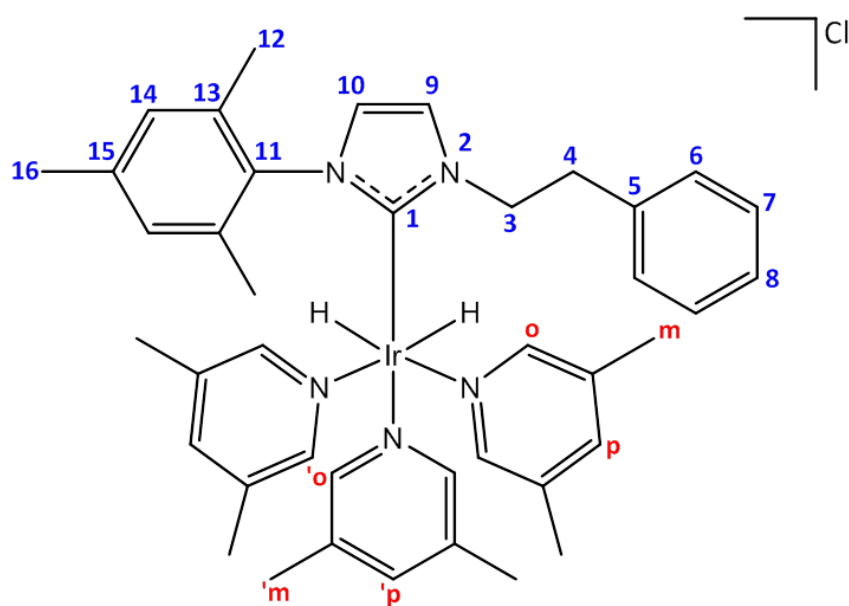
Figure 85: Labelled Schematic of 15

¹H NMR (400 MHz, CD₃OD, 298 K): δ 8.00 (s, 4H, *ortho*-CH lutidine in *equa.* position), 7.88 (s, 2H, *ortho*-CH lutidine in *axial* position), 7.51 (s, 2H, *para*-CH lutidine in *equa* position), 7.47 (s, H, *para*-CH lutidine in *axial* position), 7.31 (d, H, =CH-CH₃, imidazolium, J$_{HH}$=1.95 Hz, H₉, H₁₀), 7.24 (d, 2H, CH-*meta* on Benz, J$_{HH}$=7.24 Hz, H₇), 7.19 (1H, CH-*para* on Benz, J$_{HH}$=7.29 Hz, H₈), 7.03 (d, 2H, CH-*ortho* on Benz, J$_{HH}$=7.35Hz, H₆), 6.88 (d, 1H, -C*H*=, imidazolium, J$_{HH}$=1.95 Hz, H₉, H₁₀), 6.69 (s, 2**H**, H₁₄), 3.74, 2.96 (t, 4**H**, CH₂, **H₃**, H₄), 2.23 (s, 3H, C**H₃**, **H₁₆**), 2.17 (s, 12**H**, CH₃-lutidine in *equa* position), 2.11 (s, 6**H**, CH₃-lutidine in *axial* position), 2.02 (s, 6**H**, CH₃, Mes, H₁₂), −22.38 (s, 2**H**, hydrides).

^{13}C NMR (500 MHz, CD$_3$OD, 298 K): 158.9 (C-carbene, **C$_1$**), 152.8 (*'p*-**C**H, lutidine in *axial*), 151.1 (*p*-**C**H, lutidine in *equa*), 138.8 (*o*-**C**H, lutidine, *equa*), 135.9 (**C**(CH$_3$), lutidine, *axial*), 135.2 (**C**(CH$_3$), lutidine, *equa*), 134.9 (*'o*-**C**H, lutidine, *axial*), 128. 3 (**C**H, Mes, **C$_{14}$**), 128.1 (**C**H, **C$_6$**, **C$_7$**), 126.0 (**C**H, **C$_8$**), 120.5, 122.2 (-**C**H=CH-, Im-**C$_9$**, **C$_{10}$**), 51.8 (**C**H$_2$, **C$_3$**, **C$_4$**), 17.3, 19.9 (CH$_3$, Mes, **C$_{12,}$ C$_{16}$**), 16.7 (CH$_3$, *m*-lutidine *equa*), 16.5 (CH$_3$,*'m*-lutidine *axial*).

7   Appendices

7.1   Appendix

This is supplementary information for chapters 2 , 3 and 4 for symmetric and asymmetric SABRE catalysts which are stated within this thesis.

7.2   NMR data collection for exchange rates calculations

7.2.1 Substrate exchange model of [Ir(H)$_2$(IXy)(py)$_3$]Cl and [Ir(H)$_2$(ITol)(py)$_3$]Cl

All data for exchange rates can be modelled on this basis. When the carbenes form SABRE active complexes with pyridine or 3,5-lutidine, there is only one site that the substrates can dissociate and associate. When obtaining the rates constants for this process, equations must be formed to explain the transfer of polarisation from the bound pyridine species and the free pyridine complexes where an exchange takes place. In this model we make the assumption that as the iridium complex forms a stable 18-electron complex, where only one substrate dissociates as a time. The polarisation exchange takes place between the equatorial substrate protons and no polarisation transfer occurs in the axial substrate as seen in Figure 86.
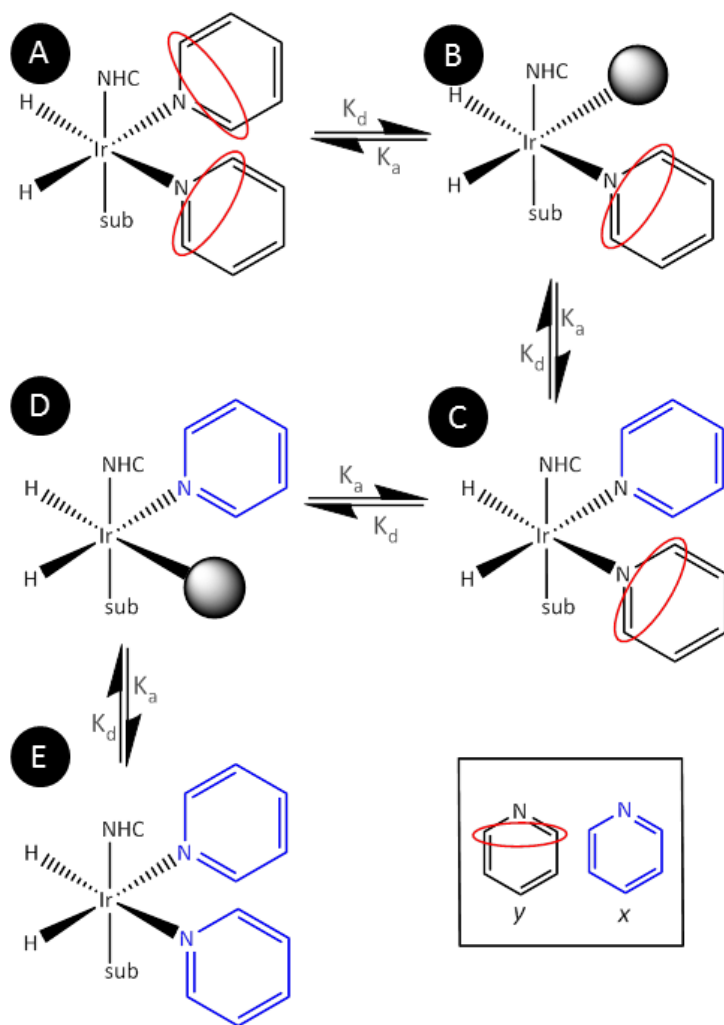
Figure 86: The pathway the kinetics will follow by exchanging polarisation from complex A to E shown in EXSY spectra for both [Ir(H)$_2$(IXy)(py)$_3$]Cl and [Ir(H)$_2$(ITol)(py)$_3$]Cl. The exchange occurs on the substrate of these catalysts so this pathway is a model for many various NHCs with the substrate as pyridine. Each species has a chloride counterion which has not been added to this figure.

As stated, in Figure 86, the pathway of the exchange polarisation model can be used for both IXy and ITol as the exchange occur within the equatorial substrate protons, this model can be explained:

o   In complex A, the polarised protons of pyridine are shown with a red circle surrounding the protons. One of the equatorial substrates can dissociate and form complex B at a rate of K_d.

o   When complex B has formed, a substrate molecule can either re-associate forming complex A at a rate of K_a, or a molecule x (non-polarised free pyridine) from complex C can associate to form complex C.

- o When complex C has formed, a molecule of *x* can either dissociate to form complex B, or a molecule of *y* (a polarised free pyridine) can associate from complex D to form complex B.

- o When complex D has formed, it can either form complex E by associating a molecule of *x* or by re-associating a molecule of *y* to form complex C.

- o When complex E has formed, it can only dissociate a molecule of *x*, as it has formed the fully unpolarised SABRE species.

The experimental data was then modelled by the formulae for each species concentration. The formulae were then used to simulate a graph on Microsoft Excel. The initial concentration of A $[A]_0$ were 5mM and the value of $[K]_0$ were measured at…

$$[A]_t = [A]_0 + K_a[B][y] - 2K_d[A]$$
$$[B]_t = [B]_0 - K_a[B][y] + 2K_d[A] + K_d[C] - K_a[B][x]$$
$$[C]_t = [C]_0 + K_a[D][y] - K_d[C] - K_d[C] + K_a[B][x]$$
$$[D]_t = [D]_0 - K_a[D][x] + K_d[E]$$
$$[E]_t = [E]_0 - K_a[D][y] - 2K_d[E] + K_d[C] + K_a[D][x]$$

Equation 3: Rate equations for the different species shown in figure 16.

7.2.2 Calculating exchange rates

A multitude of ^{1}H selective NOSEY NMR experiments were collected by exciting the bound ortho pyridine after a selectively short mixing time. The bound *ortho* pyridine integral was taken against the free pyridine in solution and changed to a percentage of each other which is then plotted in Excel and produces a graph seen in Figure 87.
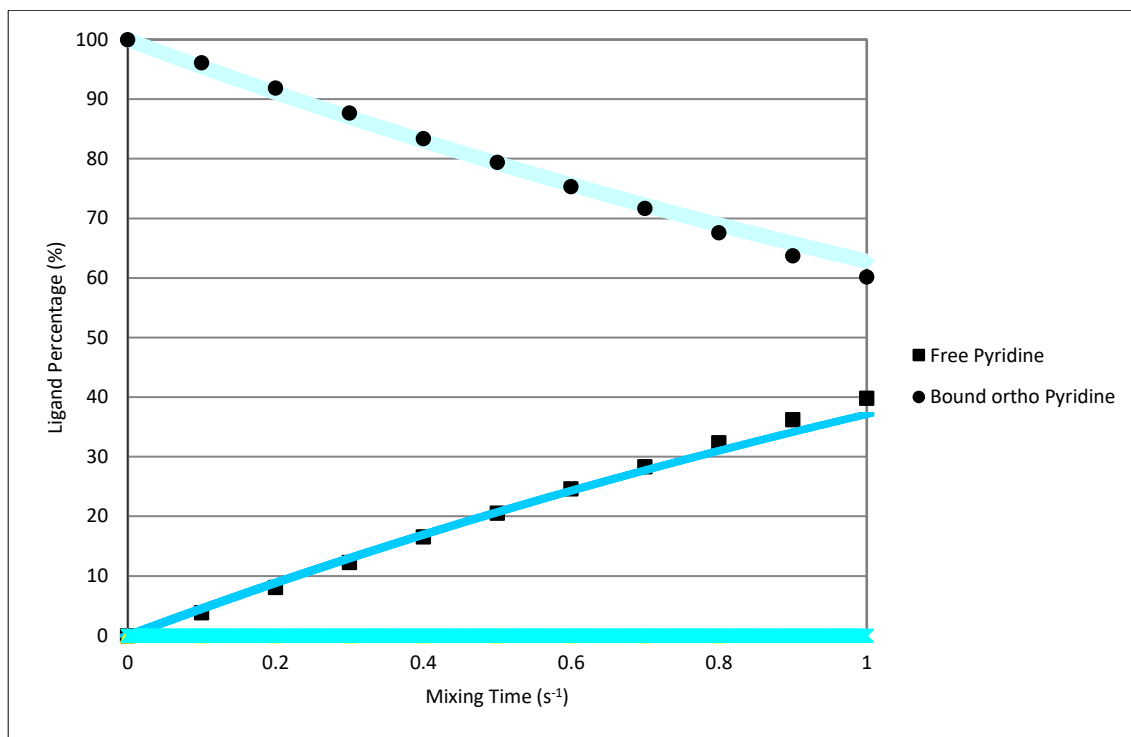
Figure 87: A graph of bound ortho pyridine and free pyridine determined from the selective NOSEY experiments. The mixing time of the free pyridine and bound pyridine are plotted against the percentage of each of these. This data was collected for complex 4, IrCl (COD)(IXy) and 5 equivalents of pyridine in CD$_3$OD, at 273 K monitored the ligand loss.

7.2.3 Calculating the thermodynamics data

The thermodynamics data was calculated using the Eyring-Polanyi method which plots $\left(\frac{1}{T}\right)$ against $\ln\frac{2k}{T}$. T is the temperature in K and k being the rate constant measured in s^{-1}. To determine the Gibbs free energy the line produced in Figure 87 is a straight line, therefore we can get the gradient and intercept from which can derive the Eyring equation using y = mx + c:

$$\ln\frac{k}{T} = \frac{-\Delta H^{\neq}}{RT} + \ln\frac{k_B}{h} + \frac{\Delta S^{\neq}}{R}$$

Equation 4: The Eyring-Polanyi Equation (Linear form)

This in turn provides us with the Eyring-Polanyi Equation:

$$k = \frac{k_B T}{h} e^{\frac{\Delta S^{\neq}}{R}} e^{\frac{-\Delta H^{\neq}}{RT}}$$

Equation 5: The Eyring-Polanyi Equation

The enthalpy and entropy can be determined from the gradient $\left(-\frac{\Delta H^{\neq}}{R}\right)$ and the intercept $\left(\ln\left(\frac{k_B}{h}\right) + \frac{\Delta S^{\neq}}{R}\right)$. Once the dissociation rate constant is determined over multiple temperatures, this provides a route to determine the Gibbs free energy:

$$\Delta G^{\neq} = \Delta H^{\neq} - T\Delta S^{\neq}$$

Equation 6: Gibbs free energy

7.2.4 Rate constant and thermodynamic data for ligand loss of symmetric catalysts with pyridine

The data collected in the section is for ligand loss of pyridine with the symmetric SABRE catalysts and IXy was the only SABRE catalyst monitored for its rates.

[IrCl(COD)(IXy)]	
Temperature (K)	K_d (s^{-1})
263	0.085
273	0.464
283	2.110
293	8.290
298	12.100

Table 6: The rate of dissociation constants for pyridine loss from 4 at different given temperatures

The data in Table 6 is used to produce the Eyring plot, from the Eyring-Polanyi equation in Figure 88.
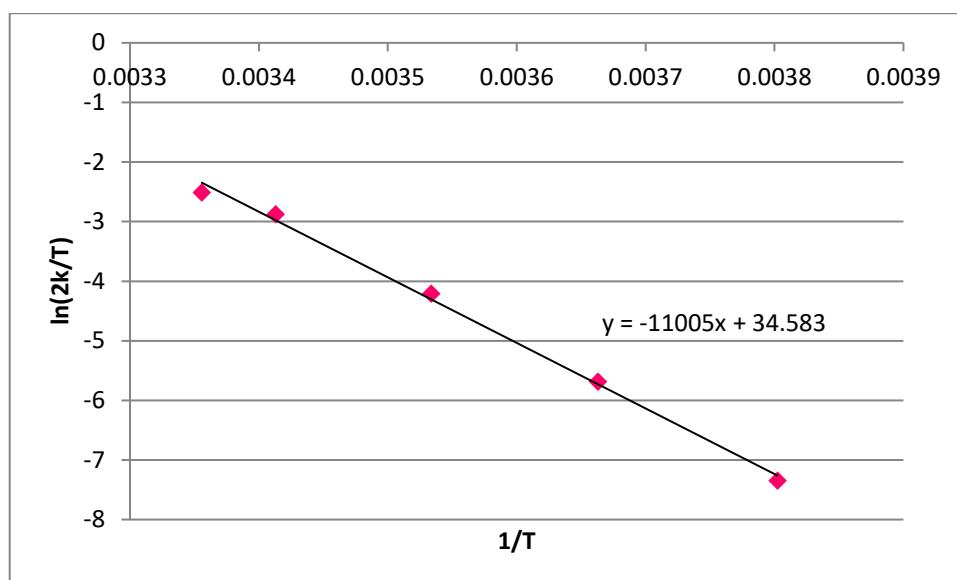
Figure 88: Eyring plots plotted for loss of pyridine from complex 4 with the gradient and intercept shown. This graph is produced from the table seen in

Once the gradient and intercept are determined, we can then use this equation to work out the thermodynamic parameters, enthalpy, entropy and the Gibbs free energy.

Ligand Loss (py)	
$\Delta G^{\neq}$ (kJ)	−138.7
$\Delta H^{\neq}$ (kJ)	91.5
$\Delta S^{\neq}$ (kJ)	0.77

Table 7: The thermodynamic parameters for the loss of pyridine with catalyst 4.

7.2.5 Rate constant and thermodynamic data for symmetric catalysts with 3,5-Lutidine

The data provided in this section is for the symmetric catalysts with 3,5 Lutidine as the substrate, IMes, being the only symmetric catalyst examined with 3,5-Lutidine.

[IrCl(COD)(IMes)]	
Temperature (K)	K_d (s^{-1})
298	2.10
303	2.60

Table 8: Rate constants for the loss of 3,5-Lutidine for IMes at different given temperature.
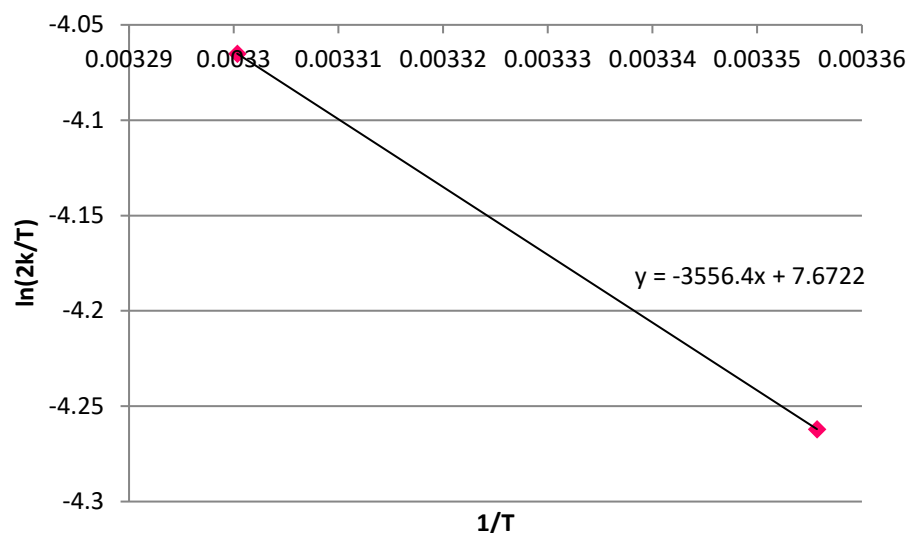
Figure 89: Eyring plot for ligand loss from IMes with 3,5-luidine as the substrate, this is then used to produce the thermodynamics data in

Table 9 displays the thermodynamic parameters calculated from the Eyring plot seen in Figure 89. It is important to identify that there are only two data points due to the rates of ligand loss being unidentifiable at lower and higher temperatures than the two stated.

Ligand Loss (3,5-Lutidine)	
$\Delta G^{\ddagger}$ (kJ)	−133.90
$\Delta H^{\ddagger}$ (kJ)	29.57
$\Delta S^{\ddagger}$ (kJ)	0.54

Table 9: Thermodynamic data presented and calculated using the gradient and intercept from

7.2.6 Rate constant and thermodynamic data for asymmetric catalysts with 3,5-Lutidine

The data collected in this section is for the asymmetric catalysts with 3,5-lutidine as the ligand of choice. The SABRE catalysts monitored for the rate reactions were: PhCarCH$_3$, MesCarCH$_3$ and MesCarHomoBenzyl.

The first catalyst examined with 3,5-Lutidine was PhCarCH$_3$.

[IrCl(COD)(PhCarCH$_3$)]	
Temperature (K)	K_d (s^{-1})
298	0.337
303	0.53

Table 10: Rate constants for the loss of 3,5-Lutidine at different temperatures with IrCl(COD)(PhCarCH$_3$) as the NHC and 3,5-Lutidine as the substrate ligand.

The data from Table 10 was used to produce the Eyring Plot seen in Figure 90.
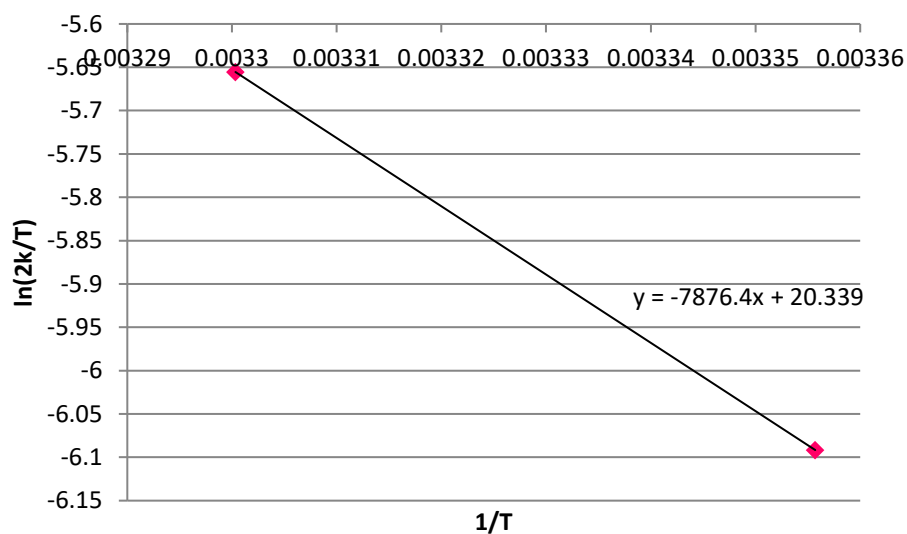
Figure 90: An Eyring plot of the loss of 3,5-Lutidine as the ligand in the presence of [IrCl(PhCarCH$_3$)] with the equation showing the gradient and intercept of the line . This graph was produced using the data in Table 10.

The equation seen in Figure 90 was then used to calculate the Gibbs free energy, the enthalpy and entropy seen in Table 11. It is important to identify that there are only two data points due to the rates of ligand loss being unidentifiable at lower and higher temperatures than the two stated.

Ligand Loss (3,5-Lutidine)	
ΔG‡ (kJ)	−129
ΔH‡ (kJ)	66.3
ΔS‡ (kJ)	0.654

Table 11: Thermodynamic data for the loss of 3,5-Lutidine with the catalysts IrCl(PhCarCH$_3$)

The same process that was used for the second catalyst examined with 3,5-Lutidine which was MesCarCH$_3$.

[IrCl(COD)(MesCarCH$_3$)]	
Temperature (K)	K$_d$ (s^{-1})
298	1.01
303	1.89

Table 12: Rate constants of the loss of 3,5-lutidine with IrCl(COD)(MesCarCH$_3$) as the NHC at various temperatures.

The data shown in Table 12 was used to produce the Eyring plot seen in Figure 91.
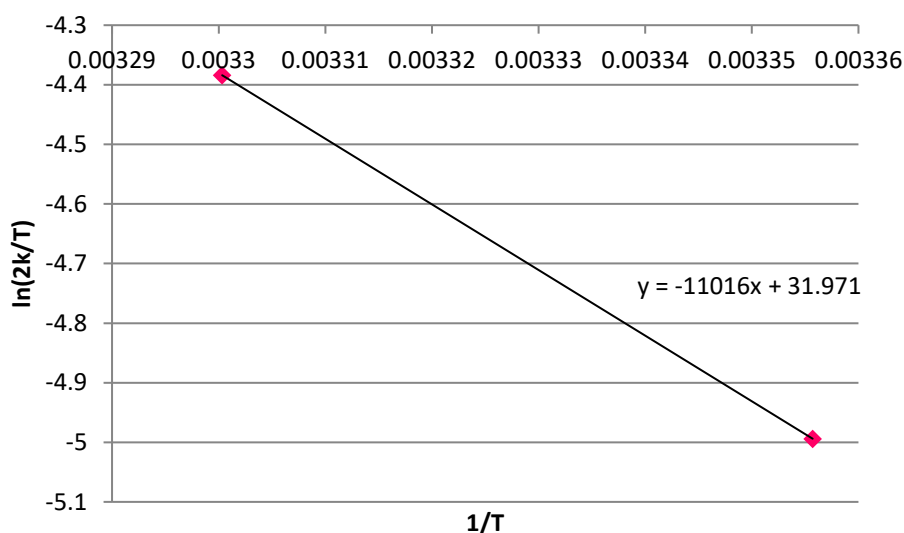
Figure 91: This Eyring plot for ligand loss of 3,5-Lutidine with IrCl(COD)(MesCarCH$_3$) was produced from the data shown in Table 11.

The graph displayed in Figure 91, was used to calculate the data shown in Table 13. It is important to identify that there are only two data points due to the rates of ligand loss being unidentifiable at lower and higher temperatures than the two stated.

Ligand Loss (3.5-Lutidine)	
ΔG‡ (kJ)	−132

ΔH‡ (kJ)	91.6
ΔS‡ (kJ)	0.751

Table 13: This table displays the thermodynamic data for the loss of 3,5-Lutidine with the catalyst

The final catalysts examined to calculate the rate constants and the thermodynamic parameters was [IrCl(COD)(MesCarHomoBenzyl)]. Table 14 displays the rate constants for loss of 3,5-lutidine with 3 at various temperatures.

[IrCl(COD)(MesCarHomoBenzyl)]	
Temperature (K)	K_d (s^{-1})
298	1.19
303	3.70
313	10.8

Table 14: Rate constants for the loss of 3,5-Lutidine with catalyst 3 at different temperatures indicated.

The data displayed in Table 15 was used to produce the Eyring plot graph seen in Figure 92.
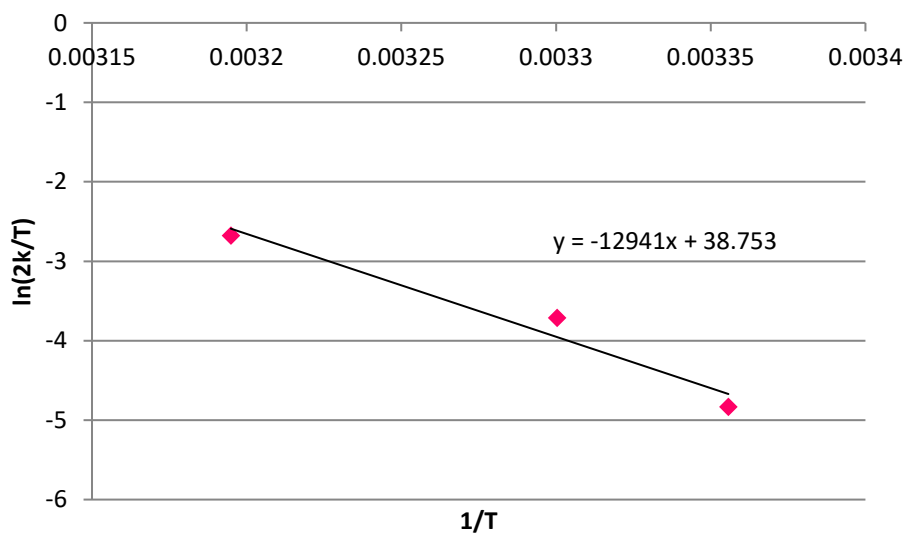
Figure 92: Eyring plot of the loss of 3,5-lutidine ligands from 3 with the equation stating the gradient and intercept. The data in Table 14 was used to plot this data.

Figure 92 displays the gradient and intercept equation needed to determine the thermodynamic data presented in Table 15.

Ligand Loss (3,5-Lutidine)	
$\Delta G^{\neq}$ (kJ)	−133
$\Delta H^{\neq}$ (kJ)	108
$\Delta S^{\neq}$ (kJ)	0.807

Table 15: Thermodynamic data of the activation for the loss of 3,5-Lutidine with catalyst 3.

8 Abbreviations

$\Delta G^{\neq}$	Gibbs free energy
$\Delta H^{\neq}$	Enthalpy of activation
$\Delta S^{\neq}$	Entropy of activation
μL	Microlitre
μM	Mircomole
1D	1-Dimensional
2D	2-dimensional
ALTADENA	Adiabatic longitudinal transfer after dissociation engenders net alignment
bar	Unit of pressure
ca.	Approximately
CD_2Cl_2	Deuterated Dichloromethane
CD_3OD	Deuterated Methanol
COD	1, 5 - *cis-cis* - Cyclooctadiene
COSY	Correlated spectroscopy
Cy	Cyclohexal
DCM	Dichloromethane
dmp	Di-methyl phenyl
DNP	Dynamic Nuclear Polarisation
E	Enhancement
eq.	Equivalent
eq.	Equivalent(s)
ESI	Electrospray Ionisation
EtOAc	Ethyl Acetate
EtOH	Ethanol
EXSY	Exchange Spectroscopy
G	Gauss
G	Gauss
h	Planck constant
ħ	reduced Planck constant
HCl	Hydrochloric Acid
IMes	1,3-bis(2,4,6-trimethylphenyl)imidazol-2-ylidene
ITol	1,3-bis(4-methylphenyl)imidazolium chloride
IXy	1,3 -bis(2,6-Dimethylbenzene)imidazol-2-ylidene
J	Joules
K	Kelvin
k	Boltzmann constant
kJ	Kilojoules
KO^{t}Bu	Potassium *tert*-butoxide
m	*meta*
MeOH	Methanol
Mes	Mesityl

MHz	Megahertz
mL	Millilitre
mM	Millimolar
mol	mole
MR	Magnetic Resonance
MRI	Magnetic Resonance Imaging
MS	Mass Spectrometry
NHC	*N*-Heterocyclic Carbene
NMR	Nuclear Magnetic Resonance
o	*ortho*
p	*para*
PASADENA	*Para*hydrogen And Synthesis Allow Dramatically Enhanced Nuclear Alignment
Ph	Phenyl
p-H$_2$	*para*hydrogen
PHIP	*para*hydrogen induced polarisation
PPh$_3$	triphenyl phosphine
ppm	parts per million
PR$_3$	phosphine ligand
PTF	polarisation transfer field
py	pyridine
R	any group
R	gas constant
rt	Room Temperature
SABRE	Signal Amplification by Reversible Exchange
SIMes	1,3-bis(2,4,6-trimethylphenyl)-4,5-dihydroimidazol-2-ylidene
sub	Substrate
T	Tesla
T	Temperature
tBu	tert-butyl
tBuBIM	1,3-Di-tert-butylimidazolium chloride
THF	Tetrahydrofuan

9   References

1. L. S. Lloyd, A. Asghar, M. J. Burns, A. Charlton, S. Coombes, M. J. Cowley, G. J. Dear, S. B. Duckett, G. R. Genov, G. G. R. Green, L. A. R. Highton, A. J. J. Hooper, M. Khan, I. G. Khazal, R. J. Lewis, R. E. Mewis, A. D. Roberts and A. J. Ruddlesden, *Catalysis Science & Technology*, 2014, **4**, 3544-3554.
2. U. Holzgrabe, *Prog. Nucl. Magn. Reson. Spectrosc.*, 2010, **57**, 229-240.
3. M. M. Britton, *Chem. Soc. Rev.*, 2010, **39**, 4036-4043.
4. F. G. Lynn and A. Paul, *Meas. Sci. Technol.*, 1996, **7**, 423.
5. R. W. Adams, J. A. Aguilar, K. D. Atkinson, M. J. Cowley, P. I. P. Elliott, S. B. Duckett, G. G. R. Green, I. G. Khazal, J. Lopez-Serrano and D. C. Williamson, *Science*, 2009, **323**, 1708-1711.
6. I. I. Rabi, S. Millman, P. Kusch and J. R. Zacharias, *Phys. Rev*, 1939, **55**, 526.
7. E. D. Becker, *Anal. Chem.*, 1993, **65**, 295A-302A.
8. K. Zangger, *Prog. Nucl. Magn. Reson. Spectrosc.*, 2015, **86–87**, 1-20.
9. A. J. J. Hooper, Ph.D., University of York, 2015.
10. T. D. Claridge, *High-resolution NMR techniques in organic chemistry*, Elsevier, 2016.
11. P. Hore, *Nuclear magnetic resonance*, Oxford University Press, USA, 2015.
12. J. A. Iggo, *NMR spectroscopy in inorganic chemistry*, Oxford University Press New York, 1999.
13. L. Frydman, *Nat Chem*, 2009, **1**, 176-178.
14. J. Keeler, *Understanding NMR spectroscopy*, John Wiley & Sons, 2011.
15. K. Hashi, S. Ohki, S. Matsumoto, G. Nishijima, A. Goto, K. Deguchi, K. Yamada, T. Noguchi, S. Sakai and M. Takahashi, *J. Magn. Reson.*, 2015, **256**, 30-33.
16. K. D. Atkinson, M. J. Cowley, P. I. P. Elliott, S. B. Duckett, G. G. R. Green, J. López-Serrano and A. C. Whitwood, *J. Am. Chem. Soc.*, 2009, **131**, 13362-13368.
17. T. R. Carver and C. P. Slichter, *Phys.Rev.*, 1953, **92**, 212-213.
18. P. Nikolaou, B. M. Goodson and E. Y. Chekmenev, *Chemistry – Chem. Eur. J*, 2015, **21**, 3156-3166.
19. *J. Chem. Soc., Dalton Transactions*, 1995, DOI: 10.1039/DT99500FX097, X097-X098.
20. C. R. Bowers and D. P. Weitekamp, *Phys. Rev. Lett.*, 1986, **57**, 2645-2648.
21. C. R. Bowers and D. P. Weitekamp, *J. Am. Chem. Soc.*, 1987, **109**, 5541-5542.
22. S. B. Duckett and N. J. Wood, *Coord. Chem. Rev.*, 2008, **252**, 2278-2291.
23. S. B. Duckett and S. A. Colebrooke, in *eMagRes*, John Wiley & Sons, Ltd, 2007.
24. M. Matsumoto and J. H. Espenson, *J. Am. Chem. Soc.*, 2005, **127**, 11447-11453.
25. L. T. Kuhn and Ü. Akbey, *Hyperpolarization methods in NMR spectroscopy*, Springer, 2013.
26. W. Lichten, *Phys. Rev*, 1962, **126**, 1020.
27. J. Kestin, *A course in thermodynamics*, CRC Press, 1979.
28. Y. Fukai, *The metal-hydrogen system: basic bulk properties*, Springer Science & Business Media, 2006.
29. S. B. Duckett and C. J. Sleigh, *Prog. Nucl. Magn. Reson. Spectrosc.*, 1999, **34**, 71-92.
30. P. L. Chapovsky and L. J. F. Hermans, *Annu. Rev. Phys. Chem.*, 1999, **50**, 315-345.
31. A. Farkas, 1935.
32. P. Emmett and R. Harkness, *J. Am. Chem. Soc.*, 1935, **57**, 1624-1631.
33. J. Natterer and J. Bargon, *Prog. Nucl. Magn. Reson. Spectrosc.*, 1997, **31**, 293-315.
34. M. Fekete, C. Gibard, G. J. Dear, G. G. R. Green, A. J. J. Hooper, A. D. Roberts, F. Cisnetti and S. B. Duckett, *Dalton Transactions*, 2015, **44**, 7870-7880.
35. M. G. Pravica and D. P. Weitekamp, *Chem. Phys. Lett.*, 1988, **145**, 255-258.
36. J. Y. C. Chen, unpublished work.
37. N. M. Zacharias, H. R. Chan, N. Sailasuta, B. D. Ross and P. Bhattacharya, *J. Am. Chem. Soc.*, 2012, **134**, 934-943.

38. R. V. Shchepin, A. M. Coffey, K. W. Waddell and E. Y. Chekmenev, *J. Phys, Chem. Lett.*, 2012, **3**, 3281-3285.
39. J. Jimenez-Barbero, J. Waterton and F. G. Vogt, *New applications of NMR in drug discovery and development*, Royal Society of Chemistry, 2013.
40. R. E. Mewis, *Magnetic Resonance in Chemistry*, 2015, **53**, 789-800.
41. R. W. Adams, S. B. Duckett, R. A. Green, D. C. Williamson and G. G. R. Green, *J. Phys. Chem.*, 2009, **131**.
42. L. D. Vázquez-Serrano, B. T. Owens and J. M. Buriak, *Chem. Commun. (Cambridge, U. K.)*, 2002, 2518-2519.
43. M. J. Cowley, R. W. Adams, K. D. Atkinson, M. C. R. Cockett, S. B. Duckett, G. G. R. Green, J. A. B. Lohman, R. Kerssebaum, D. Kilgour and R. E. Mewis, *J. Am. Chem. Soc.*, 2011, **133**, 6134-6137.
44. D. Blazina, S. B. Duckett, T. K. Halstead, C. M. Kozak, R. J. K. Taylor, M. S. Anwar, J. A. Jones and H. A. Carteret, *Magn. Reson. Chem.*, 2005, **43**, 200-208.
45. Q. Gong, A. Gordji-Nejad, B. Blümich and S. Appelt, *Anal. Chem.*, 2010, **82**, 7078-7082.
46. K. M. Appleby, R. E. Mewis, A. M. Olaru, G. G. R. Green, I. J. S. Fairlamb and S. B. Duckett, *Chemical Science*, 2015, **6**, 3981-3993.
47. A. J. Ruddlesden, R. E. Mewis, G. G. R. Green, A. C. Whitwood and S. B. Duckett, *Organometallics*, 2015, **34**, 2997-3006.
48. B. J. A. van Weerdenburg, S. Gloggler, N. Eshuis, A. H. J. Engwerda, J. M. M. Smits, R. de Gelder, S. Appelt, S. S. Wymenga, M. Tessari, M. C. Feiters, B. Blumich and F. Rutjes, *Chem. Commun.*, 2013, **49**, 7388-7390.
49. M. Fekete, C. Gibard, G. Dear, G. Green, A. Hooper, A. Roberts, F. Cisnetti and S. Duckett, *Dalton Trans.*, 2015, **44**, 7870-7880.
50. D. Bourissou, O. Guerret, F. P. Gabbaï and G. Bertrand, *Chem. Rev. (Washington, DC, U. S.)*, 2000, **100**, 39-92.
51. H. Jacobsen, A. Correa, A. Poater, C. Costabile and L. Cavallo, *Coord. Chem. Rev.*, 2009, **253**, 687-703.
52. E. O. Fischer and A. Maasböl, *Angewandte Chemie International Edition in English*, 1964, **3**, 580-581.
53. D. S. Marynick and C. M. Kirkpatrick, *J. Am. Chem. Soc.*, 1985, **107**, 1993-1994.
54. R. A. Van Santen and M. Neurock, *Molecular heterogeneous catalysis: a conceptual and computational approach*, John Wiley & Sons, 2009.
55. C. D. Montgomery, *J. Chem. Educ.*, 2015, **92**, 1653-1660.
56. R. R. Schrock, *J. Am. Chem. Soc.*, 1975, **97**, 6577-6578.
57. M. N. Hopkinson, C. Richter, M. Schedler and F. Glorius, *Nature*, 2014, **510**, 485-496.
58. J. B. P. Dumas, E, *Ann. Chim. Phys*, 1835, **58**, 5–74.
59. A. J. Arduengo, R. L. Harlow and M. Kline, *J. Am. Chem. Soc.*, 1991, **113**, 361-363.
60. A. Igau, H. Grutzmacher, A. Baceiredo and G. Bertrand, *J. Am. Chem. Soc.*, 1988, **110**, 6463-6466.
61. A. Albright, D. Eddings, R. Black, C. J. Welch, N. N. Gerasimchuk and R. E. Gawley, *J. Org. Chem.,* 2011, **76**, 7341-7351.
62. V. Lavallo, Y. Canac, C. Präsang, B. Donnadieu and G. Bertrand, *Angew. Chem. Int. Ed.*, 2005, **44**, 5705-5709.
63. K. O. W.A. Herrmann, D. von Preysing, E. Herdtweck, J., *Organomet. Chem.*, 2003, 235.
64. L. Benhamou, E. Chardon, G. Lavigne, S. Bellemin-Laponnaz and V. César, *Chem. Rev.*, 2011, **111**, 2705-2733.
65. S. Díez-González, N. Marion and S. P. Nolan, *Chem. Rev.*, 2009, **109**, 3612-3676.
66. J. Mathew and C. H. Suresh, *Organometallics*, 2011, **30**, 3106-3112.
67. G. D. Frey, V. Lavallo, B. Donnadieu, W. W. Schoeller and G. Bertrand, *Science*, 2007, **316**, 439-441.
68. K. K. Irikura, W. A. Goddard and J. L. Beauchamp, *J. Am. Chem. Soc.*, 1992, **114**, 48-51.
69. B. Gilbert, D. Griller and A. Nazran, *J. Org. Chem.*, 1985, **50**, 4738-4742.

70. K. D. Atkinson, M. J. Cowley, S. B. Duckett, P. I. P. Elliott, G. G. R. Green, J. López-Serrano, I. G. Khazal and A. C. Whitwood, *Inorg. Chem.*, 2009, **48**, 663-670.

71. A. J. Ruddlesden and S. B. Duckett, *Chem. Commun. (Cambridge, U. K.)*, 2016, **52**, 8467-8470.

72. H. Zeng, J. Xu, J. Gillen, M. T. McMahon, D. Artemov, J. M. Tyburn, J. A. Lohman, R. E. Mewis, K. D. Atkinson, G. G. Green, S. B. Duckett and P. C. van Zijl, *J Magn Reson*, 2013, **237**, 73-78.

73. Y. Canac and C. Lepetit, *Inorg. Chem.*, 2016, **56**, 667-675.

74. A. J. Arduengo Iii, R. Krafczyk, R. Schmutzler, H. A. Craig, J. R. Goerlich, W. J. Marshall and M. Unverzagt, *Tetrahedron*, 1999, **55**, 14523-14534.

75. A. A. Altaf, A. Shahzad, Z. Gul, N. Rasool, A. Badshah, B. Lal and E. Khan, *J. Drug Des. Med. Chem*, 2015, **1**, 1-11.

76. J. J. Li, D. S. Johnson, D. R. Sliskovic and B. D. Roth, in *Contemporary Drug Synthesis*, John Wiley & Sons, Inc., 2004, DOI: 10.1002/0471686743.ch3, pp. 21-27.

77. S. Wieland and R. Van Eldik, *Organometallics*, 1991, **10**, 3110-3114.

78. D. C. Harris, *J. Chem. Educ*, 1998, **75**, 119.

79. A. J. Vetter, R. D. Rieth, W. W. Brennessel and W. D. Jones, *J. Am. Chem. Soc.*, 2009, **131**, 10742-10752.

80. S. Gulcemal, A. G. Gokce and B. Cetinkaya, *Dalton Transactions*, 2013, **42**, 7305-7311.

81. R. E. Mewis, R. A. Green, M. C. R. Cockett, M. J. Cowley, S. B. Duckett, G. G. R. Green, R. O. John, P. J. Rayner and D. C. Williamson, *J. Phys. Chem.*, 2015, **119**, 1416-1424.

82. P. J. Rayner, M. J. Burns, A. M. Olaru, P. Norcott, M. Fekete, G. G. R. Green, L. A. R. Highton, R. E. Mewis and S. B. Duckett, *Proc. Natl. Acad. Sci. U.S.A.*, 2017, **114**, E3188-E3194.

83. R. E. Mewis, K. D. Atkinson, M. J. Cowley, S. B. Duckett, G. G. R. Green, R. A. Green, L. A. R. Highton, D. Kilgour, L. S. Lloyd, J. A. B. Lohman and D. C. Williamson, *Magnetic Resonance in Chemistry*, 2014, **52**, 358-369.

84. H. Zeng, J. Xu, J. Gillen, M. T. McMahon, D. Artemov, J.-M. Tyburn, J. A. B. Lohman, R. E. Mewis, K. D. Atkinson, G. G. R. Green, S. B. Duckett and P. C. M. van Zijl, *J. Magn. Reson.*, 2013, **237**, 73-78.

85. M. L. Truong, F. Shi, P. He, B. Yuan, K. N. Plunkett, A. M. Coffey, R. V. Shchepin, D. A. Barskiy, K. V. Kovtunov, I. V. Koptyug, K. W. Waddell, B. M. Goodson and E. Y. Chekmenev, *J. Phys. Chem., B*, 2014, **118**, 13882-13889.

86. J. F. P. Colell, M. Emondts, A. W. J. Logan, K. Shen, J. Bae, R. V. Shchepin, G. X. Ortiz, P. Spannring, Q. Wang, S. J. Malcolmson, E. Y. Chekmenev, M. C. Feiters, F. P. J. T. Rutjes, B. Bluemich, T. Theis and W. S. Warren, *J. Am. Chem. Soc.*, 2017.

87. M. E. Halse, *TrAC Trends in Analytical Chemistry*, 2016, **83**, 76-83.

88. O. Torres, M. Martín and E. Sola, *Organometallics*, 2009, **28**, 863-870.